Scuola Internazionale Superiore di Studi Avanzati - Trieste

Astrophysics Sector

New *PARSEC* evolutionary tracks of massive stars at low metallicity: testing canonical stellar evolution in nearby star forming dwarf galaxies.

Thesis submitted for the degree of Doctor Philosophiae in Astrophysics

CANDIDATE

Jing Tang

SUPERVISOR

Prof. Alessandro Bressan

October 2015

SISSA - Via Bonomea 265 - 34136 TRIESTE - ITALY

Abstract

In this thesis I present new models of massive stars for low metallicity computed with the new code *PARSEC*: *P*adova T*R*ieste *S*tellar *E*volution *C*ode.

An updated version of this code, known as *PARSEC* V1.1, has already been released but, in the published version, the range of initial masses does not go beyond $12M_{\odot}$. Recently, the *PARSEC* library of stellar evolutionary tracks has been extended with the inclusion of new models of massive stars, from $14M_{\odot}$to $350M_{\odot}$. The input physics is the same used in the *PARSEC* V1.1 version, but for the mass-loss rate which is included by considering the most recent updates in literature.

In this thesis I perform a thorough comparison of the new models of massive stars with existing observational data. This is a critical and necessary step because the stellar evolution theory still contains some parameters that need to be tuned to well observed stellar samples.

For this reason I focus on the low metallicity environment, Z=0.001, Z=0.004 and Z=0.0005, for which the metal poor dwarf irregular star forming galaxies, Sextans A, WLM, NGC 6822 and SagDIG, provide simple but powerful workbenches: the color-magnitude diagrams (CMDs) of their young stellar populations.

From the simulations of these CMDs I draw the following conclusions:

While the new models reproduce fairly well the observed CMDs of Sextans A, WLM and NGC 6822, a detailed analysis of the stellar color distributions indicates that the predicted blue loop is not hot enough in models that assume the canonical extent of overshooting from the convective regions.

In the framework of a mild extended mixing during central hydrogen burning, the only way to reconcile the discrepancy is to enhance the overshooting at the base of the convective envelope (EO) during the first dredge-UP. Reproducing the features of the observed CMDs with standard values of envelope overshooting would require a metallicity significantly lower than the values measured in these galaxies.

I find that the mixing scales required to reproduce the observed loops are large, EO=$2H_{\rm P}$ or EO=$4H_{\rm P}$. These values are definitely larger than those derived from, e.g., the observed location of the RGB bump in low mass stars. This effect, if confirmed, would imply a strong dependence of the mixing scale below the formal Schwarzschild border, on the stellar mass or luminosity. Other quantities, such as the star formation rate and the initial mass function, are only slightly sensitive to this effect.

This result is further validated in the comparison with the observed CMD of SagDIG at lower metallicity, where I find an overshooting scale EO=$2H_{\rm P}$ to best reproduce the observed loops. I also discuss the dependence of the blue loop extension on the adopted instability criterion and find that, contrary

to what stated in literature, the Schwarzschild criterion, instead of the Ledoux criterion, favours the development of blue loops. Other factors that could affect the CMD comparisons such as differential internal extinction or the presence of binary systems are found to have negligible effects on the results.

I thus confirm that, in presence of core overshooting during the H-burning phase, a large envelope overshooting is needed to reproduce the main features of the central He-burning phase of intermediate- and high-mass stars.

Publications

- **Tang, J.**; Yu, W.-F.; Yan, Z.,
  RXTE/ASM and Swift/BAT Observations of Spectral Transitions in Bright X-ray Binaries in 2005-2010,
  2011, RAA, 434, 11
- **Tang, J.**; Bressan, A.; Rosenfield, P.; Slemer, A; Marigo, P.; Girardi, L.; Bianchi, L.,
  New PARSEC evolutionary tracks of massive stars at low metallicity: testing canonical stellar evolution in nearby star-forming dwarf galaxies,
  2014, MNRAS, 445, 4287
- Bressan, A.; Girardi, L.; Marigo, P.; Rosenfield, P.; **Tang, J.**,
  Uncertainties in stellar evolution models: convective overshoot,
  2015, Astrophysics and Space Science Proceedings, 39, 25
- **Tang, J.**; Bressan, A; Slemer, A; Marigo, P; Girardi, L; Bianchi, L; Rosenfield, P; Momany, Y.,
  Envelope Overshooting in Low Metallicity Intermediate and Massive Stars: a test with the Sagittarius Dwarf Irregular Galaxy,
  2015, MNRAS, in press

Acknowledgments

First of all, I would like to acknowledge SISSA to give me the chance to study in such a lovely place. I am grateful to my supervisor Alessandro Bressan, who really spends a lot of time and energy leading me to research, and my collaborators Luciana Bianchi, Leo Girardi, and Yazan Al Momany who help clear my doubts in the work, and also my first-year tutor Francesca Perrotta, who gives me useful advice in my study when I am fresh. I am indebted to the student secretaries, Riccardo Iancer and Federica Tuniz, for helping me live more conveniently. In addition, I thank Zhenyi Cai, Yang Chen, and Xiaoting Fu for helping me solve many technical problems, and also Claudia Antolini, Eolo Di Casola, Gianluca Castignani for their encouragement when I feel frustrated. Special thanks to all my friends, with whom I have a happy life in Trieste. Last but not least, I am missing my family in China and thank for their understanding and support.

Contents

Chapter 1

Introduction

Massive stars ($M \geq 8M_{\odot}$) play an important role in modern astrophysics. They provide most of UV radiation in the universe, ionizing the interstellar medium (ISM). They are the progenitors of blue supergiants (BSGs), red supergiants (RSGs), luminous blue variables (LBVs) and Wolf-Rayet stars. Moreover they are thought to be the likely sources of long soft gamma-ray bursts (GRBs). After explosion as type II (single star) or Ib, c (in a binary system) supernovae (SNe), their cores collapse to become neutron stars (NS) or black holes (BH). Besides they are one of the main sites for nucleosynthesis. New elements, especially those heavier than C and O, are created during both the nuclear reactions and explosive burnings. These yields are thrown out via stellar winds and explosion, chemically enriching the surroundings.

Massive stars are extremely rare. In the Milky Way, there is only one $20M_{\odot}$ star in roughly 10^5 solar-type stars and one $100M_{\odot}$ star over 10^6 solar-type stars. Nevertheless, they are very luminous and contribute significantly to the integrated luminosity of galaxies.

The PADOVA database is one of the most widely used sources of stellar evolutionary tracks and isochrones. It has been continuously updated during the last decades (Girardi et al. 2002; Marigo et al. 2008; Bertelli et al. 2009), except for the models of the most massive stars ($M > 20M_{\odot}$) that have remained untouched for two decades, after Bertelli et al. (1994). In the most recent major revision, all the basic input physics was revisited and updated, and additions were introduced, such as the pre-main-sequence phase and very low mass stellar models ($0.35M_{\odot} \geq M \geq 0.1M_{\odot}$). The *PARSEC* *P*adova T*R*ieste *S*tellar *E*volution *C*ode is described in detail in Bressan et al. (2012, 2013) and Chen et al. (2014), but the *PARSEC* revision is not complete without including models of the most massive stars. With the aim of completing the library of stellar evolutionary tracks and isochrones computed with *PARSEC*, we present the calculations of new evolutionary tracks of massive stars, from $14M_{\odot}$ to $350M_{\odot}$[1].

In this thesis, we are devoted to the evolution of massive stars using *PARSEC* at low metallicity. We present the new evolutionary tracks, and perform preliminary comparisons with observed color-magnitude diagrams (CMDs). These tests are fundamental to validate the new models.

Understanding the evolution of massive stars at low metallicity is particularly relevant, as these stars

[1] The new updated and homogeneous sets of evolutionary tracks, from very low (M=0.1$M_{\odot}$) to very massive (M=350$M_{\odot}$) stars, are available at http://stev.oapd.inaf.it

drive the chemical and dynamical evolution of the surrounding medium, and are a key ingredient in modelling galaxy evolution at early times (Groh et al. 2013; Woosley & Heger 2012). An advantage of studying massive stars at low metallicity is also that, in the very local Universe, star formation is sparkling in gas-rich galaxies which are also metal poor. In the last decades, the high spatial resolution of the space-borne HST, and the collecting power of 8m telescopes from the ground have provided accurate photometry of individual stars in these galaxies, and metallicity estimates of young stars and gas from spectroscopy. Such data enable comparison of observed CMDs with model simulations at known metallicity, an important test of how the canonical theory of the evolution of massive and intermediate-mass stars performs at low metallicity.

The internal evolution of massive stars is affected by two complex physical phenomena for which there is still a significant lack of knowledge. The first is the mass-loss rate, which becomes important in the domain of very massive stars (VMS; initial mass $M \gtrsim 30 M_{\odot}$depending on metallicity). The second is the internal mixing, usually from either differential rotation or convective overshooting. Both effects play an important role in stellar evolution because they may significantly modify the structure of the stars in an irreversible way and so their further evolution. The observational quantities that are most sensitive to internal mixing are the predicted surface abundance ratios of CNO elements (Martins & Palacios 2013; Bouret et al. 2013). In massive stars the surface abundances can be affected by mixing during the hydrogen burning phases and by the eventual subsequent first dredge-up. However, the comparison of model predictions with observed surface abundances still shows significant discrepancies (Maeder et al. 2014). Another interesting effect of mixing in this mass interval is the location in the CMD and duration of the "blue loops", where the stars spend a fraction of their central helium burning lifetime. The morphology and star population of the Blue and Red Helium Burning Sequences (BHeBS and RHeBS) may depend on several other parameters, such as the $^{12}\mathrm{C}(\alpha,\gamma)^{16}\mathrm{O}$ reaction rate (Iben 1966; Bertelli et al. 1985; Brunish & Becker 1990), and the $^{14}\mathrm{N}(\mathrm{p},\gamma)^{15}\mathrm{O}$ reaction rate (Xu & Li 2004; Weiss et al. 2005; Halabi et al. 2012), but the most important parameters are the efficiency of mixing in the convective core (Bertelli et al. 1985) and below the convective envelope (Alongi et al. 1991; Godart et al. 2013), which are described as core overshooting and envelope overshooting.

The presence of blue loops during central He-burning phase was first thoroughly investigated by Lauterborn et al. (1971) who introduced the core potential $\Phi = M_C/R_C$ with M_C and R_C being the mass and radius of the core to explain the occurrence. On the other hand, many studies show that the proximity of the H-burning shell to the H-He discontinuity marked by the depth of first dredge up triggers the blue loop (Lauterborn et al. 1971; Robertson 1972; Stothers & Chin 1991). Thus any factor that moves the discontinuity deeper into the star causes a more extended loop, such as increasing envelope opacities (Robertson 1972) and enhancing envelope overshooting (Stothers & Chin 1991; Tang et al. 2014). Further Walmswell et al. (2015) demonstrated that this phenomenon is essentially due to the removal of excess helium above the burning shell which results from the retreat of the convective core during central H burning. They considered three factors: the opacity, the fuel supply and the mean molecular weight. They found the increase in the mean molecular weight near the burning shell caused by the presence of excess helium favours considerable red-ward motion in the HR diagram. The lowered

opacity near the burning shell also compels the star to move rightwards but the effect is small, while the reduced fuel supply favours leftward motion. It is worth noting that changes to the opacity and mean molecular weight over the whole envelope have the opposite effect. They believed if the removal of excess helium happens faster than the core evolution, the blue loop is triggered.

Additionally, Chiosi & Summa (1970) found that the adoption of the Ledoux criterion instead of the Schwarzschild one for the determination of the *overshooting* region favours the development of blue loops, at least in the domain of massive stars . Though disfavored by the analisys of Kato (1966), the Ledoux criterion has recently received some observational support (Georgy et al. 2014), and its consequences are worth being explored in a systematic way.

Outline of the Thesis

While the analysis of surface abundances provides a detailed view of individual stars, the analysis of the stellar distribution across a CMD provides a complementary view of the duration of evolutionary phases over a broad range of masses. The latter requires complete, well studied and populous stellar samples.

In this thesis we use published photometry of four star-forming dwarf galaxies in the Local Group, Sextans A, WLM, NGC 6822 and SagDIG, that have hundreds of thousands resolved individual stars, complete down to intermediate-mass stars, to build the observed CMDs for comparison with our new models. In Chapter 2 we introduce the stellar structure equations and present the new stellar evolutionary tracks of intermediate- and high-mass stars calculated with *PARSEC*. Apart from the inclusion of mass loss, which had not been considered in stars less massive than M=12$M_{\odot}$, the other parameters are the standard ones in the published tracks (Bressan et al. 2012). However, having in mind the comparison with observed CMDs, we present here also models with enhanced envelope overshooting, which is known to favour more extended blue loops during central He burning. On the other hand, we discuss the blue loop and its dependence on different instability criteria. Contrary to Chiosi & Summa (1970), we find the adoption of the Schwarzschild criterion instead of the Ledoux one favours the development of blue loops when taking into account significant core overshooting. In Chapter 3 we describe the codes that we use to construct the synthetic color-magnitude diagram. The models with different envelope overshooting are compared with observations of three dwarf galaxies at low metallicities, Sextan A, WLM and NGC 6822 in Chapter 4, and with observations of SagDIG at very low metallicity in Chapter 5. The main conclusions are drawn in Chapter 6.

Chapter 2

Massive star evolution

Stellar evolution theory deals with variation of the physical and chemical properties of stars with time. In particular, as the interiors of stars cannot be observed directly, the fundamental tool to explore their internal conditions is to compare the theoretical predictions of the models of a given mass with observational quantities, usually luminosity and effective temperature.

2.1 The stellar structure

The standard stellar model is based on the following assumptions:

- Stars are spherically symmetric systems made of matter and radiation, and hence all parameters describing the star depend only on one independent variable that can be the radius r or the mass contained within that radius m_r.
- The interior of stars is assumed in local thermodynamical equilibrium (LTE). In such conditions, the radiation field can be well described by the Planck function which is only related to the temperature. At the same time the particles are well described by the usual equations: their velocity, excitation and ionization states obey the Maxwell distribution, the Boltzmann distribution and the Saha equation, respectively.
- At a generic time, stars are in hydrostatic equilibrium. The evolution is thus a sequence of hydrostatic equilibrium states, even if the star may contract or expand.
- In most numerical codes, other effects such as rotation and magnetic fields are considered negligible.

2.1.1 Equations of the stellar structure

This model contains four differential equations, describing the physical and chemical quantities of stars, i.e., radius r, pressure P, luminosity L, temperature T for a given chemical element abundances μ, as a function of m_r at a given time t, and their evolution with t. Here, the local mass value m_r replaces the

radius r as the independent variable, since the radius varies during the stellar evolution, and the local value of r is not always associated to the same mass layer.

- Continuity of mass

  Defining m_r the mass enclosed within a sphere of radius r from the centre, $m_r = \int_0^r 4\pi r^{'2}\rho dr^{'}$, where ρ is the matter density at a generic point r, we have

$$\frac{dr}{dm_r} = \frac{1}{4\pi r^2 \rho}, \tag{2.1}$$

- Hydrostatic equilibrium

  Hydrostatic equilibrium means that a generic volume element is at rest or keeps constant velocity to move. In stars, this occurs when the inward gravity is balanced by the outward pressure force.

$$\frac{dP}{dm_r} = -\frac{Gm_r}{4\pi r^4}, \tag{2.2}$$

- Conservation of energy

  In stars, there are three mechanisms related to the energy generation. ϵ denotes the energy generated per unit time and per unit mass, $\epsilon = \epsilon_n + \epsilon_g + \epsilon_\nu$. ϵ_n is the energy produced by nuclear reactions. ϵ_g is the energy resulting from the thermodynamical transformations, e.g., the change of the internal energy, the contraction and expansion of the star, and it is usually named the gravitational energy. ϵ_ν is the energy loss associated to the neutrino. Defining L_r the luminosity at distance r, equal to the energy generated within the sphere of radius r, i.e. $L_r = \int_0^r 4\pi r^{'2}\rho\epsilon dr^{'}$, we have

$$\frac{dL_r}{dm_r} = \epsilon, \tag{2.3}$$

- Energy transport

  The energy is produced and transported through the star to be released from the surface. There are three forms of energy transport in stars, radiation by photons, conduction by electrons, and convection involving organized large-scale motions of the matter. It is worth noting that electron transport is very inefficient compared to radiation, unless electrons are strongly degenerate in which case conduction becomes very efficient.

$$\frac{dT}{dm_r} = -\frac{Gm_r}{4\pi r^4}\frac{T}{P}\nabla, \qquad \nabla = \begin{cases} \nabla_{rad}, & \text{radiative region } (\nabla_{rad} < \nabla_{ad}) \\ \nabla_{con}, & \text{convective region } (\nabla_{rad} > \nabla_{ad}) \end{cases} \tag{2.4}$$

  where $\nabla \equiv \frac{dln(T)}{dln(P)} = \frac{P}{T}\frac{dT}{dP}$ is the generic temperature logarithmic gradient with respect to pressure, corresponding to the dominant energy transport mechanism.

If radiative transport is dominant, we have

$$\nabla_{rad} = \frac{3}{16\pi acG}\frac{\kappa L_r P}{m_r T^4}, \tag{2.5}$$

where κ is the total opacity of the stellar matter and a is the black-body constant related to the Stefan-Boltzmann constant $\sigma = 5.67051 \times 10^{-5} ergcm^{-2}s^{-1}K^{-4}$ by the relationship $a = 4\sigma/c$.

Instead, if convective energy transport is the dominant mechanism, we have

$$\nabla_{con} = \begin{cases} \nabla_{ad}, & \text{deep stellar interiors} \\ \nabla_{ad} + \frac{1}{W^2}(W^2 + \frac{19}{27}WU - \frac{E}{3})^2 - U^2, & \text{outer layers close to the surface} \end{cases} \tag{2.6}$$

with

$$W \equiv (\frac{1}{2}A + \sqrt{D})^{1/3}, \tag{2.7}$$

$$\frac{A}{2} \equiv [\frac{4}{9}(\nabla_{rad} - \nabla_{ad}) + (\frac{19^3}{27^3} - \frac{1}{9})U^2]U, \tag{2.8}$$

$$D \equiv (\frac{A}{2})^2 + (\frac{E}{3})^3, \tag{2.9}$$

$$\frac{E}{3} \equiv \frac{368}{729}U^2, \tag{2.10}$$

$$U \equiv \frac{12\sigma T^3}{c_p \rho^2 l \kappa}(\frac{8H_P}{gl^2\delta})^{1/2}, \tag{2.11}$$

$$H_P = \frac{k_B T}{g\mu m_H \beta}, \tag{2.12}$$

$$g = \frac{Gm_r}{r^2}, \tag{2.13}$$

$$\delta = -(\frac{\partial ln\rho}{\partial lnT})_P, \tag{2.14}$$

where l is the mean free path and c_p is the heat at constant pressure. $k_B = 1.38 \times 10^{-23} J/K$ is Boltzmann constant. $\beta \equiv P_{gas}/P$, where $P = P_{gas} + P_{rad}$. $\nabla_{ad} = \frac{\delta P}{c_p T \rho}$ is the adiabatic gradient and it is typically equal to 0.4 (0.25 when $\beta \sim 0$), while in the partially ionized regions close to the surface, it can drop below 0.1.

Notice that the above four equations of stellar structure contain the constitutive equations:

- a) the equation of state $P = P(\rho, T, \mu)$
- b) the opacity of stellar matter $\kappa = \kappa(\rho, T, \mu)$
- c) nuclear reaction rates $\epsilon_n = \epsilon_n(\rho, T, \mu)$
- d) electron-neutrino loss rates $\epsilon_\nu = \epsilon_\nu(\rho, T, \mu)$
- e) other thermodynamic functions that enter ϵ_g, ∇_{ad}, and other quantities used in the determination of the convective temperature gradient.

To obtain the equilibrium solution we need four boundary conditions. Two boundary conditions are trivial, r(m_r=0)=0, L_r(m_r=0)=0. The other two boundary conditions are much less trivial and are

obtained from the detailed models of stellar atmospheres. They are expressed as T=$T_{photosphere}$ and P=$P_{photosphere}$ with the photosphere set at m_r=M_{tot} where the photons can freely escape from the star. This condition is expressed in terms of the optical depth of the photosphere (τ) which is usually set at $\tau \sim 2/3$. The full system of equations is then solved numerically with the so called Henyey method.

Once the equilibrium structure at a given time is known, the evolution is computed by changing the chemical element abundances caused by nuclear burning and eventual mixing, and recomputing a new equilibrium structure at the new time step.

The variation of the abundances of chemical elements owing to the nuclear reaction is given by

$$\frac{dY_i}{dt} = -\rho N_A \sum_j \frac{a_i}{1+\delta_{ij}} Y_i Y_j < \sigma\nu >_{ij} + \rho N_A \sum_{k,l} \frac{b_i}{1+\delta_{kl}} Y_k Y_l < \sigma\nu >_{kl}, \tag{2.15}$$

with

$$Y_i = \frac{X_i}{A_i}, \tag{2.16}$$

and

$$\delta_{ij} = \begin{cases} 0, & i \neq j \\ 1, & i = j \end{cases}, \quad \delta_{kl} = \begin{cases} 0, & k \neq l \\ 1, & k = l \end{cases} \tag{2.17}$$

where X_i and A_i are the mass fraction (normalized to unity) and atomic weight of a generic element i, respectively, and thus Y_i represents the number fraction. ρ is the density. $N_A = 6.02217 \times 10^{23} mol^{-1}$ is avogadro constant, defined as the number of the particles per mole. a_i indicates the number of element i destroyed in the reaction: $i + j \rightarrow z$, while b_i indicates the number of element i generated in the reaction: $k + l \rightarrow i$. $< \sigma\nu >_{ij}$ is the cross section for the reaction between i and j.

In radiative region, there is no matter exchange between neighboring mass layers and hence the variation of the chemical abundances is caused by nuclear reactions.

In convective region containing nuclear reactions, all elements are dispersed homogeneously and the chemical composition is uniform. Assuming the convective region extends outward from mass layer m_1 to mass layer m_2, the time evolution of element abundances in this region can be described as

$$\frac{dY_i}{dt} = \frac{\int_{m_1}^{m_2} \frac{dY_i^{'}}{dt} dm}{\int_{m_1}^{m_2} dm}, \tag{2.18}$$

where $\frac{dY_i^{'}}{dt}$ represents the variation of chemical composition caused by nuclear reactions and can be calculated by equation (2.15).

Generally, the timescale of convection is much shorter than that of nuclear reactions, hence the new nuclei created from the nuclear burning will be instantaneously redistributed all over the convective region and the chemical composition always keeps uniform in this region.

2.1.2 Convective instability

The main energy transport mechanisms in stellar interior are due to photon diffusion (radiative transport) or macroscopic motions (convective transport). Energy transport by microscopic motions, thermal conduction, is negligible, but for the most dense regions when electron degeneracy dominates the equation of state. Because of the difference between the radiative and convective temperature gradients and because of the mixing induced by convective motions, it is important to determine whether a particular region is stable against convection, or not.

Consider a bubble of gas, with pressure P_e, temperature T_e, density ρ_e and molecular weight μ_e, in equilibrium with the surrounding radiative medium, characterized by P_{rad}, T_{rad}, ρ_{rad} and μ_{rad}. The equation of state is that of the perfect gas,

$$P = \frac{k_B}{\mu m_H \beta}\rho T, \tag{2.19}$$

where $k_B = 1.38 \times 10^{-23} J/K$ is Boltzmann constant and $\beta \equiv P_{gas}/P$, where $P = P_{gas} + P_{rad}$.

If the bubble experiences a temperature perturbation, $\Delta T = T_e - T_{rad} > 0$ then, since $\Delta P = P_e - P_{rad} = 0$ as the pressure equilibrium is restored at the local sound speed, the bubble will experience also a density perturbation $\Delta\rho = \rho_e - \rho_{rad} < 0$. Under this perturbation the bubble moves upward with an acceleration a due to buoyancy, satisfying

$$\rho a = -g\Delta\rho, \qquad a = -g\frac{\Delta\rho}{\rho} \tag{2.20}$$

where g is the local acceleration of gravity. After moving a distance dr (positive), the density difference of the bubble and the surroundings becomes

$$\Delta\rho(r + dr) = \Delta\rho(r) + dr \cdot \frac{d\Delta\rho}{dr}, \tag{2.21}$$

in this formula, $\Delta\rho(r) < 0$, $dr > 0$. Thus, if $\frac{d\Delta\rho}{dr} \leq 0$, then $\Delta\rho(r + dr) < 0$, which means the density of the bubble is still smaller than that of the surroundings, and the bubble will continue to move up. Inversely, if $\frac{d\Delta\rho}{dr} > 0$, the bubble will slow down and eventually stop because of bearing an opposite force. Therefore, convection occurs when this condition

$$\frac{d\Delta\rho}{dr} \leq 0, \tag{2.22}$$

is satisfied.

As we know from the EOS,

$$\rho = \rho(P, T, \mu), \tag{2.23}$$

we have

$$dln\rho = \alpha dlnP - \delta dlnT + \varphi dln\mu, \tag{2.24}$$

where

$$\alpha = (\frac{\partial ln\rho}{\partial lnP})_{T,\mu}, \qquad \delta = -(\frac{\partial ln\rho}{\partial lnT})_{P,\mu}, \qquad \varphi = (\frac{\partial ln\rho}{\partial ln\mu})_{P,T} \tag{2.25}$$

$\alpha = \delta = \varphi = 1$ for the perfect gas with negligible radiation.

For the bubble, the molecular weight is always the same along the displacement dr, as there is no matter exchange with the surroundings. Thus, $dln\mu_e = 0$, and we have

$$\frac{dln\rho_e}{dr} = \alpha\frac{dlnP_e}{dr} - \delta\frac{dlnT_e}{dr}, \tag{2.26}$$

for the surroundings,

$$\frac{dln\rho_{rad}}{dr} = \alpha\frac{dlnP_{rad}}{dr} - \delta\frac{dlnT_{rad}}{dr} + \varphi\frac{dln\mu_{rad}}{dr}, \tag{2.27}$$

(2.26) - (2.27), we obtain

$$\frac{d}{dr}(\Delta ln\rho) = \frac{dln\rho_e}{dr} - \frac{dln\rho_{rad}}{dr} = \delta(\frac{dlnT_{rad}}{dr} - \frac{dlnT_e}{dr}) - \varphi\frac{dln\mu_{rad}}{dr}. \tag{2.28}$$

(2.22) is equal to

$$\frac{dlnT_{rad}}{dr} \leq \frac{dlnT_e}{dr} + \frac{\varphi}{\delta}\frac{dln\mu_{rad}}{dr}. \tag{2.29}$$

Introducing a quantity $H_{\rm P}$,

$$\frac{1}{H_P} \equiv -\frac{dlnP}{dr}, \tag{2.30}$$

$H_{\rm P}$ is called the local pressure scale height, and it is equal to the displacement of the bubble when its pressure changes by a factor of e. P decreases as r increases, thus $H_{\rm P} > 0$.

Multiple $H_{\rm P}$ on both sides of equation (2.29), we get

$$(\frac{dlnT}{dlnP})_{rad} \geq (\frac{dlnT}{dlnP})_e + \frac{\varphi}{\delta}\frac{dln\mu_{rad}}{dP}, \tag{2.31}$$

define

$$\nabla_{rad} \equiv (\frac{dlnT}{dlnP})_{rad}, \tag{2.32}$$

$$\nabla_e \equiv (\frac{dlnT}{dlnP})_e, \tag{2.33}$$

and

$$\nabla_\mu \equiv \frac{\varphi}{\delta}\frac{dln\mu_{rad}}{dP} = -(\frac{\partial ln\rho}{\partial lnT})^{-1}_{P,\mu}(\frac{\partial ln\rho}{\partial ln\mu})_{P,T}(\frac{dln\mu_{rad}}{dlnP}), \tag{2.34}$$

where ∇_{rad} is radiative temperature gradient and ∇_μ is molecular weight gradient. Assuming the motion of the bubble is adiabatic, ∇_e can be rewritten as ∇_{ad}, i.e. adiabatic temperature gradient. Thus the condition for the onset of convection is

$$\nabla_{rad} \geq \nabla_{ad} + \nabla_\mu, \tag{2.35}$$

which is called the *Ledoux criterion*. In a region with homogeneous chemical composition, $\nabla_\mu = 0$, as

you'd expect, it becomes the *Schwarzschild criterion*,

$$\nabla_{rad} \geq \nabla_{ad}. \tag{2.36}$$

Notice that in deriving this condition, effects of viscosity have been neglected. It can be seen that this is a very good approximation for stellar matter in normal conditions.

2.1.3 Convective overshooting

When adopting the Schwarzschild criterion, the region where $\nabla_{rad} > \nabla_{ad}$ is unstable and convective, whereas the region where $\nabla_{rad} < \nabla_{ad}$ is stable and radiative. Hence, the convective border is usually determined by the equality $\nabla_{rad} = \nabla_{ad}$, and this border is called the *Schwarzschild border*. However, when a bubble arrives at this border, its velocity $v \neq 0$, though the acceleration $a = -g\frac{\Delta\rho}{\rho} = 0$, so the bubble will go further into the stable region. As the bubble receives a force opposite to the direction of its motion, the velocity will decrease until zero, so the border where $v = 0$ should be the real convective border. The region between the borders determined by $\nabla_{rad} = \nabla_{ad}$ and $v = 0$ is called the *overshooting* region.

The size of the overshooting region is one of the most uncertain parameters in stellar evolution and the effects of overshooting have been thoroughly analyzed by many authors. We may distinguish two main regions where overshooting may be important in stellar evolution, at the border of the convective core during central H and He burning, and at the base of the convective envelope when the star is a red giant or supergiant.

Core overshooting (CO)

Much theoretical and observational work supports the existence of core overshooting (Bressan et al. 1981; Bertelli et al. 1985, 1990). The effect of core overshooting is that of increasing the size of the mixed region, with respect to the models where it is neglected. With core overshooting during central H burning the star becomes more luminous and evolves down to lower effective temperatures, as shown in Figure 2.1. This is the so called "main sequence widening" which can be used to calibrate the size of the effect by comparing predicted and observed star counts in the CMD around the turn-off of star clusters. This kind of calibration, made on several open clusters by different authors, provides a rough estimate of the size of the overshooting region around the convective core which, expressed in terms of the pressure scale height, turns out to be $L_{Overshoot} \simeq 0.25 H_P$. This is the value commonly adopted in many stellar evolution models.

Envelope overshooting (EO)

Concerning the overshooting at the base of the convective envelope, there is no widely accepted consensus. The consideration of envelope overshooting in stellar models was first suggested by Alongi et al. (1991). There are two relevant observational constraints: the location of RGB bump in globular clusters and old

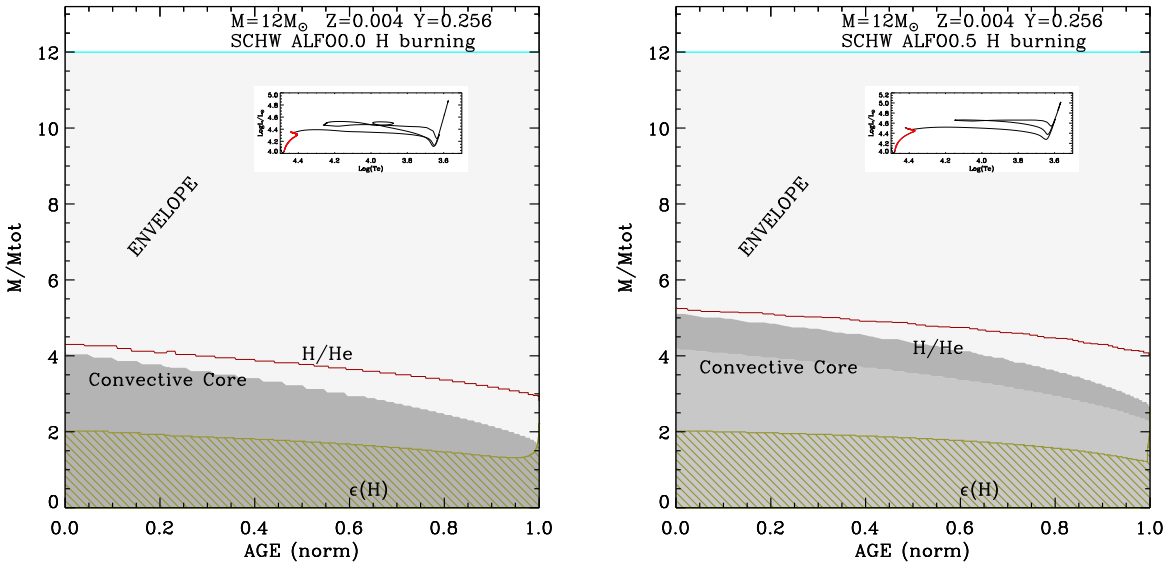

Figure 2.1: Kippenhahn diagrams of central H-burning stars of M=12$M_{\odot}$and Z=0.004 without core overshooting (left panel) and with CO=0.5$H_{\rm P}$ (right panel). A larger He core is left after H exhaustion if taking into account core overshooting.

open cluster, and the extension of blue loops in intermediate- and high-mass stars. Both features have been found to be best explained by a moderate amount of overshooting *below the border of the unstable region*, of about EO=0.25-1.0, in units of $H_{\rm P}$. For illustration, we refer to Figure 2.2 from Bressan et al. (2013). We see that in models with larger EO, the RGB bump is typically $\sim$ 0.3 mag fainter than in models with negligible EO. This is consistent with observations which found the RGB bump in Galactic globular clusters is about 0.2-0.4 mag fainter than that predicted by models without EO (Di Cecco et al. 2010; Cassisi et al. 2011). On the other hand, we can also calibrate the envelope overshooting by means of the blue loop excursions, which is carried out in this thesis.

More recently a similar mechanism has been invoked to improve the agreement with the physical state of matter in the convective-radiative transition region derived from solar oscillation data (Christensen-Dalsgaard et al. 2011). In some cases a large envelope overshooting (EO=2.0-4.0, in units of $H_{\rm P}$) is used to enhance the efficiency of the carbon dredge up during the thermally pulsing Asymptotic Giant Branch phase (Kamath et al. 2012).

2.2 New evolutionary tracks of massive stars with *PARSEC*

The largest value of initial mass in the previously published set of evolutionary tracks computed with *PARSEC* V1.1 is M=12$M_{\odot}$. The corresponding hydrogen burning lifetime is about 15Myr. To simulate younger and most massive stars we usually resort to our previous database (Bressan et al. 1993; Fagotto et al. 1994a,b,c). Since our stellar evolution code has been deeply revised recently (Girardi et al. 2000; Bressan et al. 2012, 2013), we present here new sets of evolutionary tracks of massive stars computed with the *PARSEC* code. The masses range from M=14$M_{\odot}$to M=350$M_{\odot}$and the evolution is followed from the pre-main sequence phase to the beginning of the carbon-burning phase. Together with the

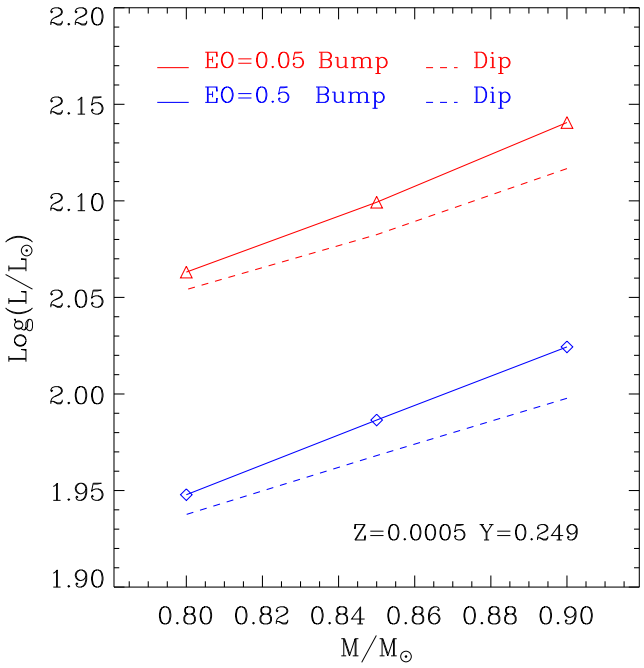

Figure 2.2: The RGB bump computed by models with EO=0.05H_P (red) and EO=0.5H_P (blue). The RGB bump in models with larger EO is typically $\sim$ 0.3 mag fainter than in models with negligible EO. This figure is from Bressan et al. (2013).

already published stellar evolution tracks the database now includes updated and homogeneous sets of evolutionary tracks from very low (M=0.1$M_\odot$) to very massive (M=350$M_\odot$) stars, from the pre-main sequence to the beginning of central carbon burning. Here we describe the models with low metallicity, Z=0.001 to Z=0.004, that will be used in Section 4 to build simulated CMDs for comparison with those of three dwarf irregualr galaxies of similar metallicity. Models for lower metallicity will be presented in Section 5, while models with higher metallicity will be discussed in future.

2.2.1 Constitutive equations

The *PARSEC* code is extensively discussed in Bressan et al. (2012, 2013) and Chen et al. (2014); here we briefly describe the most important updates to the constitutive equations. The equation of state (EOS) is computed with the FreeEOS code (A.W. Irwin, [1]). Opacities in the high-temperature regime, $4.2 \leq \log(T/\mathrm{K}) \leq 8.7$, are obtained from the Opacity Project At Livermoren(OPAL) (Iglesias & Rogers 1996), while in the low-temperature regime, $3.2 \leq \log(T/\mathrm{K}) \leq 4.1$, we use opacities generated with our ÆSOPUS[2] code (Marigo & Aringer 2009). Conductive opacities are included following Itoh et al. (2008). The nuclear reaction network consists of the p-p chains, the CNO tri-cycle, the Ne–Na and Mg–Al chains and the most important α-capture reactions, including the α-n reactions. The reaction rates and the corresponding Q-values are taken from the recommended rates in the JINA database (Cyburt et al. 2010). Electron screening factors for all reactions are from Dewitt et al. (1973) and Graboske et al.

[1] http://freeeos.sourceforge.net/
[2] http://stev.oapd.inaf.it/aesopus

(1973). Energy losses by electron neutrinos are taken from Munakata et al. (1985) and Itoh & Kohyama (1983) and Haft et al. (1994). The outer boundary conditions are discussed in Chen et al. (2014). The reference solar partition of heavy elements is taken from Caffau et al. (2011) who revised a few species of the Grevesse & Sauval (1998) compilation (GS98). According to Caffau et al. (2011), the present-day Sun's metallicity is $Z_\odot = 0.01524$, intermediate between the most recent estimates, e.g. $Z_\odot = 0.0141$ of Lodders et al. (2009) or $Z_\odot = 0.0134$ of Asplund et al. (2009) (AGSS), and the previous value of $Z_\odot = 0.017$ by GS98.

2.2.2 Convection and mixing

The convective energy transport is described according to the mixing-length theory of Böhm-Vitense (1958), with the mixing length parameter $\alpha_{\rm MLT}$ calibrated on the solar model, $\alpha_{\rm MLT} = 1.74$. The location of the boundary of the convective core of massive stars is estimated according to Bressan et al. (1981) taking into account overshooting from the central unstable region. As thoroughly described in Bressan et al. (2013), the main parameter describing core overshooting is the mean free path of convective elements *across* the border of the unstable region, expressed in units of pressure scale height, $l_{\rm c}{=}\Lambda_{\rm c} H_{\rm P}$. The overshooting parameter used in the core, $\Lambda_{\rm c} = 0.5$, is the result of the calibration obtained by the analysis of intermediate age clusters (Girardi et al. 2009) as well as individual stars (Kamath et al. 2010; Deheuvels et al. 2010; Torres et al. 2014). Note that the overshooting region obtained with this formalism extends over about $0.5 l_{\rm c}$ *above* the unstable region. Instability against convection is tested by means of the Schwarzschild criterion. An alternative criterion is that of Ledoux, which takes into account the effects of the gradient in the mean molecular weight. The comparisons between these two criteria will be made in Section 2.2.6. In the present work we opt for the Schwarzschild criterion, which is more appropriate to account for the effects of thermal dissipation, according to Kato (1966).

Overshooting at the base of the convective envelope (EO) can also give rise to sizable extra-mixing. In the past, two important observational effects have been related to this phenomenon, the location of the bump in the red giant branch of low mass stars (RGB bump seen in the CMD of globular clusters and old open clusters) and the extent of the blue loops of intermediate-mass stars (Alongi et al. 1991). Both features have been found to be best explained by a moderate amount of overshooting *below the border of the unstable region*, of about EO=0.25-1.0, in units of $H_{\rm P}$. The standard value for intermediate-mass and massive stars used in *PARSEC* V1.1 is EO=$0.7 H_{\rm P}$. However, as we will see later, with this value it turns out to be difficult to reproduce the extended blue loops seen in the metal-poor dwarf galaxies, therefore we have computed two additional sets of models increasing the *EO* to match the observed extended blue loops. We adopted EO=$2 H_{\rm P}$ and EO=$4 H_{\rm P}$. These additional sets will be discussed in Section 2.2.5.

2.2.3 Mass-loss rates

Mass loss is not considered for masses below $12 M_\odot$, in the *PARSEC* V1.1 tracks, but it cannot be neglected for larger masses. In this section we describe the algorithm used for the new sets of massive star models, obtained by combining several prescriptions found in literature for the different spectral

types.

In the Blue Super Giant (BSG) phases ($T_{\rm eff} \geq$ 12000 K) we adopt the relations provided by Vink et al. (2000, 2001). This formulation, that we name R_{V01}, shows an overall dependence of the mass-loss rate on the metallicity, of the kind $\dot{M} \propto (Z/Z_{\odot})^{0.85} M_{\odot}$/yr. For the red supergiant stars ($T_{\rm eff} <$ 12000 K) we adopt the relations provided by de Jager et al. (1988), R_{dJ}. We assume the same dependence on the surface metallicity as in R_{V01}. In the Wolf-Rayet (WR) phases we use the Nugis & Lamers (2000) formalism, with its own dependence on the stellar metallicity (R_{NL}).

A relevant aspect for the more massive stars concerns the transition between O-type phase to the Luminous Blue Variable (LBV) and Red Super Giant (RSG) phases and finally to the WR phase and, equally important, the dependence of this transition upon the surface metallicity of the star. In Bressan et al. (1993) as an example of the Padova models, but generally also in evolutionary computations made by other groups, the transition to the super-wind phase corresponding to the LBV stage is artificially set when the models cross the Humphreys & Davidson (1979) instability limit in the HR diagram. During this phase, at solar metallicity, the mass-loss rates reach values of $\dot{M} \simeq 10^{-3} M_{\odot}$/yr. In the previous Padova models this limit is set independently from the metallicity of the galaxy, though the mass-loss rates themselves do depend on the abundance of heavy elements as indicated above. More recently however, the behaviour of the mass-loss rates around this transition has been thoroughly analyzed by Gräfener & Hamann (2008) and by Vink et al. (2011). They find that the mass-loss rates are strongly enhanced when the stars approach the Eddington limit,

$$\Gamma = \frac{kL}{4\pi cGM} = 1 \tag{2.37}$$

where the symbols have their usual meaning. We have thus included in our formalism the explicit dependence of the mass-loss rates from the ratio of the star luminosity to the corresponding Eddington luminosity, Γ, as described by Vink et al. (2011) for solar metallicity. It is worth noticing that, by including this dependence on the mass-loss rates, we are able to reproduce the observed Humphreys-Davidson transition limit at solar metallicity (Chen et al. 2015). However, to extend this behaviour to different galactic environments we need to know how the metallicity affects mass-loss rate, near the Eddington limit. This has been thoroughly analyzed by Gräfener & Hamann (2008) in a broad metallicity range, $10^{-3}\ Z_{\odot} \leq\ Z \leq\ 2\ Z_{\odot}$, but only for the case of Wolf Rayet stars, and by Muijres et al. (2012) who investigate the dependence of mass-loss rate on the CNO abundances. The analysis of Gräfener & Hamann (2008) shows that the dependence of the mass-loss rate on the metallicity is also a strong function of Γ. While at low values of Γ the mass-loss rate obeys the relation $\dot{M} \propto (Z/Z_{\odot})^{0.85} M_{\odot}$/yr, at increasing Γ the metallicity dependence becomes weaker , and it disappears as Γ approaches 1. In absence of a more comprehensive analysis of the dependence of the mass-loss rates on the surface metallicity and Γ, we have adopted the results of Gräfener & Hamann (2008). In brief, we assume that the mass-loss rates scale with the metallicity as

$$\dot{M} \propto\ (Z/Z_{\odot})^{\alpha}, \tag{2.38}$$

with the coefficient α determined from a fit to the published relationships by Gräfener & Hamann (2008)

$$\begin{aligned} \alpha &= 0.85 && (\Gamma < 2/3) \\ \alpha &= 2.45 - 2.4 \times \Gamma && (2/3 \leq \Gamma \leq 1) \end{aligned} \tag{2.39}$$

In summary, our algorithm for the mass-loss rates in different evolutionary phases and metallicities is the following. Besides the already specified mass-loss rate formulation R_{V01} we compute also the dependence on Γ, using the tables provided by Vink et al. (2011), R_{Γ}. However, we scale R_{Γ} with the metallicity, using Equation 2.38 and 2.39.

During the phases BSGs, LBVs and RSGs we adopt the maximum between R_{V01}, R_{dJ} and R_{Γ}. When the stars enter the Wolf-Rayet phase, which we assume to begin when the surface Hydrogen fraction falls below $X = 0.3$ and the effective temperature $T_{\rm eff}$> 30000 K, we consider also the Nugis & Lamers (2000) formulation and we adopt the maximum $\dot{M}$ between R_{V01}, R_{dJ}, R_{Γ} and R_{NL}, after scaling each rate with metallicity using the appropriate scaling law. In this way we also obtain a smooth transition between the mass-loss rates in the different evolutionary phases.

2.2.4 The evolution across the HR diagram

In Figures 2.3-2.8 we plot the HR diagrams of our new evolutionary tracks of massive stars together with those of intermediate-mass stars, for three different values assumed for the envelope overshooting, EO=0.7$H_{\rm P}$ (the standard *PARSEC* V1.1 value), EO=2$H_{\rm P}$ and EO=4$H_{\rm P}$, and for two different values of the chemical composition, Z=0.001 and Z=0.004, respectively. For each evolutionary track, the central hydrogen burning phase is colored in blue, the central helium burning phase in green and the contraction phases in red while, for sake of clarity, the pre-main sequence phase is not reproduced.

The black lines at the highest luminosities show the Humphreys & Davidson (1979) limit. This limit marks the region of the HR diagram where, at near solar metallicity, there are no observed supergiant stars. The lack of supergiant stars in this region is interpreted as a signature of the effects of enhanced mass-loss rates when the star enter this region. This interpretation is supported by the presence, around this limit, of LBV stars which are known to be characterized by high mass-loss rates. Indeed, the Humphreys & Davidson (1979) limit is well reproduced by our new models at near-solar metallicity, due to the boosting of mass-loss rates near the Eddington limit (Chen et al. 2015). However, at the metallicities investigated in this work, Z=0.001 and Z=0.004, the boosting is mitigated by the reduction factor introduced by Eq. 2.38 and Eq. 2.39. At Z=0.001 the upper main sequence widens significantly and the more massive stars, because of their very large convective cores, evolve in the "forbidden" region even during the H-burning phase. They also ignite and burn central helium as "red" super-giant stars. Notice that the most massive stars begin the main sequence already within the "forbidden" region. At larger metallicity, Z=0.004, the widening of the upper main sequence begins at lower luminosity because of the larger opacities of the external layers but, at the same time, the effects of the mass-loss enhancement near the Eddington limit are more relevant. For both metallicities, in the most massive stars the mass-loss rates are high enough to peal off a significant fraction of the hydrogen rich envelope and the stars exhaust

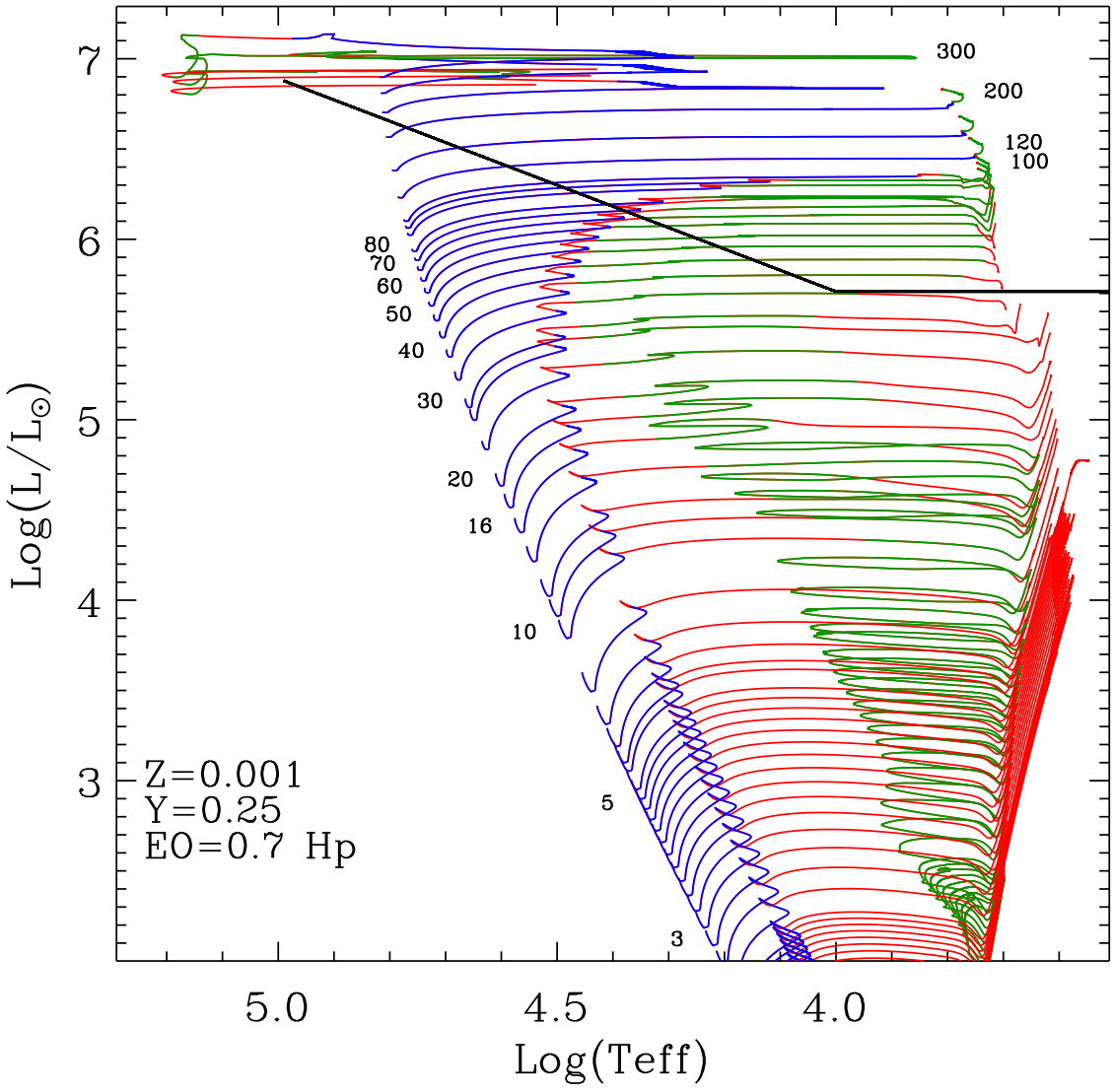

Figure 2.3: New *PARSEC* evolutionary tracks of massive stars together with already published tracks of intermediate-mass stars for Z=0.001 with EO=0.7$H_{\rm P}$. The mass range shown is between about 3 $M_{\odot}$and 350 $M_{\odot}$. The color codes blue, green and red, highlight the central H-burning, central He-burning and expansion/contraction phases, respectively. A few tracks are labelled with the initial mass. The black lines indicates the observed Humphreys & Davidson (1979) transition limit at solar metallicity.

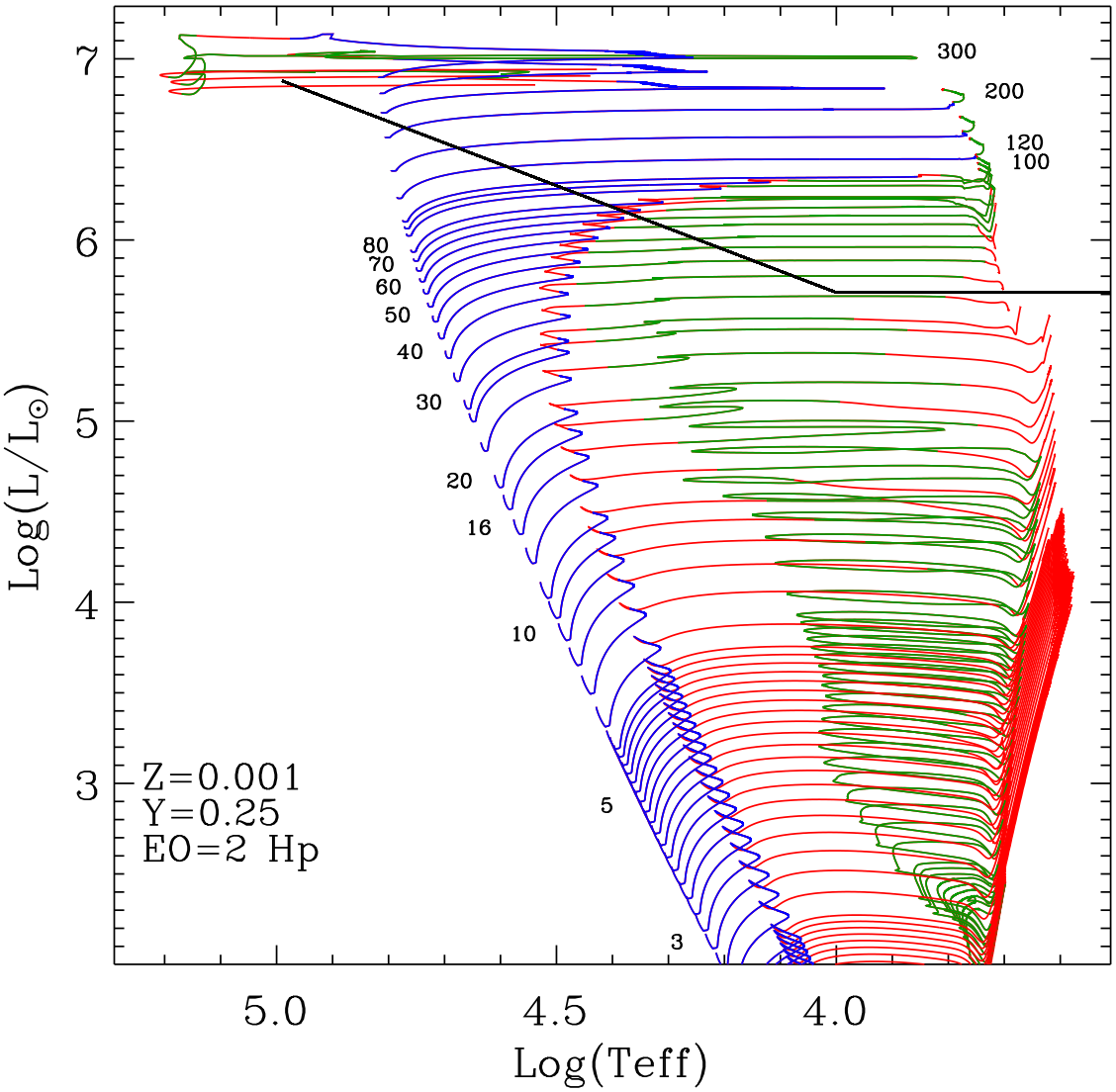

Figure 2.4: New *PARSEC* evolutionary tracks of massive stars together with already published tracks of intermediate-mass stars for Z=0.001 with EO=2$H_{\rm P}$.

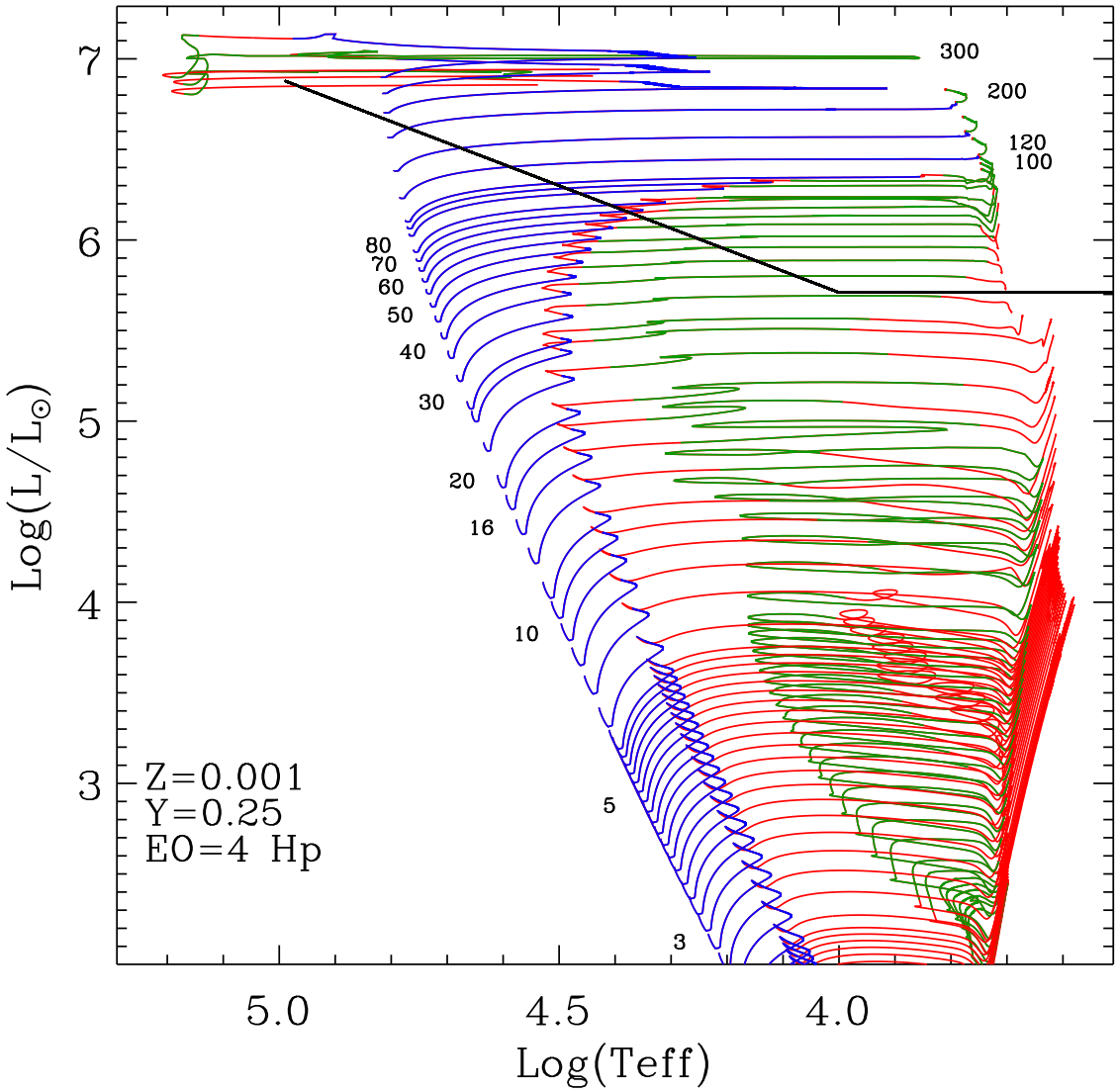

Figure 2.5: New *PARSEC* evolutionary tracks of massive stars together with already published tracks of intermediate-mass stars for Z=0.001 with EO=4$H_{\rm P}$.

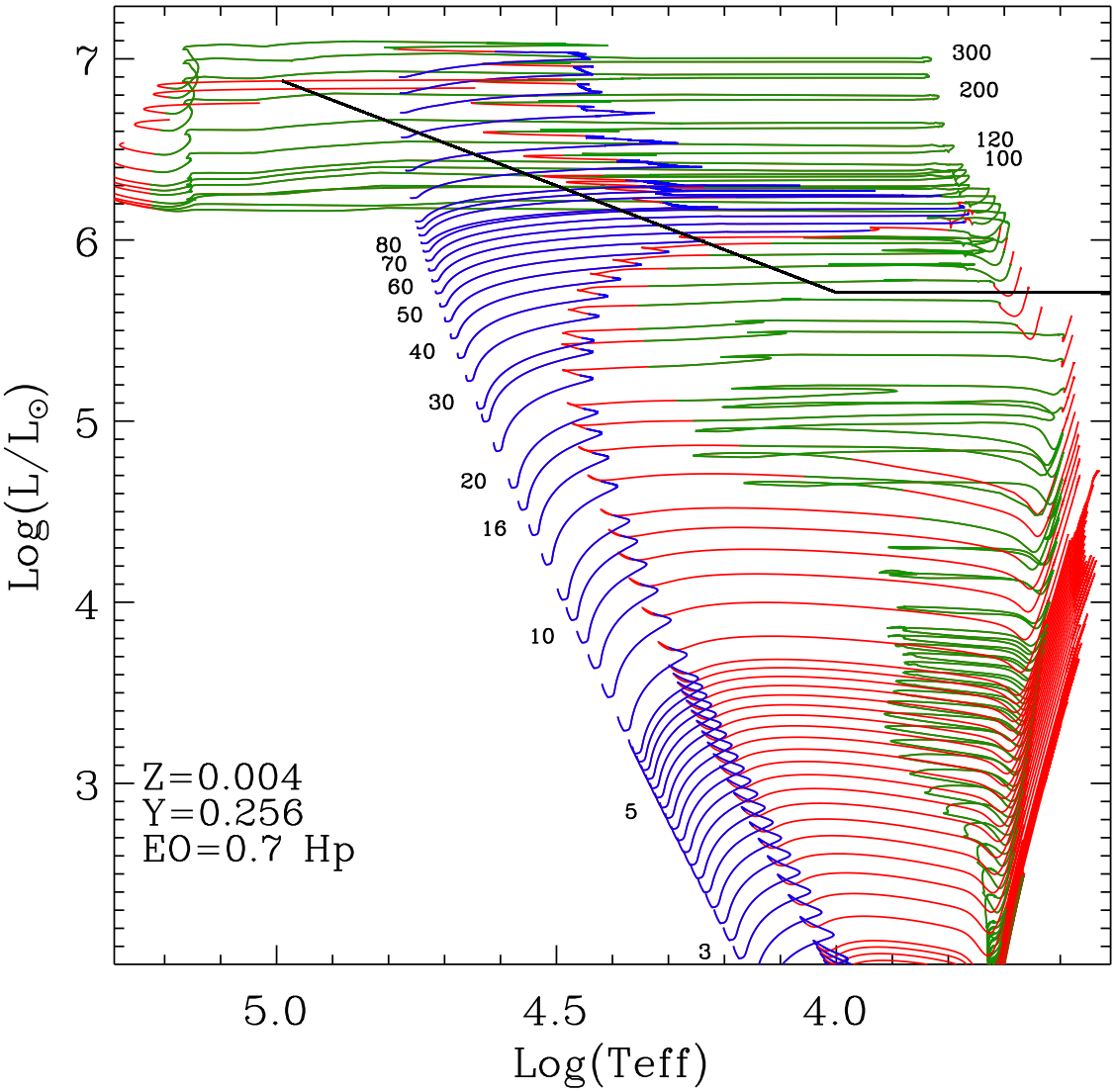

Figure 2.6: New *PARSEC* evolutionary tracks of massive stars together with already published tracks of intermediate-mass stars for Z=0.004 with EO=0.7$H_{\rm P}$.

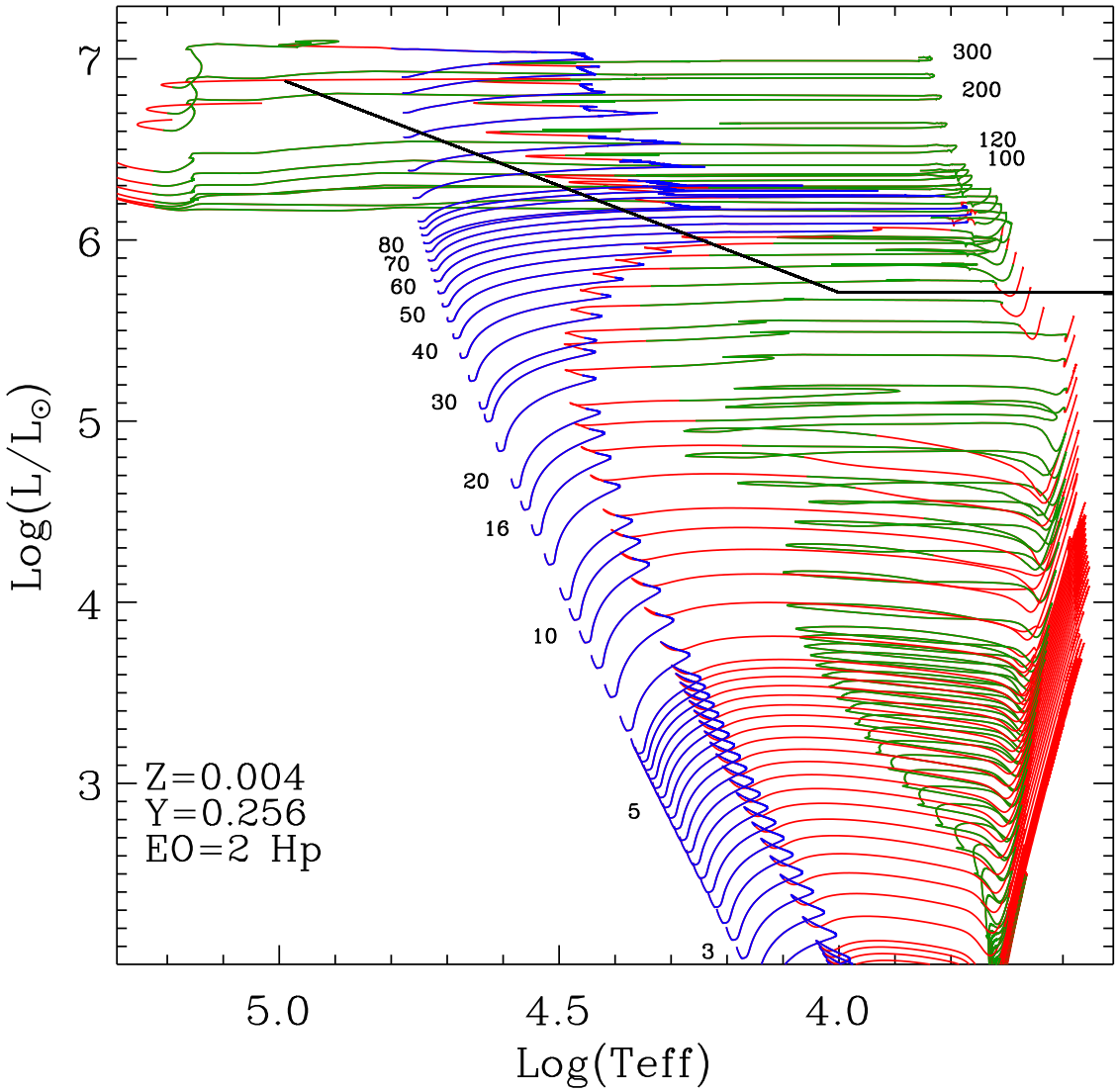

Figure 2.7: New *PARSEC* evolutionary tracks of massive stars together with already published tracks of intermediate-mass stars for Z=0.004 with EO=2$H_{\rm P}$.

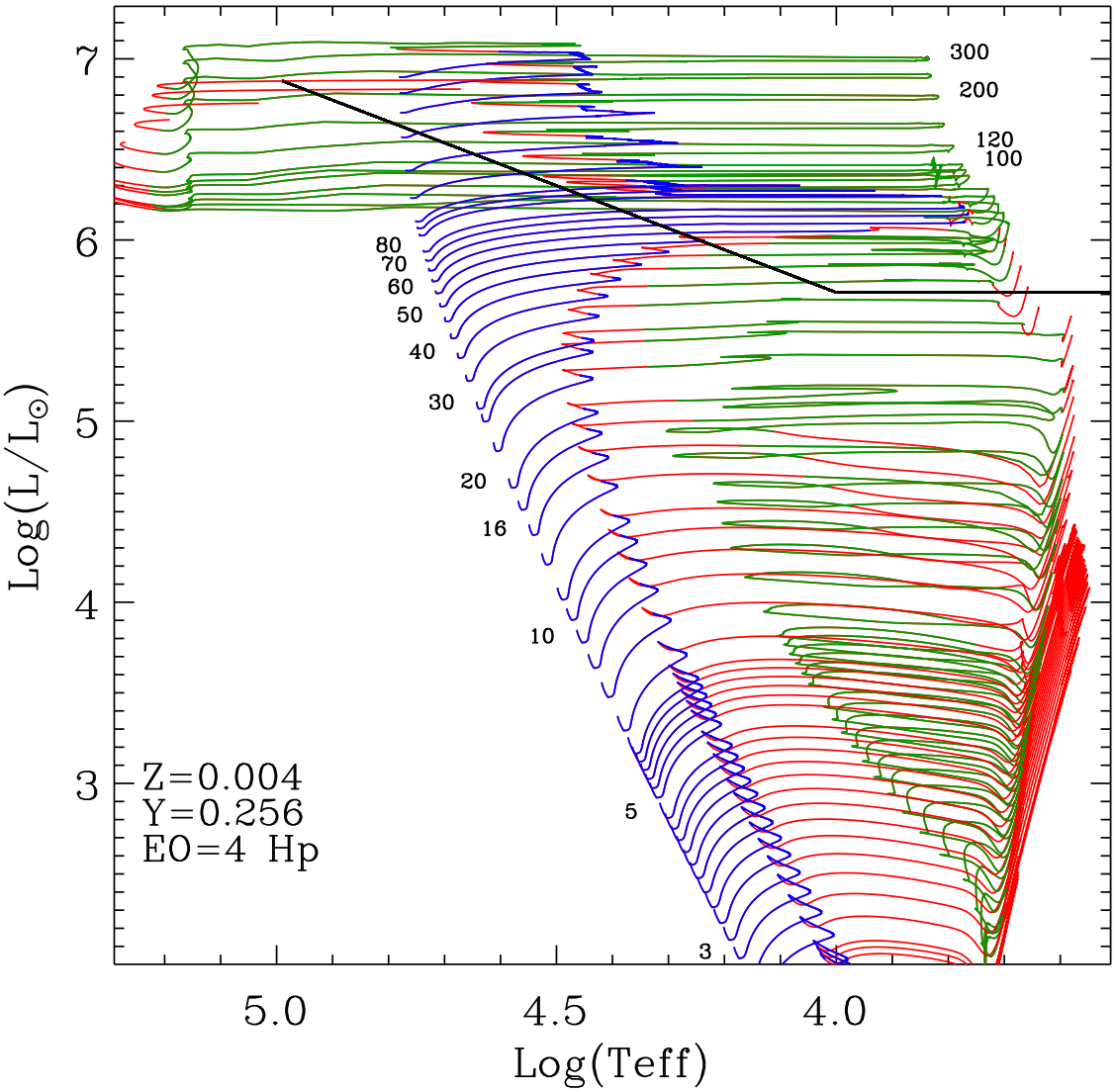

Figure 2.8: New *PARSEC* evolutionary tracks of massive stars together with already published tracks of intermediate-mass stars for Z=0.004 with EO=4H_P .

central Hydrogen near the Humphreys & Davidson (1979) limit. Nevertheless, after central He ignition the stars still move toward the red supergiant phase, until mass loss peals off the entire envelope and the stars evolve back, toward the Wolf Rayet phase. This effect is more evident at higher metallicity.

At lower luminosities the intensity of mass-loss is lower and it cannot more affect the surface evolution of the stars. There is an intermediate region in the HR diagram where stars ignite helium burning near the main sequence and then evolve toward the RSG phase. At decreasing initial mass, central He ignition shifts toward the RSG phase and the path of the stars in the HR diagram becomes similar to that of intermediate-mass stars, with the presence of blue loops during the central helium burning phase. In general the blue loops are wider for higher initial mass, indicating the existence of a bifurcation in the central Helium burning sequences that begins at intermediate-mass stars and persists up to the massive stars. Together with the main sequence, these sequences are the most distinct features in the CMDs of star forming galaxies and constitute the anchors of any study based on the simulated CMD. On simple grounds they can be explained by considering equilibrium structures made by a helium core and a non negligible outer hydrogen-rich envelope. In the HR diagram these equilibrium structures are expected to lie between the main sequence and the Hayashi line (Lauterborn et al. 1971). They lie near the main sequence when the helium core is negligible, and near the Hayashi line when the virial temperature of the helium core, $\propto \Phi = M_C/R_C$ with M_C and R_C being the mass and radius of the helium core, is larger than a critical threshold. The latter depends on the mass of the star, the chemical composition, some reaction rates and possibly other input physics such as internal mixing, rendering the morphology of the loops quite dependent on several details of stellar evolution (Iben 1966; Brunish & Becker 1990; Xu & Li 2004; Weiss et al. 2005; Halabi et al. 2012). Such complex dependence makes the theoretical predictions quite difficult, especially at increasing metallicity. For example at Z=0.001 with canonical envelope overshooting (Figure 2.3), at increasing luminosity the loops become initially quite extended but then their extent decreases and thereafter increases again. This behaviour is even more marked at Z=0.004 (Figure 2.6). The loops initially become more extended at increasing mass, but above M=6.4$M_\odot$their extent decreases, and they even disappear for M=10$M_\odot$and M=11$M_\odot$. Above these masses, they fully develop again until the beginning of central He burning shifts in the yellow/blue side of the HR diagram.

2.2.5 Blue loops: the role of envelope overshooting

The reason of the presence or absence of extended blue loops during the central helium burning phase has been thoroughly investigated in the past. Among the effects that limit the extent or inhibit the appearance of blue loops, the most important one is certainly extended mixing from the core during the hydrogen burning phase, either due to overshooting(Bertelli et al. 1985) or to differential rotation (Heger & Langer 2000; Georgy et al. 2013). This effect can be understood by considering that it is more difficult for a star with a larger He core to decrease Φ below the critical value needed to begin the loop, because Φ increases with the core mass in a virialized structure, for which the radius increases with a power ($\sim$0.5) of the mass. On the other hand, it is well known that the presence of extended mixing below the bottom of the convective envelope favours the development of an extended loop (Alongi et al. 1991). To better clarify this point, we show in Figures 2.9-2.11 the evolution of the internal structure during the central helium-burning

phase, of a model with M=11$M_{\odot}$and Z=0.004, computed with canonical core overshooting and three different values of envelope overshooting EO=0.7$H_{\rm P}$ (*PARSEC* V1.1), EO=2$H_{\rm P}$ and EO=4$H_{\rm P}$. The models begin helium burning with the same internal structure, apart from the larger inward penetration of the envelope convection due to the different efficiency of the overshooting during the first dredge-up episode, which changes the location of the hydrogen/helium discontinuity (indicated in the figures by the brown horizontal line at M/M$_{tot}$ ∼0.35). By comparing the three models it turns out that the only noticeable internal difference is the size of the mass pocket between the H-burning shell and the H-He discontinuity left by the first dredge-up episode. Only the models with enhanced envelope overshooting (EO=2$H_{\rm P}$ and EO=4$H_{\rm P}$) perform an extended blue loop. The loop begins when the central hydrogen shell approaches the H-He discontinuity, in a way that reminds us of what happens to a red giant star when its internal hydrogen shell reaches the hydrogen discontinuity. Because of the high temperature dependence of the CNO reaction rates, when a discontinuity in the hydrogen profile is encountered, the structure readjusts on a thermal time-scale toward a slightly lower luminosity and a higher effective temperature Afterwards the star continues climbing the RGB on the nuclear time-scale, giving rise to the well known bump in the luminosity function. What happens in the interiors of the different models of M=11$M_{\odot}$can be seen in Figure 2.12, where we compare several quantities as a function of the evolutionary time during central helium burning. The dashed lines in the figure refer to the standard *PARSEC* V1.1 model (EO=0.7$H_{\rm P}$) while the solid line to the model with EO=4$H_{\rm P}$ (see also Figures 2.9, 2.11). While helium burning proceeds, the temperature and the density at the border of the He core continuously decrease. Once the H-burning shell approaches the H discontinuity (brown horizontal line in Figures 2.9-2.11) in the model with large EO, the density decreases and the temperature increases in a thermal time-scale. In the same time the H luminosity increases from 50% to 60% while the star shifts towards the main sequence, in the blue loop. Notice that Φ has a deep during this transition.

With the models of M=10$M_{\odot}$and M=11$M_{\odot}$for Z=0.004, with canonical core and envelope overshooting (*PARSEC* V1.1), we also analyze the importance of changing other parameters, such as the mixing length, the ^{12}C$(\alpha,\gamma)^{16}$O reaction rate (Iben 1966; Bertelli et al. 1985; Brunish & Becker 1990) and the ^{14}N$(\mathrm{p},\gamma)^{15}$O reaction rate (Xu & Li 2004; Weiss et al. 2005; Halabi et al. 2012), because these parameters are known to affect the extent of the loops. We find that by modifying these parameters within a suitable range the above models are not able to perform extended blue loops in the HR diagram. We thus conclude that the most critical parameter for the morphology of the He blue loop is the size of the mass pocket between the advancing H-burning shell and the H discontinuity left by the previous first convective dredge-up (Alongi et al. 1991; Godart et al. 2013). The earlier the shell approaches this discontinuity, the earlier the loop begins and the larger is its extent. For this reason and in view of the comparison of the new models with the observations that will be performed in the next sections, we compute additional sets of models with increased amount of envelope overshooting, i.e. with EO=2$H_{\rm P}$ and EO=4$H_{\rm P}$. The stellar evolutionary tracks with increased envelope overshooting are shown in Figures 2.4-2.5 for Z=0.001, and 2.7-2.8 for Z=0.004. As expected, after including a larger mixing at the base of the convective envelope the blue loops become more extended, though at the lower metallicity the effect is not large. In this case, only by assuming a large mixing scale (EO=4$H_{\rm P}$) the effect becomes significant. It is worth noticing

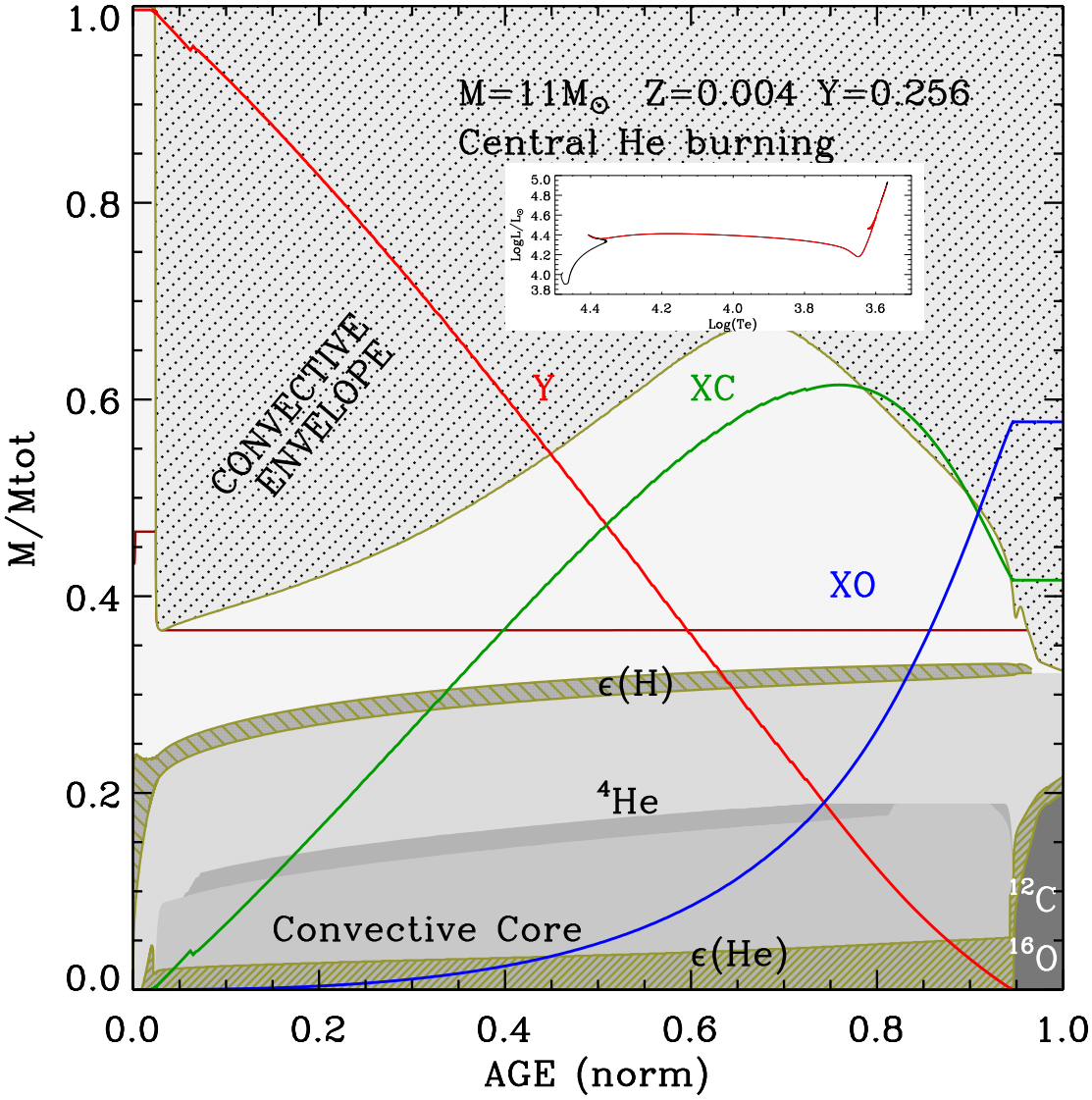

Figure 2.9: Kippenhahn diagram of central helium-burning model stars of M=11$M_{\odot}$and Z=0.004 computed with EO=0.7$H_{\rm P}$. The inset shows the corresponding evolutionary tracks in the HR diagram.

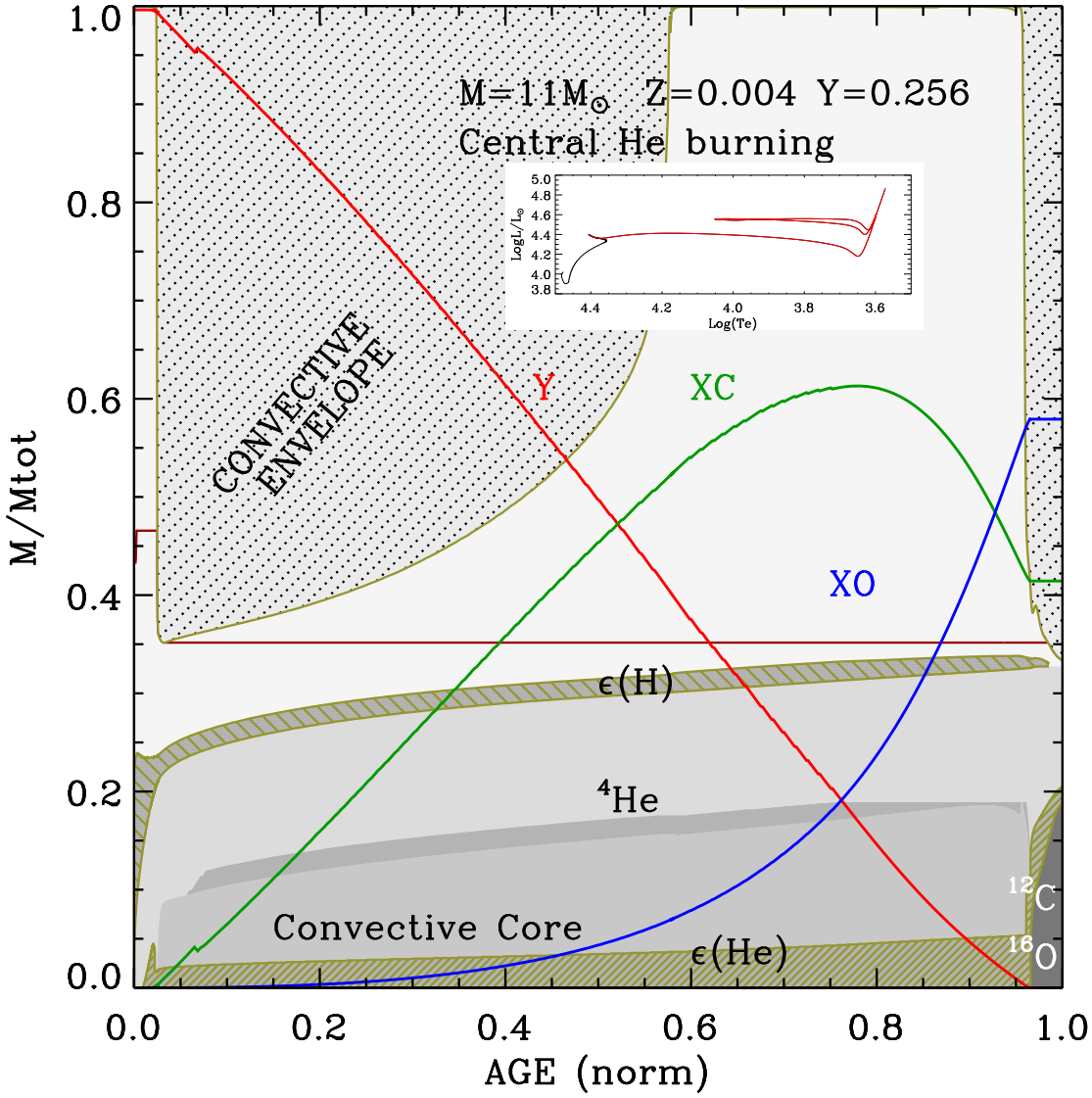

Figure 2.10: Kippenhahn diagram of central helium-burning model stars of M=11$M_{\odot}$and Z=0.004 computed with EO=2$H_{\rm P}$. The inset shows the corresponding evolutionary tracks in the HR diagram.

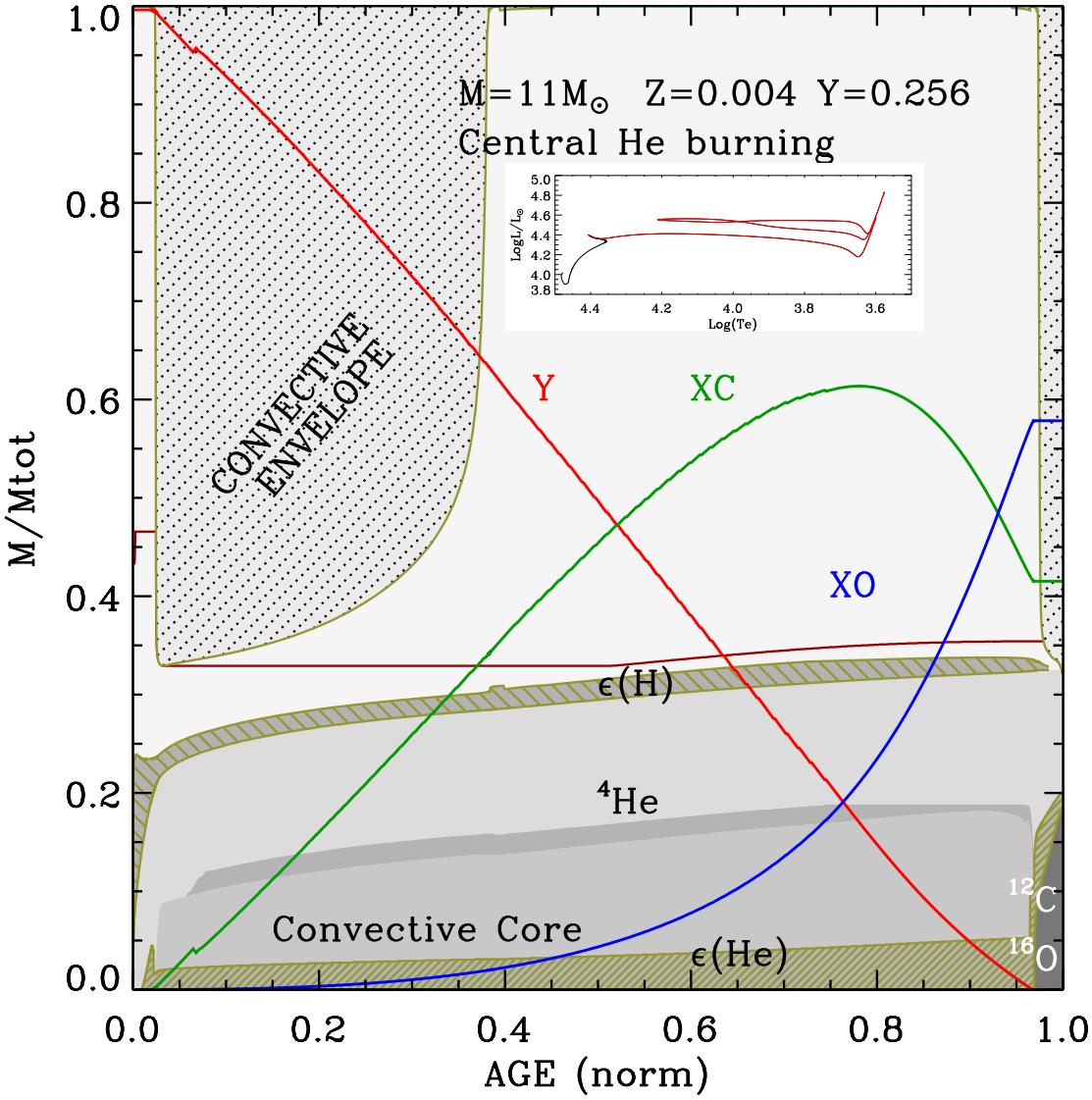

Figure 2.11: Kippenhahn diagram of central helium-burning model stars of M=11$M_{\odot}$and Z=0.004 computed with EO=4$H_{\rm P}$. The inset shows the corresponding evolutionary tracks in the HR diagram.

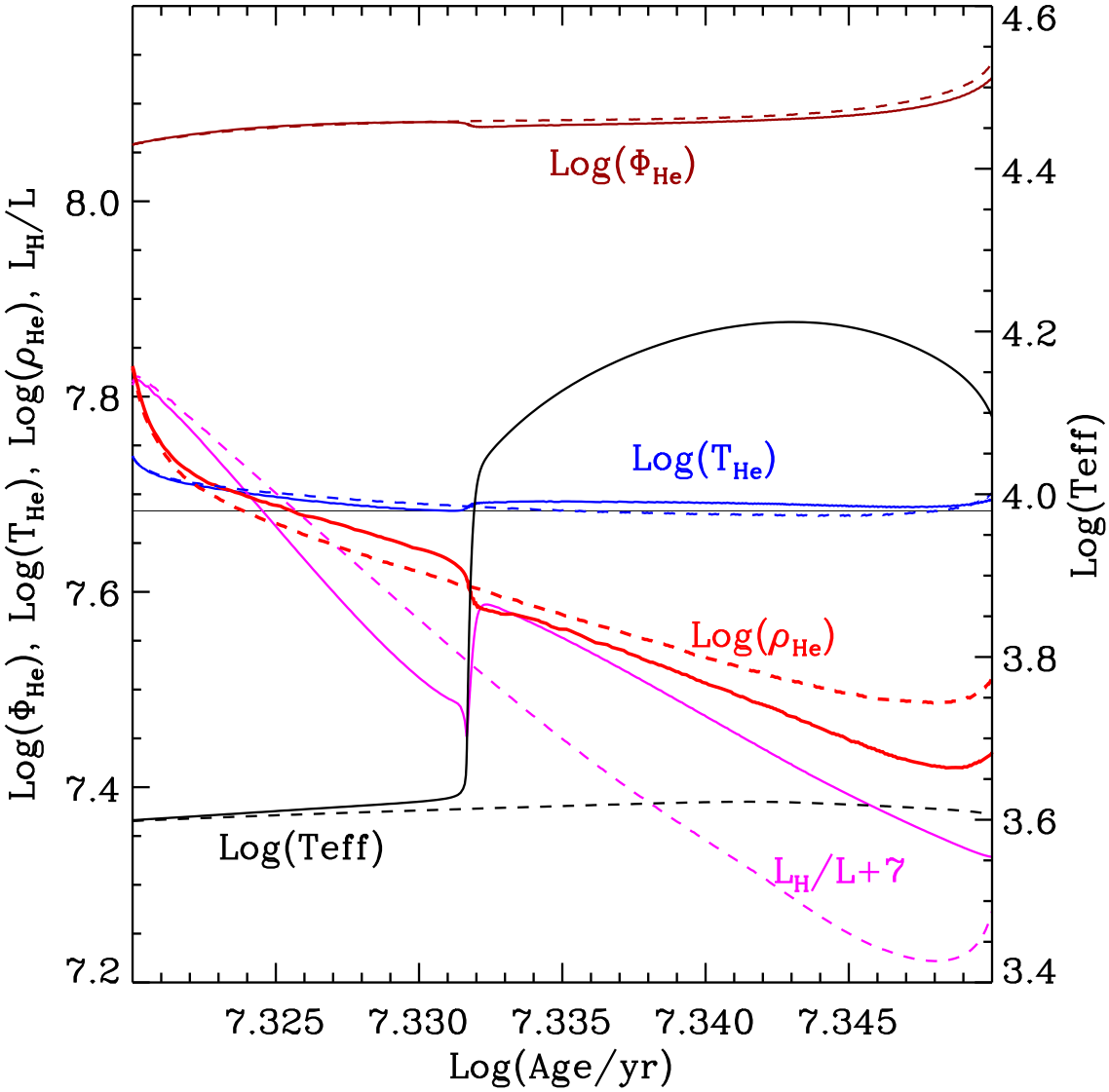

Figure 2.12: Evolution of the effective temperature and other selected internal quantities for the models of Figures 2.9, 2.11, with envelope overshooting values EO=0.7H_P (dashed lines) and EO=4H_P (solid lines), respectively.

that, though large, values of EO between $2H_P$ and $4H_P$ are not uncommon. For example they are used to enhance the efficiency of the carbon dredge up during the thermally pulsing Asymptotic Giant Branch phase (Kamath et al. 2012).

2.2.6 Blue loops and the role of different instability criteria: comparison between the Schwarzschild criterion and the Ledoux criterion

As we have discussed above, the boundary of the convective region can be determined by either the Schwarzschild criterion or the Ledoux criterion. There have been claims in literature that the use of the Ledoux criterion could eventually be more suitable in regions with variable mean molecular weight and it could give rise to more extended blue loops. This has been shown in the pioneering paper by Chiosi & Summa (1970) who investigated the effect of the above two instability criteria on the morphology of the tracks and, specifically, on the extension of the blue loops. They found that the adoption of different criteria produces different size of semi-convective regions above the unstable core, and that only the model computed with the Ledoux criterion develops a blue loop. Notably, the model computed with the Schwarzschild criterion ignites central He at high effective temperature, before reaching the red supergiant phase, and only at the end of central He burning it slowly moves toward the latter phase. The different behaviour resulting from the adoption of different instability criteria may be understood by considering the competition between two important structural properties of the model, the relative size of H-exhausted core and the mass pocket between the H-burning shell and the H-He discontinuity at the bottom of the convective envelope. As already shown in Lauterborn et al. (1971), since core overshooting during the H-burning phase has the effect of increasing the relative mass size of the H-exhausted core, it favours He ignition and burning in the red phase. On the other hand, it has been shown that the hydrostatic equilibrium location of He-burning models in the HRD is very sensitive to the mean molecular wight in the mass pocket between the H-exhausted core and the discontinuity in the H profile, left either by the development of intermediate convective regions and/or by the penetration of the convective envelope. Walmswell et al. (2015) have clearly shown that if the chemical composition of this mass pocket, which usually has an outward increasing H content, is artificially changed into a helium rich mixture, the hydrostatic location of the model shifts in the blue region of the HRD.

This explains why the blue loop starts when the H-burning shell reaches the discontinuity of mean molecular weight at the base of the H-rich envelope at early phase during the central He burning (Tang et al. 2014). Three possibilities may arise, depending on when, eventually, the H-shell reaches the H-discontinuity after central H-exhaustion. If it happens very soon during its expansion phase before the star becomes a red giant, the path in the HRD is inverted and the star ignites and burns He as a blue supergiant. Only at central He exhaustion the star will move toward the red giant phase. This behaviour may be typical of most massive stars, especially at low metallicity. It corresponds to the case B (model computed with the Schwarzschild criterion) in Chiosi & Summa (1970): that model does not perform a loop because it ignites He already in the blue loop hydrostatic configuration. The second case happens when the H-shell reaches the discontinuity after He ignition in the red (super-)giant phase, but early

enough during central He burning. In this case the star performs a blue loop in the HRD as in case A (model computed with the Leodux criterion) of Chiosi & Summa (1970). Finally if the H-shell reaches the discontinuity at late time during central He burning, the star does not perform a blue loop and burns central He entirely as a red (super-)giant. However, this behaviour is not a general property of the adopted instability criterion. To demonstrate this we show here two cases of M=12$M_{\odot}$computed with the two different instability criteria, and convective core overshooting is also considered in models. As shown in the Kippenhahn diagrams of Figure 2.13, the internal structure of the models is identical at the end of central H burning and both models are characterized by a rapid red-ward evolution followed by He ignition in the RSG phase, independently of the adopted instability criterion. The larger size of the H-exhausted core originated from the overshooting mixing forces both stars to ignite He in the supergiant phase. However, in the case of the Schwarzschild criterion (upper panel), a large intermediate convective region develops, shifting the location of the H-He discontinuity slightly deeper, as indicated by the brown horizontal line, and effectively decreasing the size of the mass pocket between the H-exhausted core and the H-He discontinuity. Instead using the Ledoux criterion (lower panel), which is more restrictive, the intermediate convective regions are smaller or even suppressed, and the resultant mass pocket is relatively larger. The difference with respect to the previous case is small, but in the former case the H-burning shell is able to reach the discontinuity and a loop occurs, while in the latter case this happens too late during He burning and the model does not perform a loop. Thus the computations shown in Figure 2.13 indicate that, in presence of sizable convective overshooting during central H-burning, the model computed with the Schwarzschild instability criterion performs the blue loop while the one computed with the Ledoux criterion spends all the He-burning lifetime in the RSG phase. We thus illustrate that the effect found by Chiosi & Summa (1970) is not a general property of the instability criterion applied to massive stars. We instead confirm that the loop is activated if the H-shell reaches the H-He discontinuity during the early He-burning phase (Tang et al. 2014). A possible explanation of why this effect triggers a blue loop has been advanced by Walmswell et al. (2015), who indicated that this is the hydrostatic equilibrium location of a class of central He-burning models with a fully discontinuous H profile.

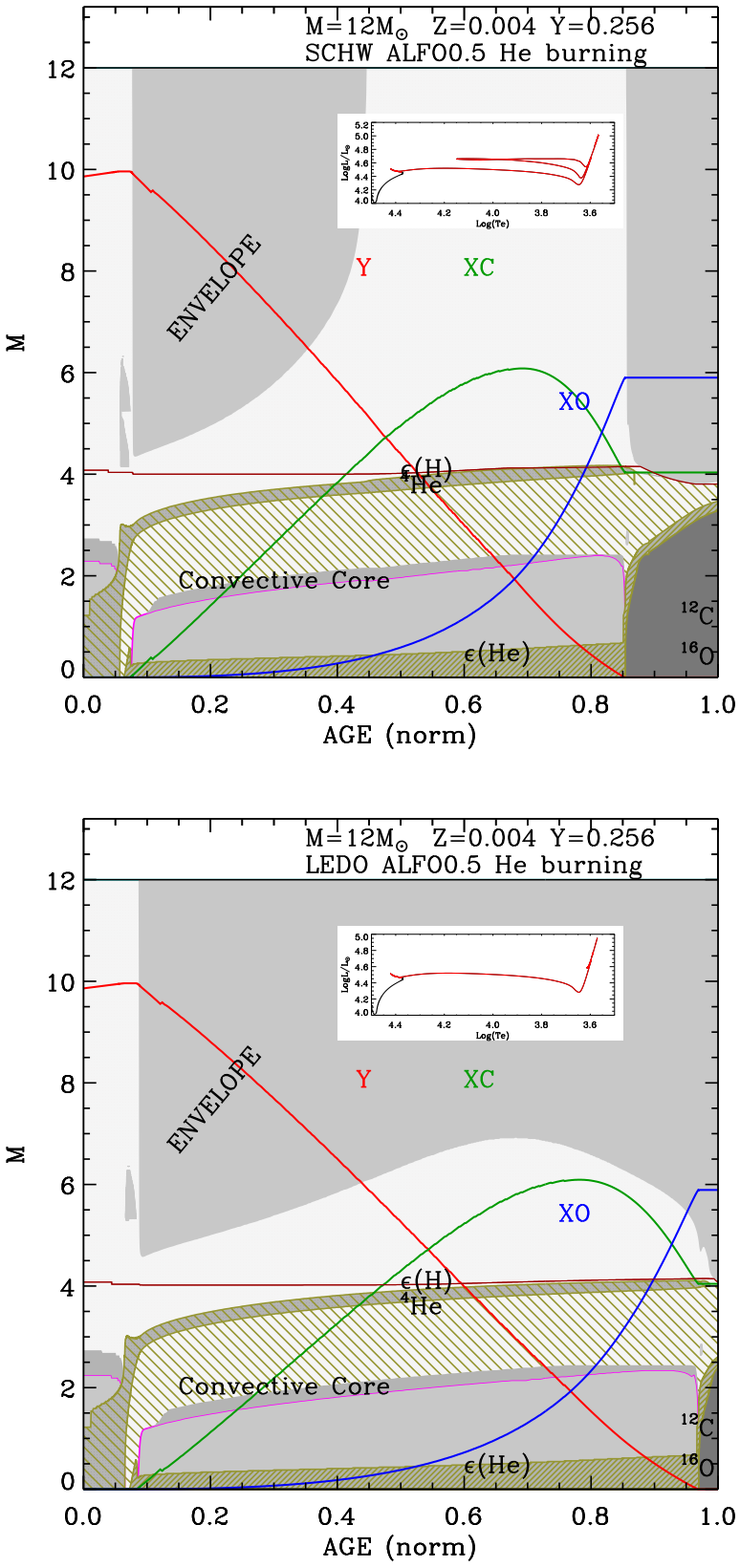

Figure 2.13: Kippenhahn diagrams of central He-burning model stars of M=12$M_{\odot}$and Z=0.004 computed with different convection criteria, the Schwarzschild criterion (upper panel) and the Ledoux criterion (lower panel). The core overshooting parameter Λ_c=0.5 is adopted. The brown line marks the location of the H-He discontinuity. The insets show the corresponding evolutionary tracks in the HR diagram.

Chapter 3

CMD simulator

To construct a synthetic color-magnitude diagram (CMD) of a stellar system, one needs to simulate the star formation history of the system, and to distribute the stars in the HR diagram, according to their age, mass and metallicity. There are already some popular CMD simulators, e.g. TRILEGAL, Besancon.

3.1 TRILEGAL

As we will use TRILEGAL to estimate the foreground contamination in observations of three dwarf irregular galaxies in Section 4.1.3, we introduce this code here in detail. Figure 1 in Girardi et al. (2005) shows the general scheme of TRILEGAL. It comprises several input quantitities. First of all, one must specify the geometry, the initial mass function (IMF), the star formation rate (SFR) and the age-metallicity relation (AMR) of the adopted Galactic stellar components. Based on the defined IMF, SFR and AMR, TRILEGAL performs a Monte Carlo simulation to generate stars randomly, and then allocates them in space according to the possibilities specified by the gemetory. At the same time, making use of tables of theoretical evolutionary tracks and of synthetic bolometric corrections, the code assigns the suitable magnitudes to these stars.

The four Galactic components taken into account in TRILEGAL are specified as follows:

- Thin disc. The star formation rate (SFR) of the thin disc is assumed that between 1 and 4 Gyr the SFR is 1.5 times larger than at other ages. Its age-metallicity relation is taken from Rocha-Pinto et al. (2000)

  Its stellar density is described by an exponential times a squared hyperbolic secant function.

$$\rho_d = C_d exp(-R/h_{R,d}) sech^2(0.5z/h_{z,d}). \tag{3.1}$$

  For the first term $exp(-R/h_{R,d})$, R is the galactocentric radius projected onto the Galaxy plane, contrained within 15 kpc from the Galaxy centre. The scale length $h_{R,d}$ is set to 2913.36 pc. For the second term $sech^2(0.5z/h_{z,d})$, the vertical scale height $h_{z,d}$ is expected to increase with stellar age t. Assuming that stars are formed at a scale height z_0 from the Galaxy plane, and then disperse vertically,

it can be expressed as $h_{z,d} = z_0(1+t/t_0)^{\alpha}$ (Rana & Basu 1992), where z_0, t_0 and α are adopted 94.6902 pc, 5.55079 Gyr and 1.6666, respectively.

The normalization constant C_d can be determined by $\Sigma_d(\odot)$, "the total surface density of thin disc stars ever formed in the Solar Neighbourhood", according to the formula proposed by Girardi et al. (2005).

$$\Sigma_d(\odot) = \int_0^{t_G} \psi_d(t)dt \int_{-\infty}^{+\infty} \rho_d(\mathbf{r})_{R=R_\odot} dz, \tag{3.2}$$

where $\psi_d(t)$ is the SFR of the thin disc and t_G is the Galaxy age. Here we take $\Sigma_d\odot = 55.4082 M_\odot/\mathrm{pc}^2$. The parameters $\Sigma_d\odot, h_R, z_0, t_0$ and α exclusively define the geometry of the thin disc.

- Thick disc. The SFR for the thick disc is assumed to be constant between 11 and 12 Gyr, and the metallcity is assumed to be Z=0.008, with a dispersion of 0.1 dex.

  Its density is also described by an exponential times a $sech^2$ function.

$$\rho_{td} = C_{td} exp(-R/h_{R,td}) sech^2(0.5z/h_{z,td}). \tag{3.3}$$

  Similarly to the thin disc, R is confined within 15 kpc from the Galaxy center and $h_{R,td}$ is set to 2394.07 pc. Since the thick disc primarily consists of old stars ($\geq$ 10 Gyr), the vertical scale height $h_{z,td}$ is considered not to vary with age, and we adopt 800 pc here. The normalization constant C_{td} is calculated according to "the total density of thick disc stars ever formed in the Solar Neighbourhood",

$$\Omega_{td}(\odot) = \rho_{td}(\mathbf{r}_\odot) \int_0^{t_G} \psi_{td}(t)dt, \tag{3.4}$$

  where $\psi_{td}(t)$ is the SFR of the thick disc. Here we take $\Omega_{td}(\odot) = 0.0010 M_\odot/\mathrm{pc}^3$. The parameters $\Sigma_{td}, h_{R,td}$ and $h_{z,td}$ define the thick disc.

- Halo. The SFR is assumed to be constant between 12 and 13 Gyr for the halo, and the metallicity distribution is taken from Ryan & Norris (1991).

  The halo can be assumed to be an oblate spheroid (Gilmore 1984)and its stellar distribution can be calculated by the deprojection of the $r^{1/4}$ law (de Vaucouleurs 1959; Young 1976). Here "r" refers to the semimajor axis in units of the effective radius within which encloses half the total luminosity. The parameters used to describe the halo and the corresponding values adopted are: the effective radius r_h = 2698.93 pc, the oblateness q_h = 0.583063, and the local "total density of halo stars ever formed in the Solar Neighbourhood" $\Omega_h(\odot) = 0.000100397 M_\odot/\mathrm{pc}^3$.

- Bulge. The bulge is assumed to be a triaxial truncated spheroid and consist of an old population formed by a single star burst about 10 Gyr ago (Vanhollebeke et al. 2009). The metallicity distribution is assumed to be [M/H] derived by Zoccali et al. (2003) + 0.3 dex.

The number density of bulge stars is given by Vanhollebeke et al. (2009):

$$\rho_b = C_b \frac{e^{-a^2/a_m^2}}{(1+a/a_0)^{1.8}}, \tag{3.5}$$

and

$$a = (x^2 + \frac{y^2}{\eta^2} + \frac{z^2}{\zeta^2})^{1/2}, \tag{3.6}$$

In the formulae above, a_m, a_0 represent the scale length and inner truncation scale lenth, respectively. The axial-ratios of the bar are: $1 : \eta(= y/x) : \zeta(= z/x)$. Additionally, two more parameters are needed to describe the Galactic bulge: the angle ϕ between the Sun-center line and the major axis of the bar, and the central "total density of bulge stars ever formed", $\Omega_b(GC)$, which is used to calibrate C_b. The adopted values for these parameters are: $a_m = 2500$ pc, $a_0 = 95$ pc, $1 : \eta : \zeta = 1 : 0.68 : 0.31$, $\phi = 15^\circ$ and $\Omega_b(GC) = 406.0 M_\odot/\mathrm{pc}^3$.

The IMF, which is the same for all the components, can be selected among different possibilities (Salpeter 1955; Kroupa 2001; Chabrier 2001). Here we assume the Chabrier (2001) log-normal function,

$$\phi_m \propto m\ exp[-\frac{(logm - logm_0)^2}{2\sigma^2}], \tag{3.7}$$

as the initial mass function. The parameters $m_0 = 0.1 M\odot$ and $\sigma = 0.627$ are the characteristic mass and dispersion, respectively. The total mass is normalized to 1, i.e.

$$\int_0^\infty m\phi_m dm = 1 M\odot, \tag{3.8}$$

so that we can express SFR in units of $M_\odot$/yr. On the other hand, in order to take into account the effect of unresolved binary systems, we assume their fraction is 30% and mass ratios are between 0.7 and 1.

As to the extinction applied to individual stars in the Galaxy, it is assumed to be described by a double-exponential decay,

$$A_V \propto exp(-|z|/h_{z,dust}) \times exp(-R/h_{R,dust}). \tag{3.9}$$

We take the scale height $h_{z,dust} = 110$ pc and the scale length $h_{R,dust} = 100$ kpc. Meanwhile, we use a total absorption at infinity $A_V(\infty)$ to calibrate the extinction, and adopt $A_V(\infty) = 0.0378$ mag. In order to calculate the absorption in each filter, A_λ, extinction curve with $R_V = 3.1$ is used to derive A_λ/A_V (Cardelli et al. 1989a).

For the photometric system, we choose HST/WFPC2 VEGAmag system, which provides information about the transmission curve S_λ and photometric zero-points. Combined with the library of theoretical evolutionary tracks and synthetic spectra, which are pre-processed to obtain the tables of isochrones and bolometric corrections BC_λ, we can derive magnitudes and colors for individual stars. For a given star (T_{eff}, L) along an isochrone, the bolometric magnitude is defined as $M_{bol} = -2.5\ log(L/L_\odot) + M_{bol,\odot}$,

and the absolute magnitude can be computed according to $M_\lambda = M_{bol} - BC_\lambda$ (see Girardi et al. (2002) for details). On the other hand, the solar position is also given out, which helps to determine the distance of the simulated stars, r. The sun is assumed to be 8.7 kpc away from the Galactic centre, and 24.2 pc above the Galactic plane. Therefore, considering the suitable extinction A_λ, the absolute magnitudes can be converted to the apparent magnitudes, according to $m_\lambda = M_\lambda + 5\ log\ r + A_\lambda(r) - 5$.

3.2 Our code

Since the new massive star tracks have not yet been implemented in TRILEGAL, we built our own CMD simulator. We modified the code that computes the *PARSEC* isochrones, allowing for the possibility to select a distribution of stars with suitable star formation history (SFH), initial mass function (IMF) and Age-Metallicity relation (AMR).

There are five input quantities in our code:

- Star formation rate (SFR)

  The star formation rate, $\psi(t)$, refers to the total mass of stars formed per unit time, expressed in units of $M_\odot/yr$. The evolution of the SFR with time is defined as the star formation history (SFH). In our code, the SFR is specified as a simple function of time, which is an analytic approximation to the Schmidt's law (Schmidt 1959),

  $$\psi(t) \propto exp(t/\tau). \tag{3.10}$$

  where τ is the characteristic e-folding time (the SFR increases toward recent time when $\tau < 0$) and t represents the age of the star, adopted from 1 Myr to 1 Gyr. The normalization will be discussed in Section 4.3.1

- Initial mass function (IMF)

  The initial mass function, $\xi(logm)$, is defined as the number of stars per unit volume per unit logarithmic mass at the time when they form in the parent molecular cloud (Salpeter 1955),

  $$dn = \xi(logm)d(logm). \tag{3.11}$$

  Several analytic forms are usually used to fit the IMF:

  1. A simple power law :

  $$\xi(logm) = \frac{dn}{d(logm)} \propto m^{-\Gamma}, \tag{3.12}$$

  then it becomes

  $$\xi(m) = \frac{dn}{dm} = Am^{-(\Gamma+1)} = Am^{-\alpha}, \qquad \alpha = \Gamma + 1, \tag{3.13}$$

  where $n(m, m + dm) = \xi(m)dm$, and $\xi(m)$ is the number of stars born with mass between m and $m + dm$.

2. Multi-part power law:

$$\xi(m) = A \begin{cases} m^{-\alpha_0}, & m_0 \leq m \leq m_1, n = 0 \\ m^{-\alpha_1}, & m_1 < m \leq m_2, n = 1 \\ \cdots & \\ m^{-\alpha_n}, & m_n < m \leq m_{n+1}, n \geq 2 \end{cases} \tag{3.14}$$

3. A log-normal form:

$$\xi(logm) = \frac{dn}{d(logm)} = Aexp[-\frac{(logm - logm_0)^2}{2\sigma^2}]. \tag{3.15}$$

4. An exponential form:

$$\xi(m) = \frac{dn}{dm} = Am^{-\alpha}exp[-(\frac{m_0}{m})^{\beta}]. \tag{3.16}$$

We list the commonly used IMF in the following:

- Salpeter (1955) used a simple power law in Formula 3.13 to describe the IMF in the solar neighbourhood, and first derived $\alpha = 2.35$ (or $\Gamma = 1.35$) for $0.4M_\odot < M < 10M_\odot$. This IMF shows a rapid increase toward low-mass stars.
- Miller & Scalo (1979) measured the main sequence stars in the solar neighbourhood, and used three forms to fit the IMF:

  A quadratic fit:

  $$log\xi(logm) = A_0 + A_1 logm + A_2(logm)^2. \tag{3.17}$$

  A log-normal fit, as shown in Formula 3.15. The parameters are $logm_0 = -1.02$ and $\sigma = 0.68$.

  A three-segment power law, as shown in Formula 3.14. The parameters are $\Gamma = 0.4$ for $0.1M_\odot \leq M \leq 1M_\odot$, $\Gamma = 1.5$ for $1M_\odot \leq M \leq 10M_\odot$, and $\Gamma = 2.3$ for $M \geq 10M_\odot$.

  Other coefficients for different analytic forms can be found in Table 7 in Miller & Scalo (1979).
- Scalo (1986) suggested $\alpha \approx 2.7$ for massive stars.
- Kroupa (2001) proposed a three-part power law in Formula 3.14 as the universal IMF with lower and upper mass limits $m_l = 0.01M_\odot$and $m_u = 50M_\odot$, respectively. The parameters are $\alpha = 0.3$ for $0.01M_\odot \leq M < 0.08M_\odot$, $\alpha = 1.3$ for $0.08M_\odot \leq M < 0.5M_\odot$, and $\alpha = 2.3$ for $M \geq 0.5M_\odot$
- Chabrier (2001) used the three functional forms 3.14-3.16 to fit the IMF.

  For multi power-law fit, $\alpha = 1.55$ for $M \leq 1M_\odot$, and $\alpha = 2.7$ for $M > 1M_\odot$.

  For log-normal fit, $logm_0 = -1$ and $\sigma = 0.627$.

  For exponential fit, $\alpha = 3.3$ and $\beta = 0.25$.

  Other coefficients for different analytic forms can be found in Table 1 in Chabrier (2001).

In our code, the mass distribution is provided by the IMF and we assume a simple two power laws representation, a Kennicutt IMF (Kennicutt 1998), in the form of

$$\xi(m) = Am^{-\alpha}, \tag{3.18}$$

where $\alpha = 0.4$ for $m < 1M_{\odot}$, while the exponent is parametrized for $m > 1M_{\odot}$.

The total mass is normalized to 1, i.e.

$$\int_{0.1}^{120} m\xi(m)dm = 1M_{\odot}, \tag{3.19}$$

so that we can express SFR in units of $M_{\odot}$/yr. In order to avoid too many faint stars, we just select stars between $1.9M_{\odot}$and $120M_{\odot}$to creat the catalogue.

- Age-Metallicity relation (AMR)

  The age-metallicity relation characterizes the general trend of the variation of the metallicity with age for stars. It is a record of progressive enrichment of the galactic metal content with time, and thus provides clues on the star formation and chemical evolution of the galaxy. This relation was first established by Twarog (1980) who analysed photometric metallicities and isochrone ages of field disk stars in the solar neighbourhood and found a trend of decreasing metallicity with increasing stellar age.

  Since our analysis is limited to the youngest and brightest stars, we deem they have the same chemical composition. We therefore do not take into account an age-metallicity relation but instead we fix the abundance to the most likely value of the burst, taken from the literatures as discussed in Section 4.1.2 and 5.1.2.

- The library of *PARSEC* isochrones

  Isochrones are curves used to describe the evolutionary positions of stars with the same age but various masses on the Hertzsprung-Russell diagram (HRD). It originates from the Greek word meaning "same age". This concept is contrast to the evolutionary track, which is a plot of stars with the same mass but various ages across the HRD. The evolutionary tracks can be processed to the isochrones by connecting the equal-age points along the tracks of different initial masses.

  In our code, we compute the isochrones using *PARSEC* evolutionary tracks, giving the luminosity L, the effective temperature T_{eff}, the surface gravity g and other physical properties of stars as a function of stellar age t, initial mass M_{ini}, and metallicity Z.

- The library of bolometric corrections

  The bolometric correction, BC, is used to convert the absolute magnitude at a given band to the absolute bolometric magnitude. "Bolometric" means integrated over the entire stellar spectral energy distribution. The mathematical definition is

$$BC_{S_\lambda} \equiv M_{bol} - M_{S_\lambda}. \tag{3.20}$$

  For a star, if the extinction is neglected, the flux f_λ (energy per unit time, unit area and unit wavelength) at a given wavelength λ received on the Earth and the flux F_λ at the stellar surface satisfy the relation

$$f_\lambda = F_\lambda(\frac{R}{d})^2, \tag{3.21}$$

where R is the stellar radius and d is the distance. F_λ can be derived from the model spectrum of the stellar atmosphere which is uniquely determined by the effective temperature T_{eff}, the gravity g and the chemical composition $[M/H]$.

The apparent magnitude m_{S_λ} that covers the wavelength range $[\lambda_1, \lambda_2]$ is given by

$$m_{S_\lambda} = -2.5log\Big(\frac{\int_{\lambda_1}^{\lambda_2} f_\lambda S_\lambda d\lambda}{\int_{\lambda_1}^{\lambda_2} f_\lambda^0 S_\lambda d\lambda}\Big) + m_{S_\lambda}^0, \tag{3.22}$$

where S_λ is the response function of the photometric filter between λ_1 and λ_2. f_λ^0 and $m_{S_\lambda}^0$ represent the flux and apparent magnitude of a reference star, which we call "zero points" of a given photometric system. S_λ varies in different photometric systems. The very popular systems are Johnson-Cousins-Glass UBVRIJHKLMN and HST/WFPC2 VEGAmag systems. Details about photometric systems can be found in Bessell (2005).

The absolute magnitude M_{S_λ} is defined as the magnitude at a distance of d=10pc, so we obtain

$$M_{S_\lambda} = -2.5log\Big[\Big(\frac{R}{10pc}\Big)^2 \frac{\int_{\lambda_1}^{\lambda_2} F_\lambda S_\lambda d\lambda}{\int_{\lambda_1}^{\lambda_2} f_\lambda^0 S_\lambda d\lambda}\Big] + m_{S_\lambda}^0, \tag{3.23}$$

If assume $S_\lambda = 1$ at all wavelength, $\lambda_1 = 0$ and $\lambda_2 = \infty$, and adopting the sun as the reference star, we have the bolometric magnitude

$$M_{bol} = M_{bol,\odot} - 2.5log(L/L_\odot) = M_{bol,\odot} - 2.5log(4\pi R^2 F_{bol}/L_\odot), \tag{3.24}$$

where $M_{bol,\odot}$ is the solar absolute bolometric magnitude and $L_\odot$ is the solar luminosity. Here we adopt $M_{bol,\odot}$=4.77 and $L_\odot$=3.844×10^{33} erg s^{-1} (Bahcall et al. 1995). $F_{bol} = \int_0^\infty F_\lambda d\lambda = \sigma T_{eff}^4$ is the total emerging flux at the stellar surface.

From the definition of the bolometric correction, we have

$$BC_{S_\lambda} = M_{bol,\odot} - 2.5log\Big[4\pi(10pc)^2 F_{bol}/L_\odot\Big] + 2.5log\Big(\frac{\int_{\lambda_1}^{\lambda_2} F_\lambda S_\lambda d\lambda}{\int_{\lambda_1}^{\lambda_2} f_\lambda^0 S_\lambda d\lambda}\Big) - m_{S_\lambda}^0, \tag{3.25}$$

which depends only on the spectral shape (F_λ/F_{bol}) and basic astrophysics constants.

We adopt the bolometric correction tables from Marigo et al. (2008). These tables are obtained by convolving large libraries of stellar spectra with the filters transmission curves being considered, as described in Girardi et al. (2002). In the ranges of effective temperature, surface gravity, and metallicity relevant to this work, we use the spectra derived from the ATLAS9 model atmospheres (Castelli & Kurucz 2003), which are well calibrated against observations. In the more advanced phases (Red Supergiants, Wolf Rayet stars) and for the highest masses, where the effects of mass loss may be significant, some discrepancies may somewhat affect the transition to different spectral libraries, but these differences do not alter our results because these stars are only a minority in the analysed CMDs.

The SFH and, to a lesser degree, the shape of the IMF are tuned to reproduce the stellar number counts as described below.

Our code generates stars with randomly given mass and age according to the specified SFR and IMF. When (M, t) of a star is known, the corresponding point on the isochrones computed with *PARSEC* can be determined, and thus the stellar luminosity and effective temperature can be obtained.

From the relations

$$L = 4\pi R^2 F_{bol} = 4\pi R^2 \times \sigma T_{eff}^4, \tag{3.26}$$

and

$$g = G\frac{M}{R^2}, \tag{3.27}$$

the gravity can be derived. With specified (T_{eff}, g, $[M/H]$), the bolometric correction tables can be determined (Marigo et al. 2008). Taking the sun as the reference star, the bolometric magnitude of the star is $M_{bol} = -2.5\ log(L/L_{\odot}) + M_{bol,\odot}$, and the absolute magnitude can be calculated according to $M_{\lambda} = M_{bol} - BC_{\lambda}$. The general scheme of our code is shown in Figure 3.1.

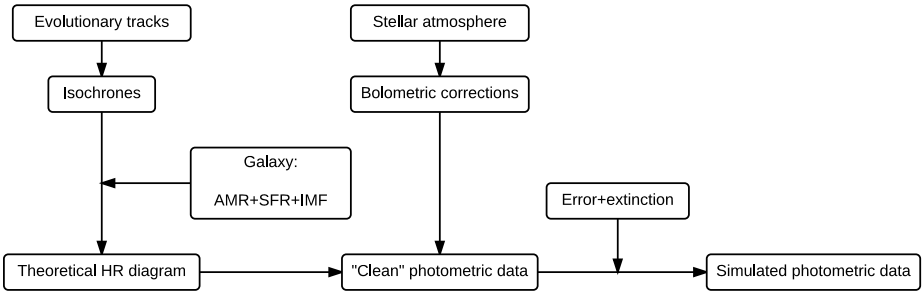

Figure 3.1: The general scheme of our codes.

The outcome of this procedure is a "clean" absolute CMD that must be translated into the observational plane, adopting the proper distance modulus ($m - M = 5 \log d - 5$, where d is the distance in parsecs) and assigning suitable values of error and extinction to each star, as described in Section 4.2 and 5.3 for individual galaxies. With this procedure we generate, for each form of SFH and IMF, simulated catalogues containing many more stars (we fix the number to be 300,000) than the observed CMDs. The "simulated CMDs" are thus drawn from subsets of these large catalogues, and this procedure is repeated a hundred times to obtain, on one hand, the average and variance of the star luminosity function and, on the other hand, the best-fit model to the observed luminosity function, for the selected input parameters.

Chapter 4

PARSEC evolutionary tracks of massive stars at metallicities $0.001 \leq Z \leq 0.004$

4.1 Data

4.1.1 Photometric data

To compare our models with observations, we use photometry from Bianchi et al. (2012b)'s Hubble Space Telescope (HST) treasury survey HST-GO-11079, which imaged star-forming regions in six Local Group dwarf galaxies, Phoenix, Pegasus, Sextans A, Sextans B, WLM and NGC 6822, and in M31 and M33. Multi-band imaging with WFPC2 includes six filters from far-UV to near-IR, F170W, F255W, F336W, F439W, F555W F814W. [1] Bianchi et al. (2012b) survey was focused on the study of the massive stars in these galaxies, therefore the exposures were tuned to provide complete filter coverage with high S/N for the hottest stars, while cooler stars have progressively lower S/N in the UV filters. We refer the reader to Bianchi et al. (2012b) for details on the data reduction and photometric quality; for the purpose of this work it is sufficient to recall that incompleteness reaches 20% at mag=21.0, 22.8, 22.9 and 22.0 in F336W, F439W, F555W, and F814W, respectively.

After careful examination of the CMDs we conclude that the three best galaxies suitable for the analysis of their star formation history to check the performance of the new *PARSEC* V1.1 models of massive stars at low metallicity are WLM, NGC 6822 and Sextans A. The other three galaxies, Phoenix, Pegasus and Sextans B, are less populated of massive stars and therefore less suitable for our purpose. Furthermore, deeper photometry in the F555W and F814W filters is available for Sextans A (Dalcanton et al. 2009), which we use for comparison with simulated CMDs. The CMDs of Sextans A, WLM and NGC 6822 are shown in Figures 4.1-4.3.

[1] http://dolomiti.pha.jhu.edu/LocalGroup/

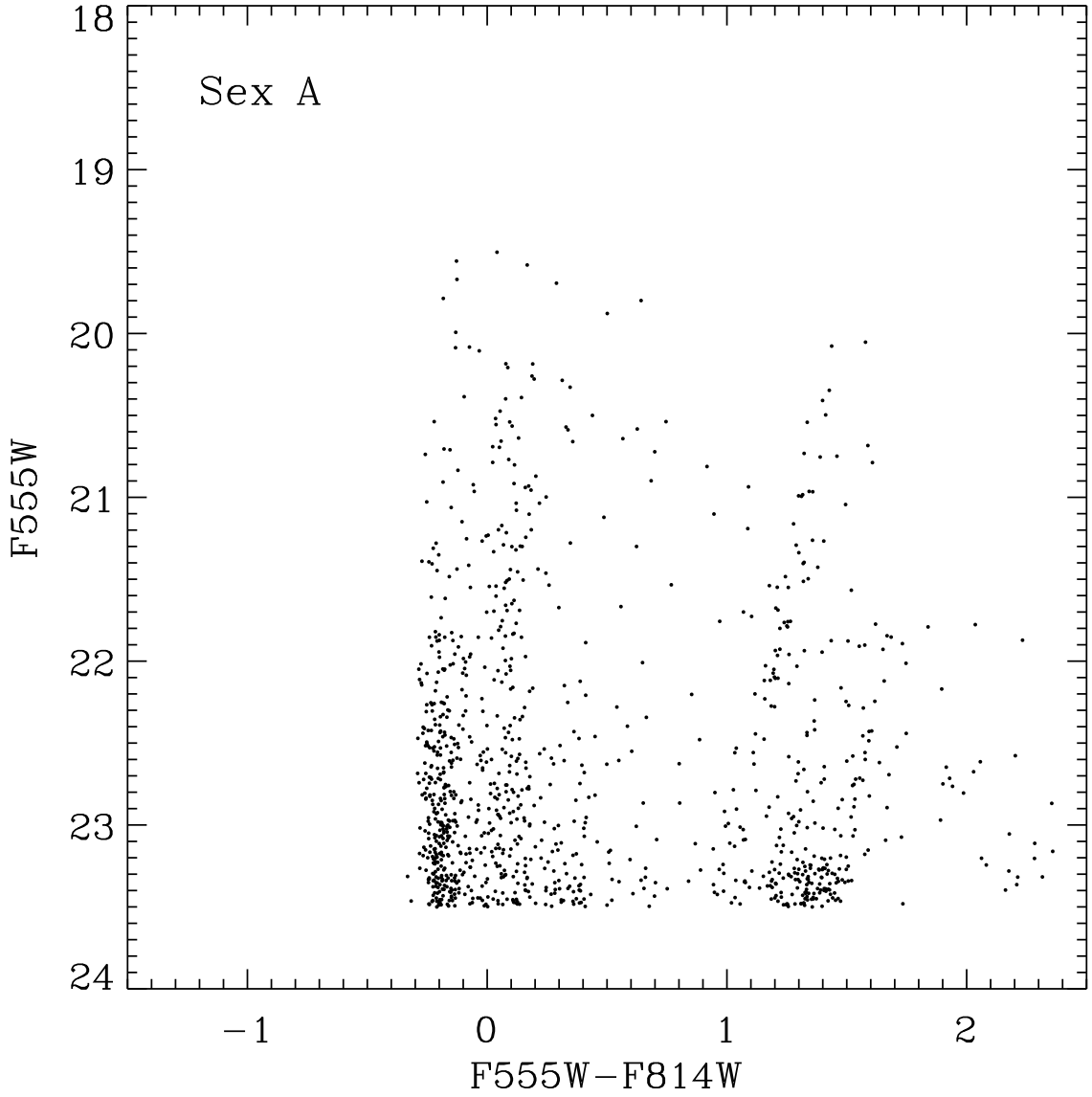

Figure 4.1: color-magnitude diagram of Sextans A.

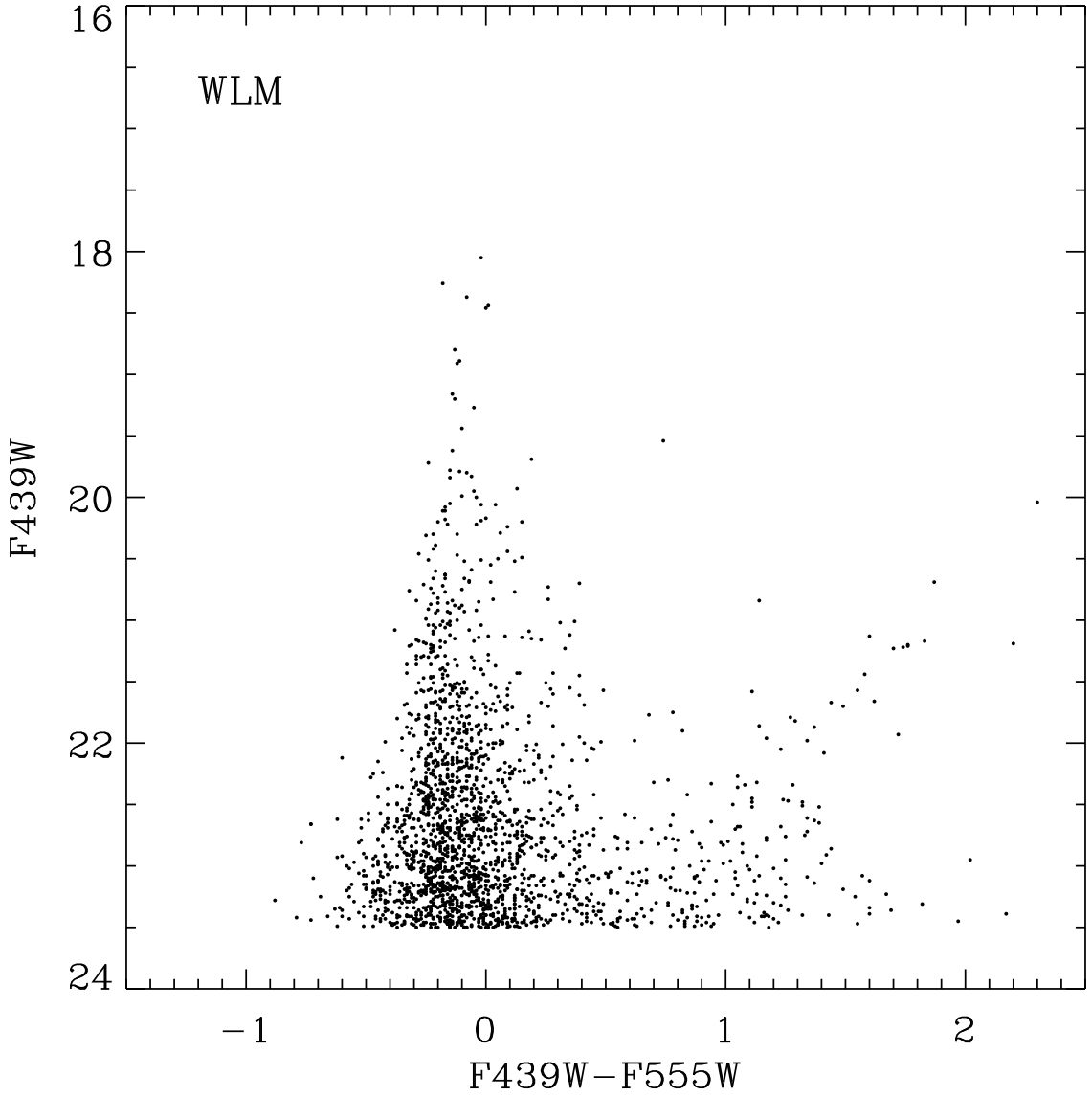

Figure 4.2: Color-magnitude diagram of WLM.

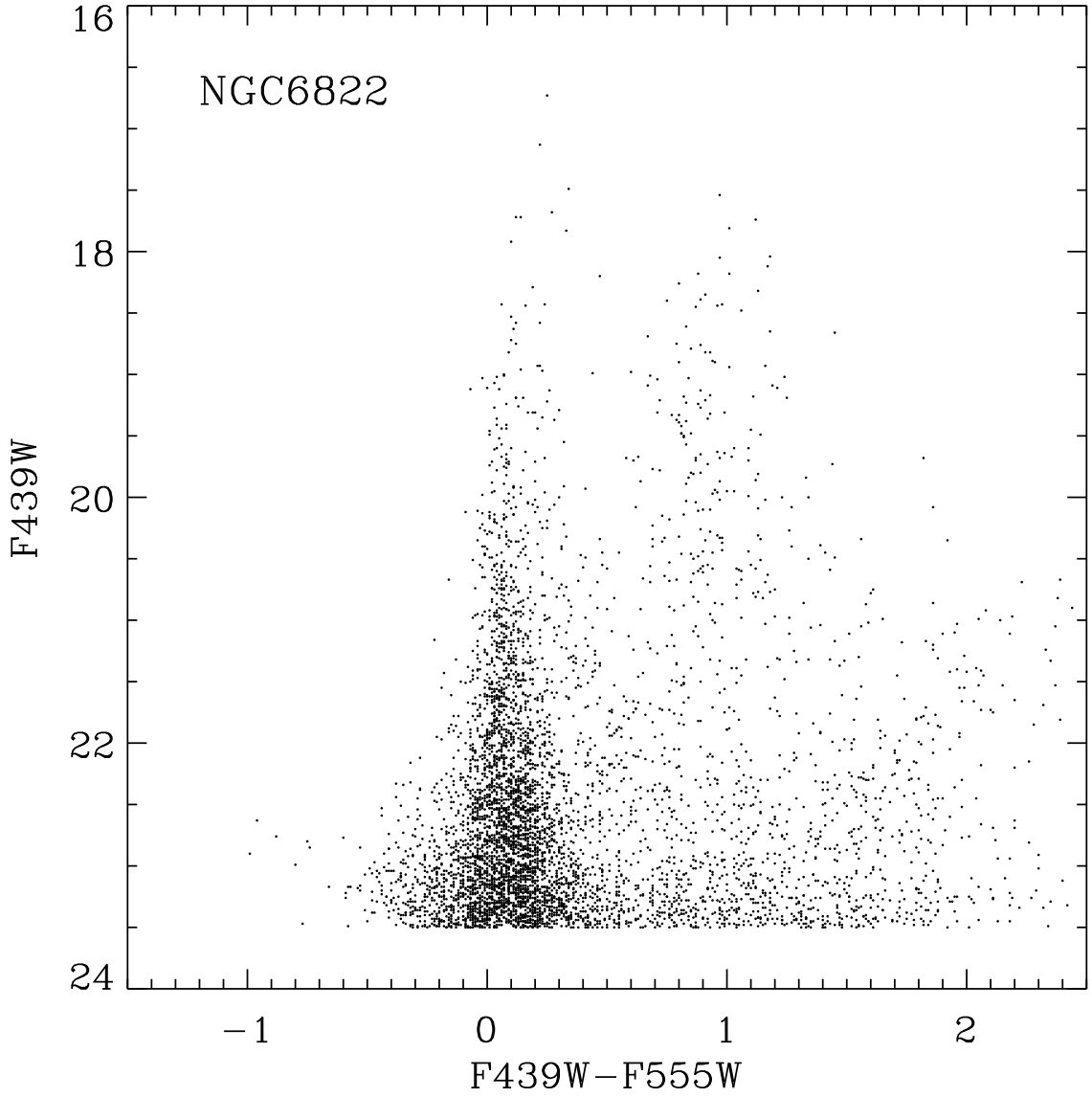

Figure 4.3: Color-magnitude diagram of NGC 6822.

4.1.2 Metallicity of the sample galaxies

To select the appropriate metallicity of the models, we examined the literature for existing measurements of abundances in our sample galaxies.

The Metallicity of Sextans A

An Oxygen nebular abundance of 12 + log(O/H) = 7.49 for Sextans A, was obtained by Skillman et al. (1989a) by means of optical spectrophotometry of H_{II} regions. Comparing synthetic and observed CMDs, Dolphin et al. (2003b) obtained a mean metallicity of [M/H]=-1.45 ± 0.2 throughout the measured history of the galaxy. Analysis of three isolated A-type supergiants by Kaufer et al. (2004) yielded a present-day stellar abundance of the α element Mg as $\langle[\alpha(Mg_I)/H]\rangle = -1.09 \pm 0.02$. Finally, Kniazev et al. (2005) presented spectroscopic observations of three H_{II} regions and a planetary nebula (PN) in Sextans A. They derived an average Oxygen abundance of 12 + log(O/H) = 7.54 ± 0.06 in theH_{II} regions, which agrees well with Kaufer et al. (2004) data. However, the Oxygen abundance of the PN is significantly higher, 12 + log(O/H)=8.02 ± 0.05 and it is explained as self-pollution by the PN progenitor. Adopting the oxygen solar abundance of 12 + log(O/H) = 8.66 based on the 3D model (Asplund et al. 2004) and the corresponding total metallicity (Z ∼0.014), we obtain for the young populations of Sextans A a metallicity of Z ∼0.001. For this galaxy we will use *PARSEC* V1.1 models with Z=0.001.

The Metallicity of WLM

For WLM, Skillman et al. (1989b) and Hodge & Miller (1995) measured Oxygen nebular abundances of 12 + log(O/H) = 7.74 and 7.77, respectively. Venn et al. (2003) found a significant discrepancy between nebular abundance ([O/H] = -0.89) and stellar abundance [O/H] =-0.21 ± 0.10. From a study of nine H_{II} regions, Lee et al. (2005) obtained a mean nebular oxygen abundance of 12 + log(O/H) = 7.83 ±0.06, corresponding to [O/H]=-0.83 when adopting the solar oxygen abundance of 12 + log(O/H) = 8.66 (Asplund et al. 2004). This is in excellent agreement with the measurement of Bresolin et al. (2006) who carried out a quantitive analysis of three early B supergiants and derived an average 12 + log(O/H) = 7.83 ± 0.12. Finally, Urbaneja et al. (2008) obtained a weighted mean metallicity [Z/H] = -0.87 ± 0.06 for several B and A supergiants, a result consistent with the previous measurements. The metallicity of the young populations is thus [O/H]∼-0.9 which corresponds to Z ∼0.0017. Even though this value is larger than that of Sextans A, in the following analysis we will make use of the same models adopted for Sexstans A, so that the models with Z=0.001 are compared with two bracketing samples of observational data.

The Metallicity of NGC 6822

The nebular abundance of NGC 6822 was found to be 12 + log(O/H) = 8.25 ± 0.07 from a spectroscopic analysis of seven H_{II} regions Pagel et al. (1980). This result is supported by Richer & McCall (1995) who observed two planetary nebulae, and deduced oxygen abundances 12 + log(O/H) = 8.10 and 8.01, respectively. From a spectral study of A-type supergiants, Venn et al. (2001) derived an average Oxygen

Table 4.1: Coordinates and Area applied in TRILEGAL

Galaxy	α (h)	δ (deg)	Total Field Area (deg^2)
Sextans A	10.183555556	-4.692777778	0.003222222
WLM	0.032805556	-15.460833333	0.004166667
NGC6822	19.749361111	-14.803333333	0.011111111

abundance of 12 + log(O/H) = 8.36 ± 0.19 and [Fe/H] = -0.49 ± 0.22 for the young star population, suggesting also the presence of a gradient in [O/H]. Tolstoy et al. (2001) measured the Ca_{II} triplet in RGB stars and estimated the mean metallicity of the old stars to be [Fe/H] = -1 ± 0.5, with values of individual stars ranging from -2.0 to -0.5. This average value agrees well with Davidge (2003) who obtained the same value from the slope of the RGB. By means of the ratio between C type and M type Asymptotic Giant Branch stars, Cioni & Habing (2005) derived a spread of the metallicity Δ[Fe/H] = 1.56 dex, and Kang et al. (2006) found Δ[Fe/H] = 0.07 - 0.09 dex in the bar. Moreover, Sibbons et al. (2012) obtained [Fe/H] = -1.29 ± 0.07. The metallicity of NGC 6822 is definitely higher than that of Sexstans A and WLM and therefore we need to use higher metallicity models for the analysis of its CMD. In order to favour models with extended blue loops and thus to avoid any possible problem due to the adoption of a too high metallicity, we will adopt the lowest value compatible with observations of the young populations. Both the lowest values of [O/H] by Pagel et al. (1980) and Venn et al. (2001) are compatible with Z ∼0.0045, again using 12 + log(O/H) = 8.66 and Z=0.014 for the Sun. The simulation of NGC 6822 will thus be performed using models with Z=0.004.

4.1.3 Contamination by foreground stars

Since foreground Galactic stars can contaminate the observed diagrams, it is necessary to check this effect before analyzing their CMDs. The contamination analysis can be done using the TRILEGAL code that reproduce the Galactic stellar distribution towards particular locations in the sky, as seen by the Sun.

TRILEGAL has been thoroughly described in Section 3.1. Additional parameters as the parameters specifying the simulated area, the limiting magnitude in any of the available filters, the resolution in magnitude, Δm, have also been set. The coordinates and area adopted to generate the simulated MW stars in the directions of the three galaxies, are listed in Table 4.1. The limiting magnitude is set to reproduce the contamination above a given apparent magnitude which is roughly 25 mag in F439W. The resolution $\Delta m = 0.1$ is adopted, which means only luminosity function structure larger than this can be detected.

We run the TRILEGAL code via its web-based interface http://stev.oapd.inaf.it/cgi-bin/trilegal.

The simulations indicate that only in the case of NGC 6822 there is a significant contamination, as expected because of its low Galactic latitude.

Figure 4.4 shows the simulated MW foreground stars on the CMD of NGC 6822. The contamination has the shape of a plume around $m_{F439W} - m_{F555W} \sim 1$ that occupies the region between the blue and the red sequences of NGC 6822, likely true members of the galaxy. Figure 4.5 shows the mass function and the metallicity distribution of the simulated MW stars. We find that over 95% stars are smaller than $1M_{\odot}$. Meanwhile, 73% stars have the metallicity larger than one-tenth of solar metallcity, while only 6%

stars exceed solar metallicity.

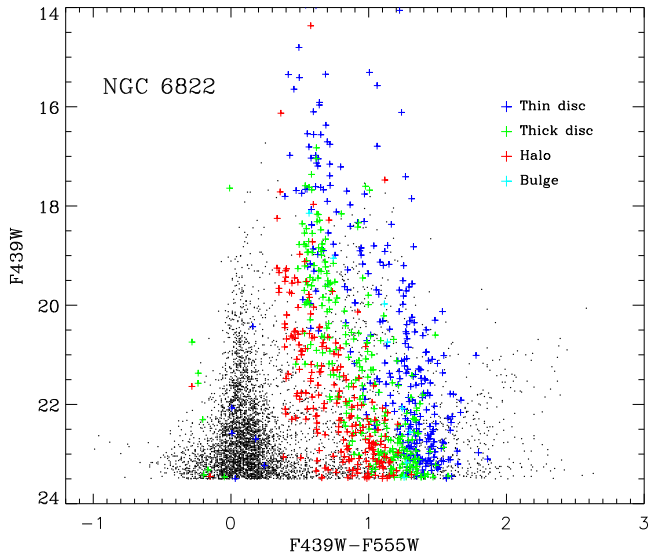

Figure 4.4: Estimated MW contamination on the CMD of NGC 6822. Black dots are the observed stars, while colored dots are the predicted contamination from the four Galactic components as indicated in the color code labels.

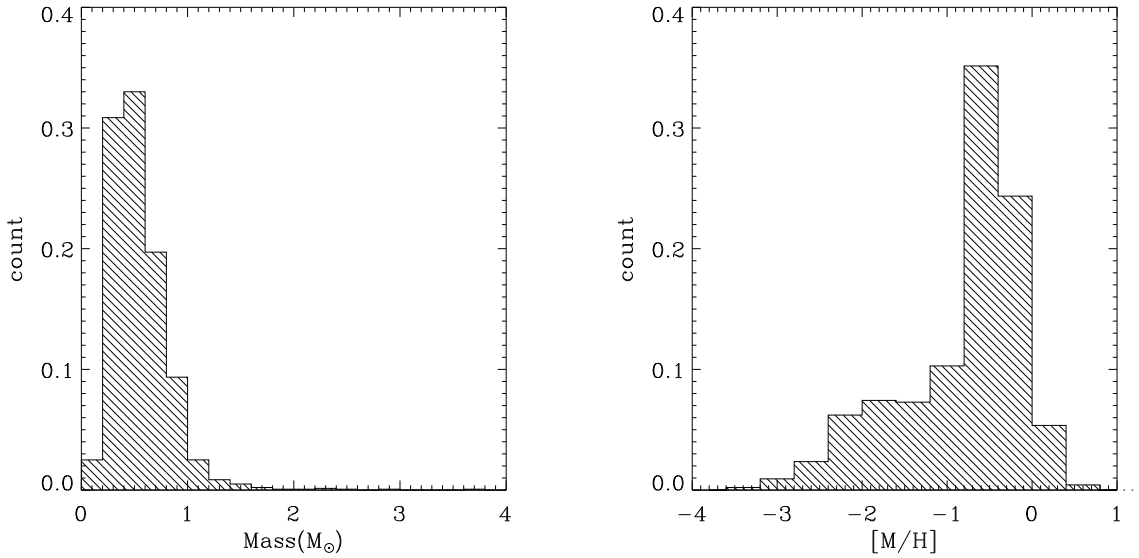

Figure 4.5: Mass (left) and metallicity (right) distribution of the simulated stars. The counts are scaled with respect to the total number.

In order to quantify the contamination, we counted the simulated stars that fall within the box $0.5 < m_{F439W} - m_{F555W} < 1.4$ and $18 < m_{F439W} < 22.5$, in the CMD. In this region we count 336 stars in the observed CMD while the simulation predicts 93 stars of the thin disc (blue crosses), 118 of the thick disc(green crosses), 59 of the halo (red crosses), and 4 of bulge stars (cyan crosses). Table 4.2 lists the nature of the contaminating stars. These stars are found to be low-mass stars. Thin disc stars range from 1 Gyr to 8 Gyr, whereas stars of other components were formed around 10 Gyr. They are inferred to be dwarfs on the main sequence (MS), for the central H-burning phase for low-mass stars is quite

long, being of the order of ∼ 10 Gyr for $1M_{\odot}$star, and this MS lifetime increases as the mass decreases. Additionally, the metallicity of halo stars is very low, with 25% stars less than one-hundredth and 88% less than one-tenth of solar metallicity. Bulge stars have higher metallicity than solar metallicity, and disc stars are in between. In total we find that there could be 178 possible MW stars in the selected box, indicating that, in NGC 6822, the MW contamination above $m_{F439W} - m_{F555W}$ >0.5 is severe and must be taken into account in the comparison of the simulated and observed CMDs (Section 4.3 and 4.4 below).

Table 4.2: The Nature of the Simulated MW stars in NGC 6822

Galaxy Components	Age (Gyr)	Initial Mass ($M\odot$)	Z
Thin disc	1 - 8	0.46 - 1.05	0.004 - 0.03
Thick disc	10.7 - 11.7	0.47 - 1.23	0.002 - 0.0085
Halo	11.7 - 12.9	0.41 - 1.01	0.000028 - 0.013
Bulge	8	0.71 - 0.95	0.02 - 0.062

The estimated contamination for Sextans A and WLM is shown in Figure 4.6. When we just consider stars brighter than m_{F555W}=23.5 in Sextans A, the observed stars are 1081, while the simulated MW stars are 25. The contamination in WLM is even less, 19 simulated foreground stars out of 2038 observed stars when counting stars brighter than m_{F439W}=23.5. Therefore, the contamination for these two galaxies is negligible.

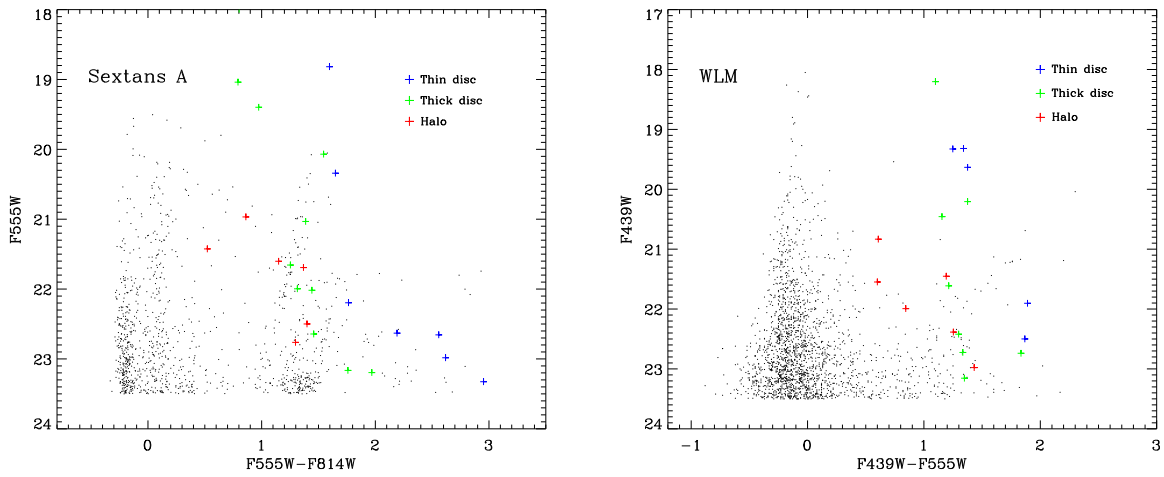

Figure 4.6: Estimated MW contamination on the CMDs of Sextans A (left) and WLM (right).

4.2 Synthetic color-magnitude diagrams

First of all, we use the code described in Section 3.2 to generate a mock stellar catalogue. In order to avoid unnecessary large numbers of simulated stars we define a suitable absolute limiting magnitude by taking into account the distance modulus of the galaxies and the faintest magnitude at which the incompleteness reaches the 20% in each filter, which is ≈23mag in F439W and F555W (Bianchi et al. 2012b). For the simulatons of WLM and NGC 6822 we thus select a limiting apparent magnitude of

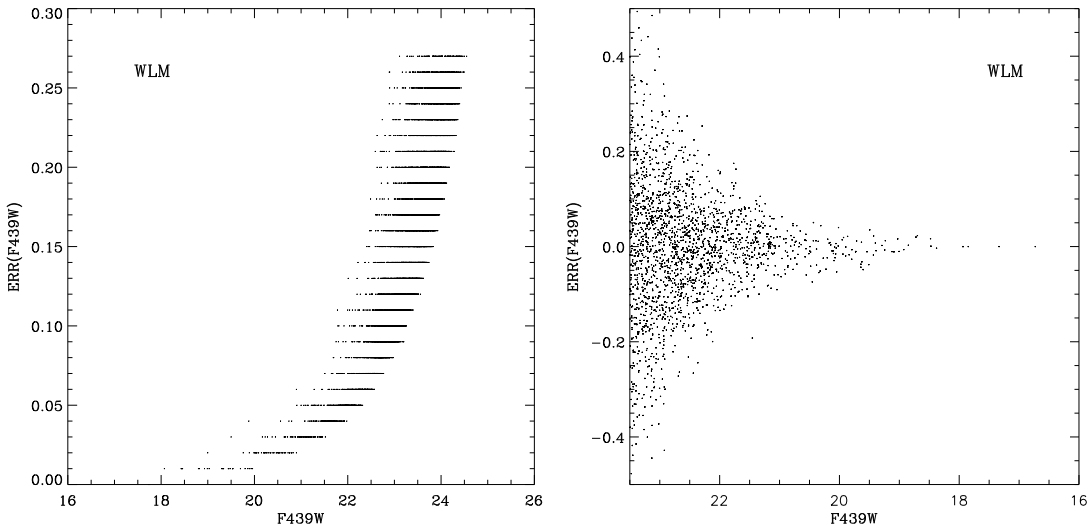

Figure 4.7: Left panel: error-magnitude plot for WLM in the F439W filter. Right panel: simulated error *vs* apparent magnitude in the F439W filter for WLM stars.

m_{F439W}=23.5. We adopt the same magnitude limit, m_{F555W}=23.5, also for Sextans A, in order to avoid the inclusion of less massive stars in the simulation, even if the same incompleteness level is reached at fainter magnitudes in the Dalcanton et al. (2009) data.

Then we assign each modelled star the proper error and extinction as depicted below.

4.2.1 Simulated errors

The simulated photometric errors have been derived from the distribution of the observational errors as a function of the apparent magnitude (Bianchi et al. 2012b; Dalcanton et al. 2009), as follows. For WLM and NGC 6822 we select sources with HSTphot *type* = 1 and | *sharpness* |< 0.3 and we plot error *vs* apparent magnitude diagrams. One example for WLM in the F439W filter is shown in the left panel of Figure 4.7. As the error is accurate to two decimal places, this plot looks a bit different from Figure 2 in Bianchi et al. (2012b). To estimate individual errors for the simulated stars in a given filter, we re-bin the error distribution in 0.1 magnitude bins and, within each magnitude bin, we evaluate the median error. Then, the error assigned to each model star of a given apparent magnitude is randomly drawn from a Gaussian distribution with a standard deviation derived from the median value corresponding to its magnitude, as shown in the right panel of Figure 4.7. For Sextant A the errors are determined in the same way, but using the data from Dalcanton et al. (2009). The simulated errors for NGC 6822 and Sextans A are shown in Figure 4.8. We find that the errors for Sextans A stars are very small due to the deep observations.

4.2.2 Accounting for extinction

In the analysis of the CMDs of stellar systems the extinction is generally treated as a constant free parameter that must be derived from a fitting procedure. In this respect, a key feature of this investigation is that we may exploit the information carried by the multi-band photometric coverage of the observations

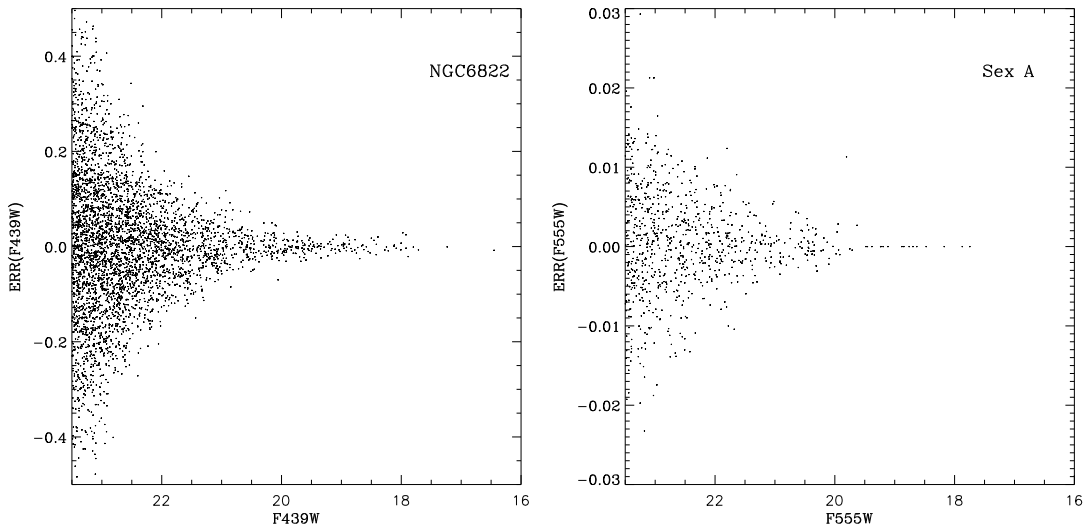

Figure 4.8: Simulated photometric errors as a function of the apparent magnitude in the F439W filter for NGC 6822 (left) and in the F555W filter for Sextans A (right).

because our galaxies were observed in six HST bands by Bianchi et al. (2012b). For many of the observed stars the photometry spectral energy distributions (SED) can be modelled to obtain extinction, effective temperature and bolometric luminosity at once, as shown in Figure 4.9. We use such results to define the attenuation on a star by star basis, in a statistical way.

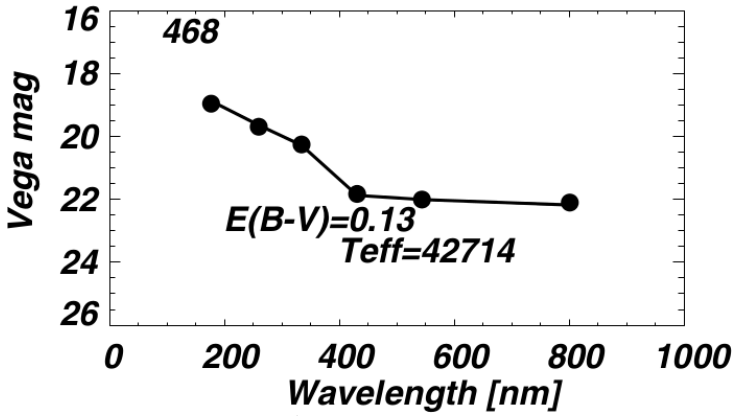

Figure 4.9: The SED of one sample star in Sextans A. The line connecting the multi magnitudes shows the best-fit model SED. This figure is from Bianchi et al. (2012b).

We use extinction results from Bianchi et al. (2012b)'s SED fitting of the multi-band HST photometry with theoretical spectral libraries of different metallicities, Z=0.0002, Z=0.002 and Z=0.02 and different extinction curves, "average" MW with $R_v = 3.1$ (Cardelli et al. 1989b), "LMC2" (Misselt et al. 1999) or "SMC" (Gordon & Clayton 1998). We restricted this analysis to sources with photometric accuracy better than 0.25, 0.20, 0.25, 0.10, 0.10, in the filters F170W, F225W, F336W, F439W, F555W respectively, and applied no error cut in F814W. Such sample restriction to stars detected in at least five filters, with small photometric errors in the optical bands, ensures that enough measurements are available for each star for deriving concurrently two free parameters (T_{eff} and E(B-V)), and biases the analysis sample towards the hottest, most luminous stars, because we require detection even in the far-UV filter. Results

from this survey and similar ones showed that the hottest stars are usually found in regions of high IS extinction (see e.g. Figure 12 of Bianchi et al. (2012b)), as we shall discuss again later. The resulting extinction depends significantly on the adopted attenuation curve (see also Bianchi et al. (2012b)) but much less on the adopted metallicity of the theoretical spectra.

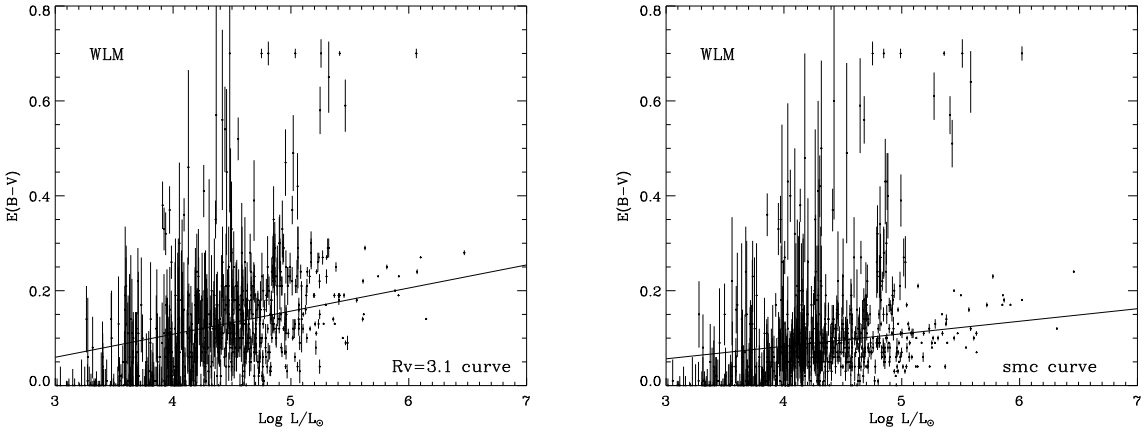

Figure 4.10: Reddening of WLM stars, derived from multi-band SED fitting using the Galactic (left panel) or the SMC (right panel) extinction curves.

As an example, we show in Figure 4.10 the extinction derived for the stars in WLM by Bianchi et al. (2012b). The two panels show two different cases obtained with the same spectral library, Z=0.002, and two different extinction laws, the Galactic (R_v=3.1) one in the left panel and the SMC one in the right panel, respectively. For each star, the E(B-V) is plotted against the stellar bolometric luminosity, which is also derived from the best fit of the observed SED, assuming the distance of the galaxy. The vertical error bars depict the uncertainties, derived in the SED-fitting process. In addition to the formal uncertainties, there may be a slight bias due to poor calibration of the WFPC2 UV filters (CTE corrections) as discussed by Bianchi et al. (2012a). Figure 4.10 shows a trend of increasing E(B-V) at increasing luminosity. The line shown in the figure is a simple best fit to the data obtained after selecting only those with a relative error $\leq$0.2 and excluding the outliers (using LADFIT IDL procedure). The lines shown in the panels show a clear positive slope with the stellar intrinsic luminosity. The slope obtained with the Galactic extinction law (left panel) is about 50% larger than that obtained with the SMC extinction law (right panel). We also observe a significant dispersion at all luminosities and, in general, the more luminous stars have smaller uncertainties. Of course the derived extinction includes the contribution arising from the MW which should be almost constant in a given field though we notice that, at the lower luminosities, there are values that are even less than the contribution of the Galaxy. However, within the uncertainties, they are compatible with the foreground value, which is significant only for NGC 6822. Instead we suppose that the dependence of the additional attenuation with the intrinsic luminosity is a clear signature the internal extinction being age-selective (Silva et al. 1998). In this case the trend arises because younger stars are embedded in a more opaque interstellar medium, independently from their mass and luminosity while, older stars, which are generally less massive and of lower luminosity may be less attenuated. Another noticeable feature is that in the higher luminosity bins the errors are small and the observed values indicate that there can be significant star to star variation in the extinction. There are also a few stars

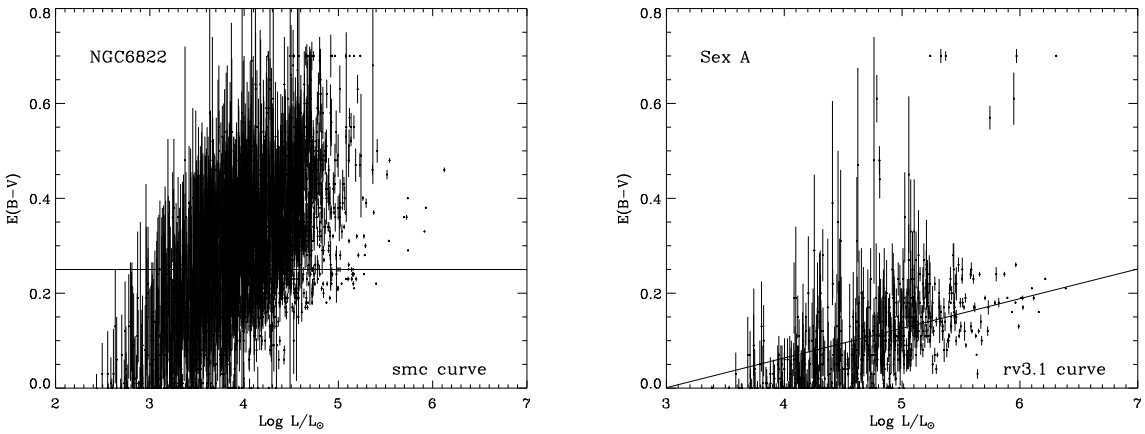

Figure 4.11: Left panel: reddening of NGC 6822 stars, derived from multi-band SED fitting using the SMC extinction curve. Right panel: reddening of Sextans A stars, derived from multi-band SED fitting using the R_v=3.1 extinction curve.

with small error bars and significantly higher than average extinction. These are generally stars cooler than the main sequence ones and a likely explanation for their large extinction is that they could be affected by dust produced by their own circumstellar envelopes. Since there are only a small number of such stars, they are excluded from the fits shown in the above panels, but this point could deserve further investigation because it could be an evidence of pristine dust production in low metallicity galaxies. In summary, there is evidence that in our galaxies the extinction may grow with intrinsic luminosity for the hot stars, and may have a significant star to star variation. In order to account for these effects in the simulated CMD, we randomly distribute the extinction values as a function of the (known) intrinsic luminosity of our model stars, by reproducing the best fit relation and the observed dispersion with a Gaussian model. This effect introduces a further dispersion in the simulated CMDs, that adds to that of the photometric errors and possibly a tilt in the modelled stellar sequences. Because we modeled the extinction distribution on a sample of hot stars, which are mostly associated with regions of high extinction, we should keep in mind in the following discussion that, if cooler stars outside the star-forming regions are included in the catalog, the model extinction distribution may be over-estimated for them; this is not the case for the Bianchi et al. (2012b) survey which mostly targeted conspicuous star-forming regions.

For Sextans A we fit the star to star attenuation model derived from the multi-band data by Bianchi et al. (2012b), and apply it to the F555W, F814W deeper data by Dalcanton et al. (2009), using the selected extinction law. Since in the considered range of magnitudes the errors are negligible in the Dalcanton et al. (2009) photometry, the variable extinction is practically the only source of star to star dispersion in the simulated CMD of Sextans A. The simulated extinction assigned to NGC 6822 and Sextans A stars is shown in Figure 4.11.

4.3 Results with canonical models

As already anticipated in Section 2.2, the simulations of the CMDs of the three galaxies are based on stellar evolution models that use different values of the envelope overshooting. We begin by discussing

the results obtained by using the standard value adopted in *PARSEC* V1.1, i.e. an envelope overshooting of EO=$0.7H_{\rm P}$.

4.3.1 Sextans A

The color-magnitude diagram

The observed CMD of Sextans A, reproduced in the left panel of Figure 4.12, shows the following noticeable features. There is a well defined main sequence with stars brighter than m_{F555W}=23.5 (our selected magnitude limit) and bluer than $m_{F555W} - m_{F814W}$ ≤-0.1. The sequence appears to become broader and redder at brighter magnitudes. This effect is unusual because, in general the sequence becomes bluer and narrower at brighter magnitudes, due to the smaller photometric errors. A parallel sequence, redder by about 0.2-0.3 mag, is also visible and likely corresponds to the stars that are burning helium in the blue loops. This may not be the case for the brightest stars that, as shown in the HR diagrams may ignite central helium before reaching the red supergiant phase. A red sequence, starting at $m_{F555W} - m_{F814W}$ ∼1, indicates the presence of red giant/supergiant stars in the red phase before the loop. Only a scarce number of stars populate the region between the red and blue helium-burning sequences, as expected because of the short crossing timescales of the Hertzsprung gap. The stars found in this gap are likely yellow supergiants, since the MW contamination that mainly affects this region of the CMD is low for this galaxy. The RGB and AGB phases of low and intermediate mass make up the sequences at even redder colors ($m_{F555W} - m_{F814W}$ ≥1.2).

For the simulations of Sextans A we adopt a distance modulus $(\text{m-M})_0 = 25.61$ (Dolphin et al. 2003a). The best simulation obtained with *PARSEC* V1.1 models is shown in the right panel of Figure 4.12. This simulation has been selected from a hundred stochastic realizations made with the same parameters, by means of a merit function based on the differences between the observed and simulated luminosity function, as shown in the left panel of Figure 4.13. Stars of different ages are shown with different colors in the simulated CMD, as indicated in the corresponding labels. The metallicity adopted for the simulation is Z=0.001. The simulated CMD reproduces qualitatively all the main features of the observed diagram, except for the stars redder than $m_{F555W} - m_{F814W}$ ≥1.2 and the sequences that depart from there. This is because we impose a cut in the simulation at masses below $1.9M_{\odot}$, since we are interested in the recent star formation history of the galaxy. For the same reason we discarded from the analysis below all stars in the observed diagram redder than the line $m_{F555W} - m_{F814W} = (31.2 - m_{F555W})/7$ which should correspond to the old population.

The star formation rate

Since our simulated CMD catalogue is constructed by imposing a total number of living stars brighter than a given threshold luminosity, a few steps are needed to derive the normalization of the SFR that corresponds to the parameters given in Table 4.3. In particular we have to take into account that our model catalogue is a super-set of the observed CMD, to which it should be matched. So, we first need to obtain the SFR normalization of the parent catalogue and then scale this normalization to the number of

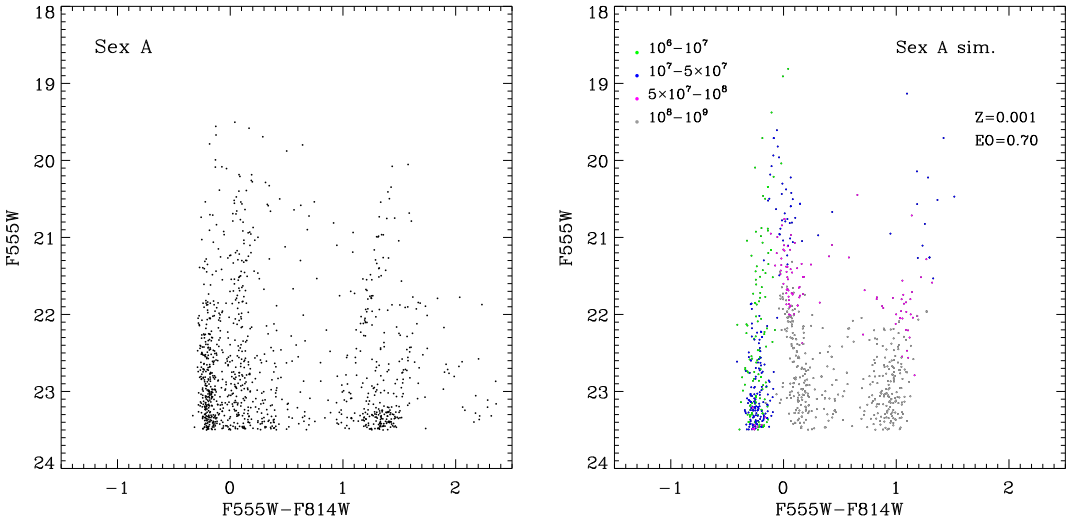

Figure 4.12: Left panel: observed color-magnitude diagram of Sextans A. Right panel: the best model obtained with *PARSEC* V1.1.

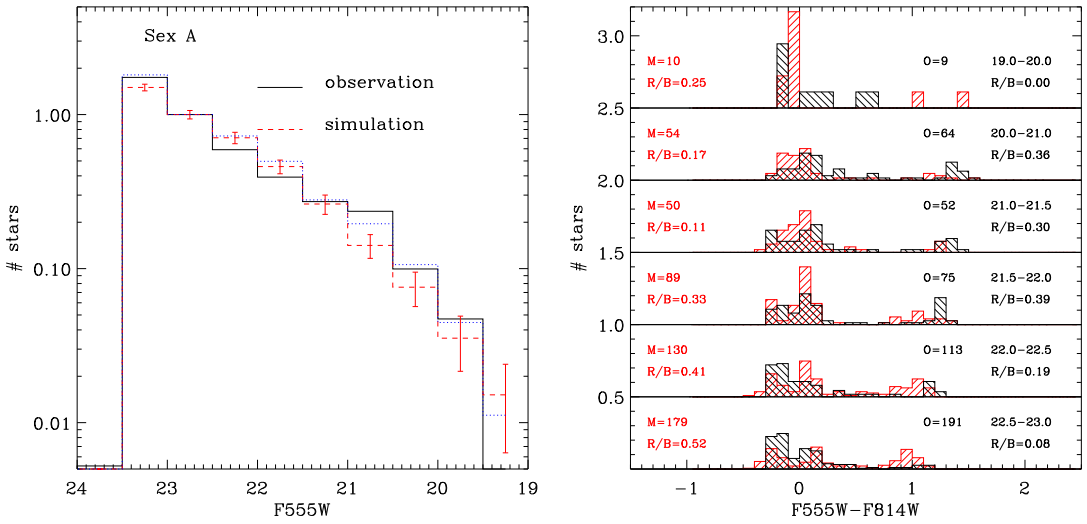

Figure 4.13: Left panel: the observed (black solid) and average simulated (red dashed) luminosity functions (LFs) with vertical standard deviation bars obtained from one hundred simulations with fixed parameters. Blue dotted lines indicate the LFs of the best-fit models. Right panel: comparison of the observed (black) and modelled (red) color distributions.

stars in the observed CMD. For the first step we selected a small mass interval from $1.9 M_{\odot}$to $1.905 M_{\odot}$, for which the stellar evolutionary times are larger than the oldest age of our simulation, i.e. 1 Gyr. Since all such stars are still alive, they must all be in the catalogue and they can be easily counted. On the other hand their number must correspond to the double integral, over the full time interval from 1 Myr to 1 Gyr and the selected mass interval, of the product of the SFR and the IMF, that is

$$N_{[1E6,1E9],[1.9,1.905]} = \int_{1E6}^{1E9} \psi(t)dt \int_{1.9}^{1.905} \xi(m)dm = \int_{1E6}^{1E9} SFR_0 exp(t/\tau)dt \int_{1.9}^{1.905} \xi_m dm \qquad (4.1)$$

where SFR_0 is the current SFR. ξ_m has been derived in Section 3.2. From the comparison between the counted stars and the analytical result of the double integral, we derive the normalization of the model SFR used to generate the large catalogue. To obtain the real SFR from the observed CMD, we simply

Table 4.3: Parameters of the CMD simulations of Sextans A

EO	$T_i[yr]$	$T_f[yr]$	$\tau[yr]$	α	<SFR>[$M_\odot$/yr]
0.7	1E6	1E9	-2E8	2.35	2.5E-3
2	1E6	1E9	-2E8	2.35	2.9E-3
4	1E6	1E9	-1E8	2.35	3.2E-3

scale the model SFR by imposing that the model contains the same number of stars as the observed CMD, in the magnitude range between 23 and 21.5.We use this magnitude interval to limit the stochastic effects introduced by the brightest stars.

Nevertheless, since the normalization is made after the simulated magnitudes have been assigned attenuation and errors, the star formation rate so derived may slightly change between different models, even if the underlying parameters are the same. It is worth noting that the normalization obtained in this way may also be affected by all those effects that may modify the luminosity function in a given pass-band. One such effect, as we will see, is the variation of the lifetime of stars in the blue and red sides of the loops. This effect may change the number of stars in the magnitude bins and so the resulting luminosity function. Another possible effect is that of the unresolved binary stars (even if not physical), which artificially increase the number of stars in the brighter magnitude bins. In this respect, HST/WFPC2's resolution ($0.1''$ spatial scale, i.e. less than half pc in WLM and Sextans A, and about one fourth of a pc projected on the sky, at the distance of NGC 6822) offers a critical advantage with respect to ground-based observations with typical seeing of $\gtrsim 1''$. Quantification of the gain afforded by HST imaging in resolving individual stars in these galaxies can be seen, for example, in Figure 3 of Bianchi et al. (2012b). This is particularly relevant for studies of hot stars, which are found in crowded regions because of their young age, the OB associations having not yet dissolved. The very bright stars are rare, but at B and V magnitudes fainter than ≈20, the effect of unresolved stars in ground-based catalogs, and the gain from HST, become very significant. We finally note that for random superposition (along the line of sight) the combined photometry of two likely different types of stars will result in an SED hard to fit with a single star, and the source may be discarded from the analysis with quality cuts.

We find that the SFR increases toward recent times (τ <0, Table 4.3) with a characteristic time scale $\mid \tau \mid$=2E8yrs. From Figure 4.14, we find the normalization of the real SFR is 3.2E-3$M_\odot$/yr. The average SFR in the last 100 million years is 2.5E-3$M_\odot$/yr, and the effective mass formed in the last 1 billion is 6.3E5$M_\odot$. The maximum mass obtained from the simulation is $M \sim 80 M_\odot$. However, with $m_{F555W} \sim$ 20.5, this is not the brightest star which instead is an evolved star with $M \sim 30 M_\odot$and $m_{F555W} \sim 18.8$.

The color distribution

In order to make the comparison between the observed and simulated CMDs more quantitative, we plot in the right panel of Figure 4.13 the color distribution of the stars in different bins of F555W magnitude, 19-20,20-21,21-21.5,21.5-22,22-22.5,22.5-23. The black histograms refer to the observed CMD while the red histograms are for the simulated CMD. On the right side of each histogram we show the corresponding magnitude interval, the number of stars observed in the interval (O) and the observed ratio (R/B) of stars redder and bluer than a given threshold color. On the left side of the histogram we show the

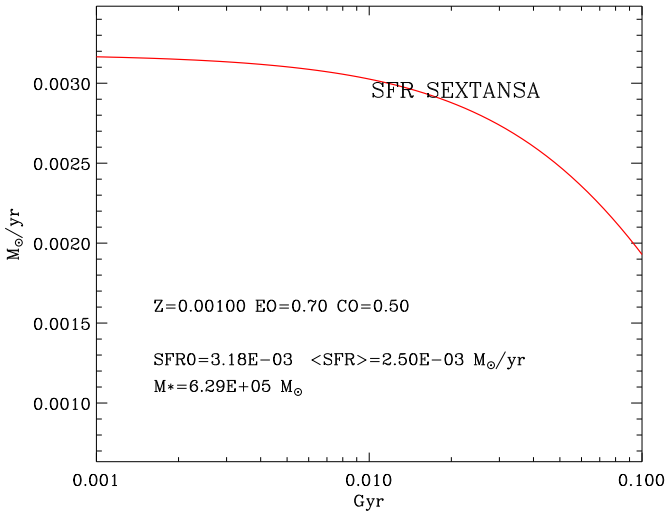

Figure 4.14: The star formation history of Sextans A derived from the best model.

same quantities, number of stars and number ratios (M and R/B), as predicted by the simulations. For Sextans A we adopted a threshold value of $m_{F555W} - m_{F814W}$=0.6 and, as already specified, we did not considered stars redder than the line $m_{F555W} - m_{F814W} = (31.2 - m_{F555W})/7$, that more likely belong to older populations.

The colors and in particular the width of the simulated main sequence match fairly well those of the observed one, in all the magnitude bins. Two points are worth discussing. First we note that, since we are using a single metallicity, the observed width of the main sequence should be ascribed mainly to photometric errors, because the intrinsic width at 22 mag is $\delta(m_{F555W} - m_{F814W})_0 \lesssim$0.07. But the photometric errors of the observations are very small at these magnitudes. Second, the simulated main sequence is almost vertical in the diagram while, as already said we would expect this sequence to be inclined toward bluer colors at brighter magnitudes. Both effects are due to the extinction. The extinction was evaluated for individual stars from simultaneous fits for [T_{eff}, E(B-V)] of multiband photometry (Bianchi et al. 2012b) by means of suitably attenuated spectral models. As discussed in Section 4.2.2, Bianchi et al. (2012b) find that E(B-V), besides showing a significant dispersion, is higher for the hot, young stars. The dispersion in the attenuation is intrinsic and due to region to region variation. Instead its rise with luminosity is likely caused by the following bias. All stars are born in region of relatively higher attenuation and as the time elapses, the parent clouds dissolve and the attenuation decreases (Silva et al. 1998). It is well known that the emission lines (signature of young massive stars) in star-bursts show an attenuation which is about twice that of the optical continuum (mostly from older, lower mass stars) (Calzetti et al. 1994). For a continuous star formation it is thus expected that hot massive stars (that have been recently formed) are the more attenuated, while stars of lower luminosity (whose ages can span the full star-burst period) can have any attenuation. Thus age dependent attenuation provides at once the dispersion and the trend with luminosity that are at the basis of the observed spread and tilt of the main sequence.

The observed blue helium-burning sequence is also fairly well reproduced by the simulation. However

we notice that significant discrepancies remain in the color distribution. In the three most populated bins, at magnitudes fainter than m_{F555W} ∼21.5, the model distribution is clearly bimodal. All the simulated diagrams show a gap between the main sequence and the blue helium-burning sequence that instead is much less evident (if any) in the observed CMD. This gap cannot be filled by invoking errors or by varying the attenuation. The presence of the gap is an indication the models are not able to produce extended loops during the helium burning phase.

The sequence of red stars is also fairly well reproduced. We notice that the slope of this red sequence is fairly well reproduced because of the trend of the attenuation to be larger at larger luminosities, i.e. its slope is partially due to varying reddening across the sample.

As far as the number distribution between red and blue stars (R/B ratio) is concerned, we notice significant discrepancies between the simulated and the observed ratios. Apart from the highest bin where no red stars are observed, the R/B ratio is underestimated by the model below m_{F555W}=22, while it is largely overestimated at fainter magnitudes.

In summary, while the morphology of the simulated CMD is very similar to that of the observed one, inspection of the color distribution shows that there are some important discrepancies, mainly concerning the evolution during the central helium burning phase.

4.3.2 WLM

The CMD of WLM, depicted in the left panel of Figure 4.15, shows a broad main sequence with a quite sharp blue edge and a more smooth decline in the red edge. The red sequence of WLM is poorly defined.

For WLM we adopt a distance modulus $(m\text{-}M)_0 = 24.95$ (Gieren et al. 2008). The best simulation obtained with canonical *PARSEC* V1.1 models is shown in the right panel of the Figure 4.15. In this panel we use different colors for different ages and this helps us to interpret the main features of the CMD. The main sequence of WLM appears to span more than five magnitudes in F439W but actually, at $m_{F439W} \lesssim 21$, it is mainly composed by blue helium-burning stars. This is very clear by looking at stars in different age ranges. In the age interval between 50 Myr and 100 Myr (red dots), the main sequence ends at $m_{F439W} \sim 22.5$ and the blue loop sequence is at least one magnitude brighter. At ages between 10Myr and 50Myr (dark green) the main sequence ends at $m_{F439W} \sim 21$ in the simulations. Brighter stars near the main sequence in this age interval are also burning central helium in the blue loop. The brightest star in the simulation is an evolved star of initial mass M=40$M_\odot$and age=5.3 Myr with luminosity Log(L/L$_\odot$)=5.77 and effective temperature Log(Teff)=4.24. This luminous super-giant star is not in the blue side of the loop as its fainter counterparts because, at such initial masses, helium ignition occurs just after the main sequence. Afterwards the star slowly moves toward the red super-giant phase while burning central helium (see Figure 2.3). Notice that this star is brighter than the brightest star in the observed CMD but this is due to the stochastic nature of the stellar birthrate process at these large masses. Indeed this is not the most massive star in the simulation, which is instead a main sequence star with initial mass M=108$M_\odot$and age=1.77 Myr, about 1.3 mag fainter. In any case, it appears clearly from the simulation that the right side of the "main sequence" is actually made by blue helium-burning stars.

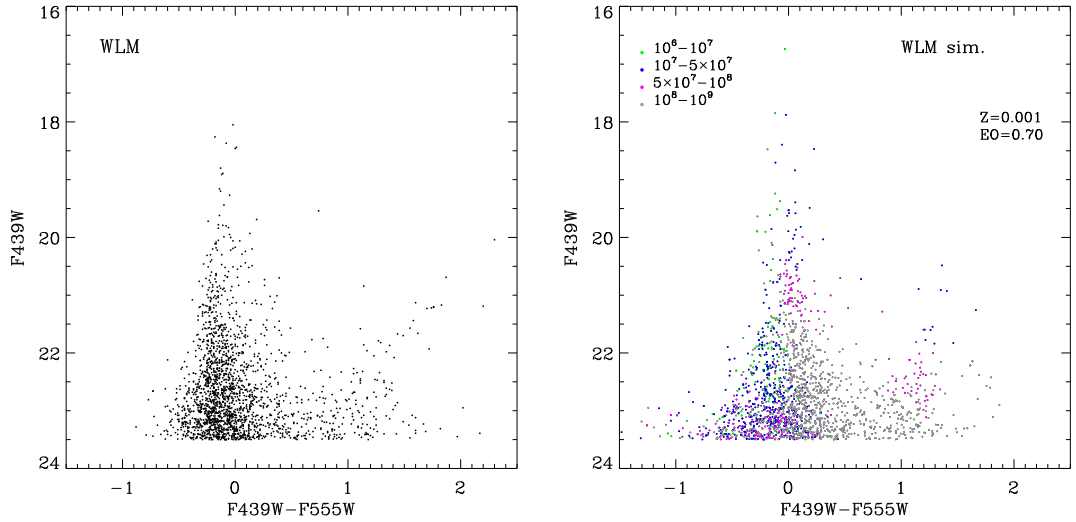

Figure 4.15: Left panel: observed color-magnitude diagram of WLM. Right panel: the best model obtained with *PARSEC* V1.1. Model stars are color-coded by age as indicated in the legend.

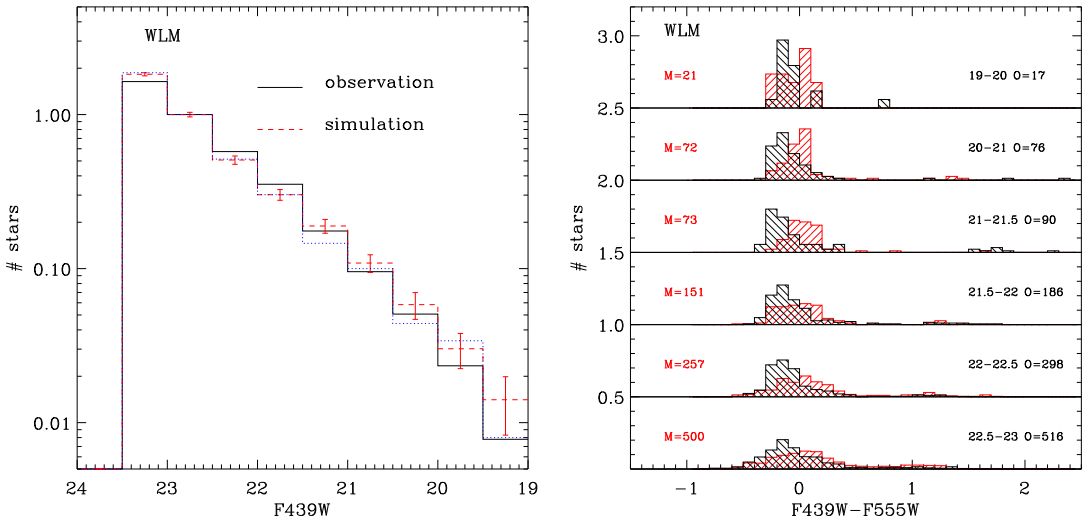

Figure 4.16: Left panel: the observed (black solid) and average simulated (red dashed) luminosity functions (LFs) with vertical standard deviation bars obtained from one hundred simulations with fixed parameters. Blue dotted lines indicate the LFs of the best-fit models. Right panel: comparison of the observed and modelled color distributions.

Also in the case of WLM the global luminosity function of this principal sequence is well reproduced (see the left panel of Figure 4.16) with a SFR that increases toward recent times (see Table 4.4). From Figure 4.17, we see the normalization of the real SFR is 4.1E-3$M_{\odot}$/yr. The average SFR in the last 100Myr is $< SFR >$=3.7E-3$M_{\odot}$/yr, and the effective mass formed in the last 1 billion is 1.8E6$M_{\odot}$.

While the global luminosity function of the observed CMD of WLM is quite well reproduced by the simulation, inspection of the color histograms drawn in the right panel of Figure 4.16 shows that the simulated color distribution across the main sequence does not match the observed one. There appears a clear excess of stars along the red side of the main sequence and a lack of very blue stars which makes the simulated main sequence too broad, especially in the magnitude interval 20≤ m_{F439W} ≤22. Note that the models adopted for WLM have the same metallicity (Z=0.001) as those used for the simulation of Sextans A. In the CMD of Sextans A the main sequence and the blue loop sequence were clearly separated

Table 4.4: Parameters of the CMD simulations of WLM

EO	$T_i[yr]$	$T_f[yr]$	$\tau[yr]$	α	<SFR>[$M_\odot$/yr]
0.7	1E6	1E9	-5E8	2.65	3.7E-3
2	1E6	1E9	-5E8	2.35	2.7E-3
4	1E6	1E9	-2E8	2.35	2.9E-3

while, in the case of WLM, this separation is not so evident because of the larger errors associated with the observations. The apparent excess of red stars is due to the blue helium-burning sequence, therefore we conclude that also in the case of WLM there is a discrepancy concerning these stars.

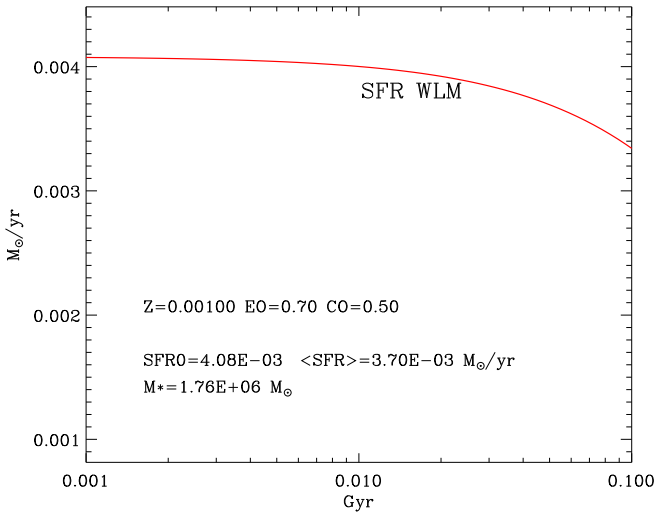

Figure 4.17: The star formation history of WLM derived from the best model.

4.3.3 NGC6822

The observed CMD of NGC6822 is shown in the left panel of Figure 4.18. With a distance modulus $(m\text{-}M)_0 = 23.31$ (Gieren et al. 2006), NGC6822 is the nearest of the three galaxies analysed here and its observed blue sequence spans more than seven magnitudes.

In the CMD we recognize also a yellow sequence, around $m_{F439W} - m_{F555W}$ ~0.8/0.9, and another redder sequence. It is important to clarify the origin of the yellow sequence, because the metallicity of NGC6822, Z ~0.004, is definitely higher than that of the other two galaxies, and this sequence could trace the position of the *blue* loops of relatively metal-rich galaxies. However, our TRILEGAL simulations, and comparison of the CMD among different galaxies, indicate a large contribution from Milky Way foreground stars near the position of the middle sequence. Actually there is some mismatch between the predicted position of the MW stars and the observed CMD. The predicted MW foreground stars not only populate the region of the observed yellow sequence (mainly thin disk stars) but also a region a few tenths of magnitude bluer. Furthermore, significant contamination by thin disk stars extends also brighter than the observed m_{F439W}=18, where only a few stars are seen in the CMD. Thus, due to the significant contamination by Milky Way stars, we exclude the yellow sequence from our analysis. Taking into account that many predicted foreground stars are slightly bluer than the observed yellow sequence, we

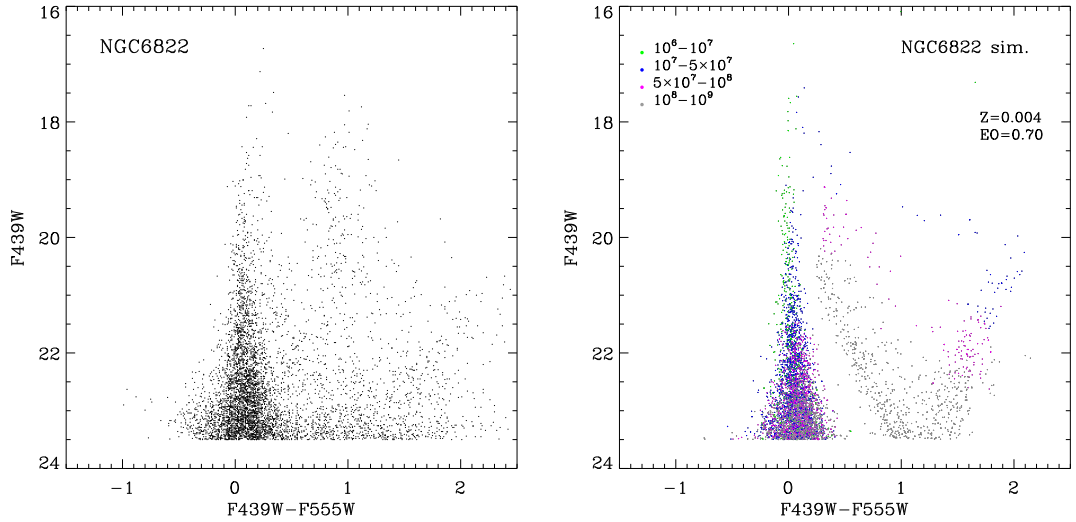

Figure 4.18: Left panel: observed color-magnitude diagram of NGC 6822. Right panel: the best model obtained with *PARSEC* V1.1.

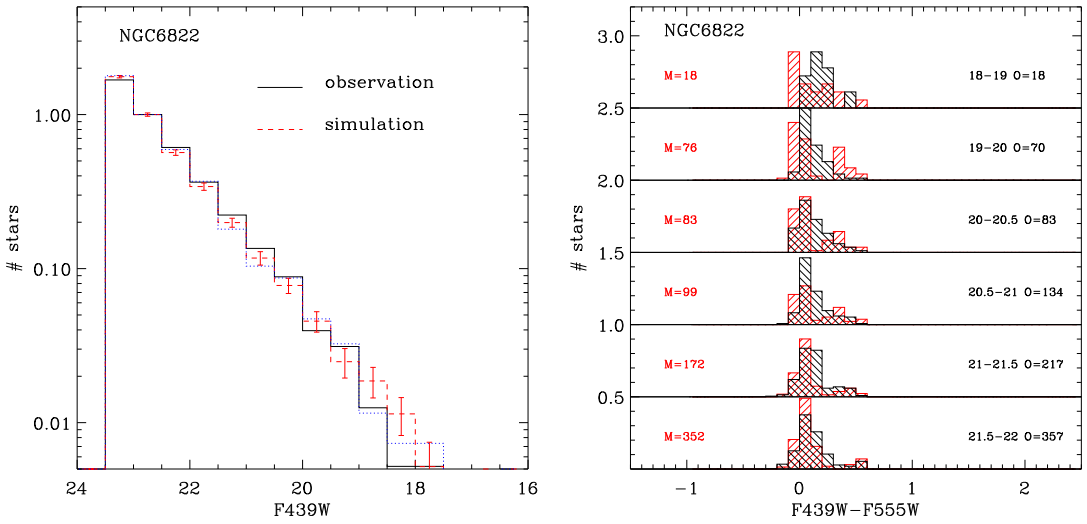

Figure 4.19: Left panel: the observed (black solid) and average simulated (red dashed) luminosity functions (LFs) with vertical standard deviation bars obtained from one hundred simulations with fixed parameters. Blue dotted lines indicate the LFs of the best-fit models. Right panel: comparison of the observed and modelled color distributions.

exclude from further analysis all stars with observed color redder than $m_{F439W} - m_{F555W}$=0.6. Below this threshold the contamination becomes negligible and we may safely use the well populated blue sequence of NGC 6822 to check the models.

The best simulation obtained with canonical *PARSEC* V1.1 models is shown in the right panel of Figure 4.18, based on the well-reproduced luminosity function, as shown in the left panel of Figure 4.19. The parameters of the stellar birthrate for this simulation are shown in Table 4.5. The star formation rate increases toward more recent times with an average value in the last 100 Myr of $< SFR >$=3.5E-3$M_{\odot}$/yr, as indicated in Figure 4.20. The normalization of the real SFR is 4.5E-3$M_{\odot}$/yr, and the effective mass formed in the last 1 billion is 8.9E5$M_{\odot}$. Note that the observed CMD includes seven HST fields, which cover a fraction of the galaxy (∼0.73kpc^2, see Table 1 and Figure 1 of Bianchi et al. (2012b)). Because star formation is very patchy in NGC 6822, and on the other hand the HST pointings used here targeted

star-forming sites, this SFR cannot be simply scaled to the whole galaxy (the two most conspicuous star-forming regions, including Hubble V and Hubble X, and an outer older region, were observed by Bianchi et al. (2001) and Bianchi & Efremova (2006)).

Table 4.5: Parameters of the CMD simulations of NGC6822

EO	$T_i[yr]$	$T_f[yr]$	$\tau[yr]$	α	<SFR>[$M_\odot$/yr]
0.7	1E6	1E9	-2E8	2.35	3.5E-3
2	1E6	1E9	-2E8	2.35	3.7E-3
4	1E6	1E9	-2E8	2.55	4.3E-3

We first notice that, from the *PARSEC* simulation, very few stars are expected to lie in the region occupied by the yellow sequence, corroborating the idea that this sequence is due to strong contamination by MW foreground stars. The maximum mass in the simulation is M=97$M_\odot$at an age of 2.1 Myr, while the brightest star has an initial mass M=72$M_\odot$and an age of 3.6 Myr

The simulation suggests the presence of a sequence of blue helium burning stars running parallel to the main sequence. However in the simulated diagram this sequence appears clearly detached from the main sequence while in the observed CMD it appears a continuation of the main sequence. This appears more clearly in the comparison of the color distributions in the right panel of Figure 4.19. Contrary to the observed distributions, the predicted ones in the range of magnitudes between 19$\leq m_{F439W} \leq$21.5 are bimodal.

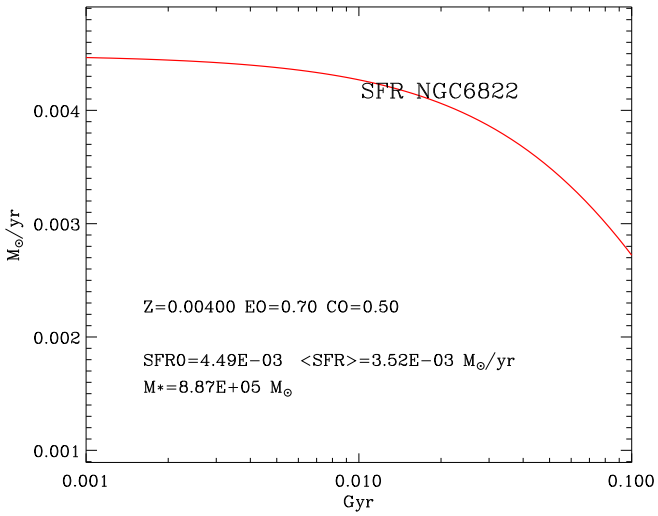

Figure 4.20: The star formation history of NGC 6822 derived from the best model.

4.4 Results with enhanced envelope overshooting models

The above comparisons indicate that the adopted stellar evolutionary models cannot reproduce well the observed CMDs: even accounting for errors and reddening which tend to smear out the color distribution, there remain a visible gap between the main sequence and the blue loop helium-burning sequence. This gap is not observed or much less evident in the data and, at the same time, the color distribution of the

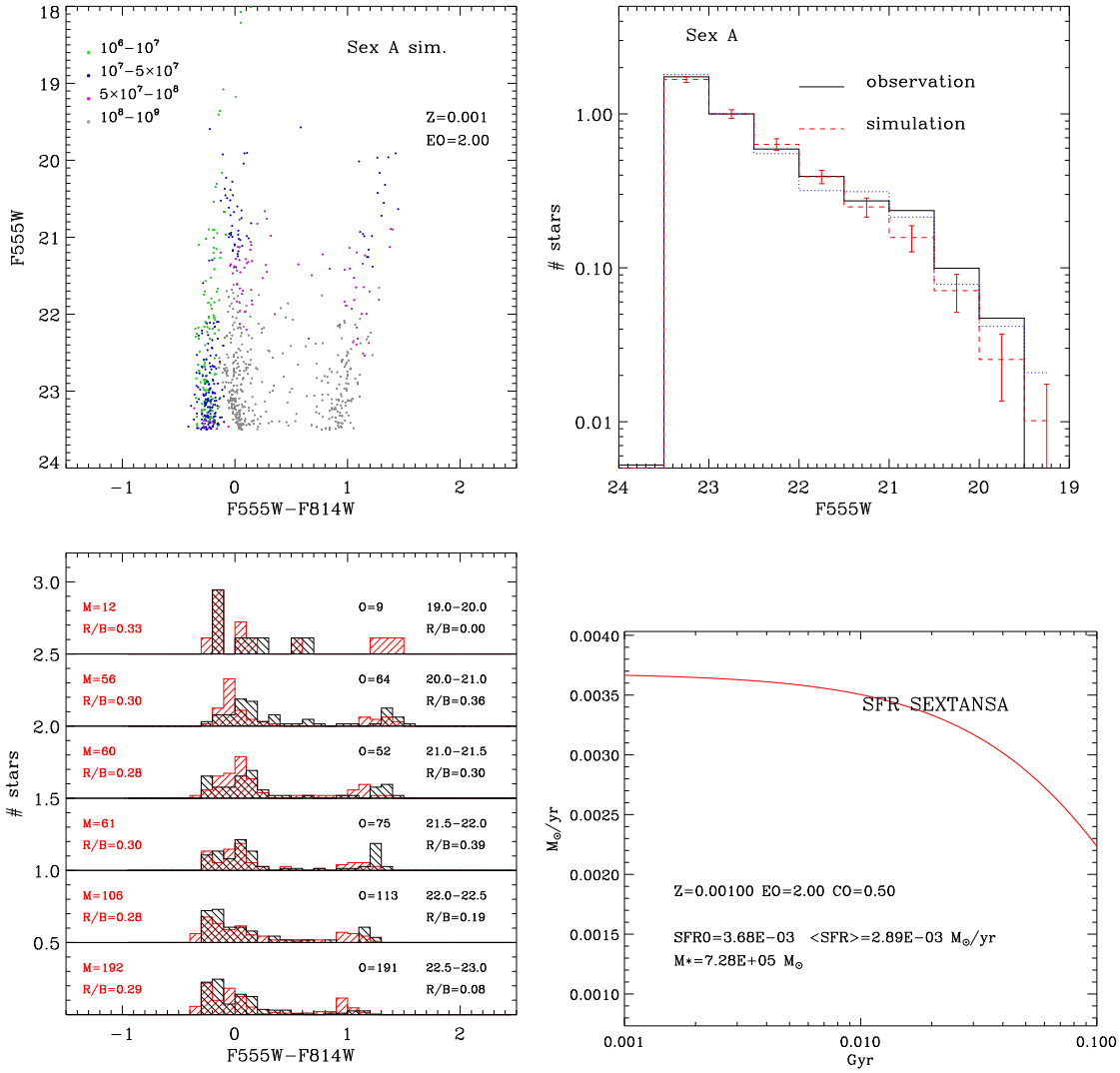

Figure 4.21: The best simulated CMD (upper left), the luminosity function (upper right), the color distribution (lower left), and the star formation history (lower right) of Sextans A, obtained with *PARSEC* increasing the envelope overshooting to EO=$2H_{\rm P}$.

models is wider than that observed. It is worth noticing that adopting a lower metal content we could remove the discrepancy between modelled and observed CMD, but this would require a metallicity value quite discrepant from the one determined from spectroscopic observations. Moreover, the value adopted in the simulations of WLM and Sextans A, Z=0.001, lies in between the ones derived observationally for the two galaxies, indicating that the origin of the discrepancy is not due the adoption of a too high metallicity. Given the inability of reproducing the observed blue loops by means of models with canonical envelope overshoot we have repeated the simulations adopting models with enhanced envelope overshoot.

The best simulations of Sextans A obtained with models with enhanced envelope overshooting are shown in Figure 4.21 and Figure 4.22 for the cases of EO=$2H_{\rm P}$ and EO=$4H_{\rm P}$, respectively. As already discussed in Section 2.2.5, models with enhanced envelope overshooting perform more extended blue loops and this is visible in the corresponding simulations. Adopting EO=$2H_{\rm P}$ produces already a reasonably

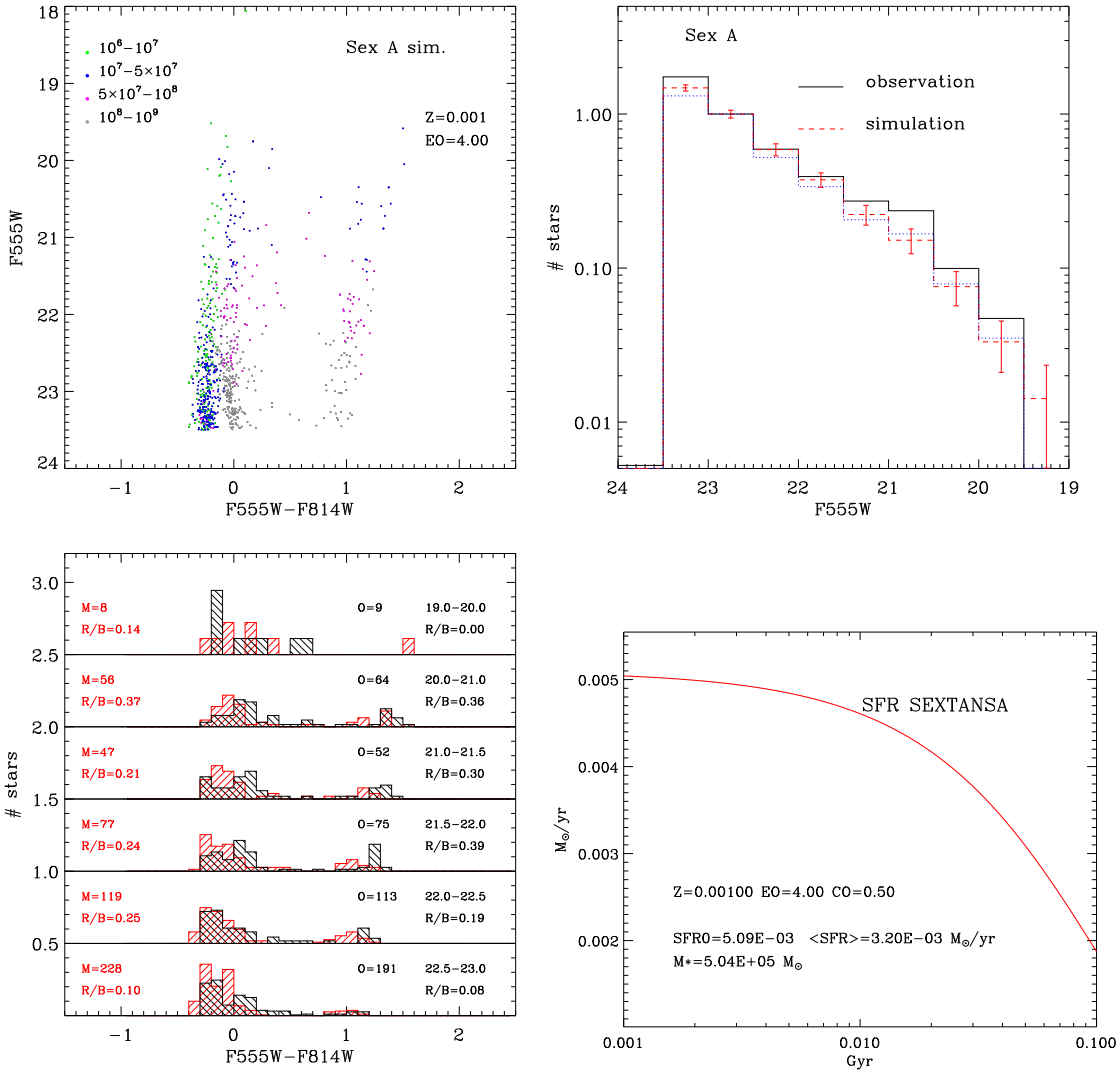

Figure 4.22: The best simulated CMD (upper left), the luminosity function (upper right), the color distribution (lower left), and the star formation history (lower right) of Sextans A, obtained with *PARSEC* for a larger envelope overshoot EO=$4H_{\rm P}$.

good fit to the observed CMD of Sextans A. The bimodal behaviour noticed in Figure 4.13 at fainter magnitudes disappears and the excess of stars in the red side of the main sequence becomes significantly less pronounced. With EO=$4H_{\rm P}$ the loops are even more extended and the predicted main sequence becomes even narrower than the observed one. The star formation rate is not significantly different from the one derived with the standard *PARSEC* V1.1 models. It increases by about 16% using the models with EO=$2H_{\rm P}$ and by another 10% if one consider the models with EO=$4H_{\rm P}$. The latter increase is in part due to the decrease of the star formation time-scale adopted for the best fit (Table 4.3).

The observed CMD of Sextans A is so well populated along the different sequences, that we may gain some insight on the properties of the different mixing models by analysing the number ratios between red ($m_{F555W} - m_{F814W}$ >0.6 and $m_{F555W} - m_{F814W} < (31.2 - m_{F555W})/7$) and blue stars ($m_{F555W} - m_{F814W}$ ≤0.6). The observed number ratios are plotted against the apparent magnitude in Figure 4.23 with large filled dots. The number ratios predicted by adopting the different values of the overshooting

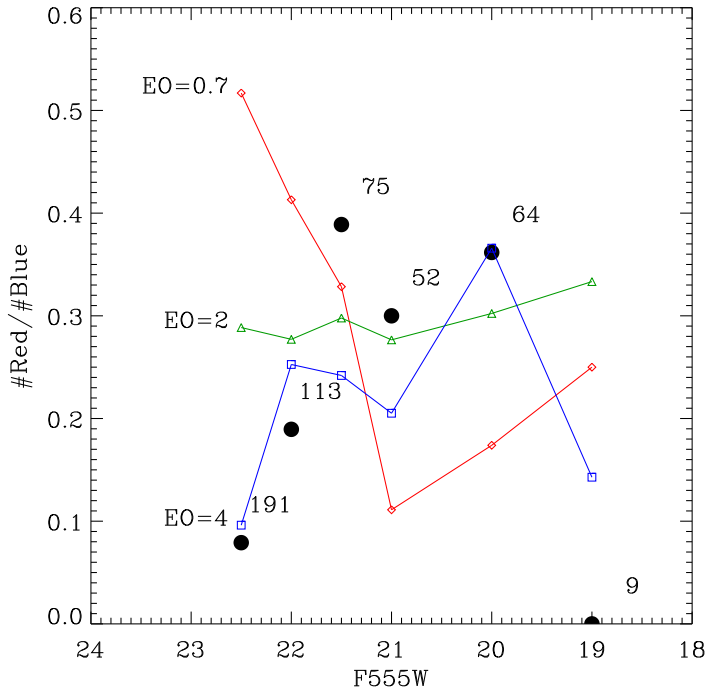

Figure 4.23: Observed (large filled dots) and predicted (colored lines with symbols) ratios between the number of stars redder and bluer than $m_{F555W} - m_{F814W}$=0.6 as a function of the apparent magnitude, in the CMDs of Sextans A. The numbers indicate the total number of stars observed in each magnitude bin. The predicted ratios are labelled with the envelope overshooting values.

scale are plotted with different symbols and colors and are labelled by the adopted overshooting scale. The size of the envelope overshooting affects not only the extension of the loop but also the relative lifetimes in the blue and red sides. In the models with larger envelope overshoot, the loops begin at earlier times during central helium burning (Figures 2.9-2.11), and the relative number of red to blue stars decreases. The observed number ratios of stars in the red and blue side of the loops have been already used to check the performance of stellar evolution models, because they concern post main-sequence phases, hence they depend almost exclusively on the lifetime ratios of the stars in the corresponding phases (e.g. Dohm-Palmer & Skillman (2002)). We cannot perform the same comparison here because we cannot disentangle the blue side of the loop and the main sequence. Indeed in Figure 4.23 we plot the ratios between the number of red stars and that of blue stars which include also the main sequence stars. Thus, these ratios are not strictly related to the above lifetime ratios not only because they include the main sequence phase but also because, by selecting them in bins of constant magnitude, we are including stars with different masses. Nevertheless, the exercise is meaningful because we are simulating the real evolution of these stars in the CMD. Indeed the figure shows that, for higher envelope overshoot, the R/B ratio decreases significantly, because the red side of the loops become less and less populated.

The best simulation of WLM obtained with these new models is shown in Figure 4.24 and Figure 4.25 for the cases of EO=$2H_P$ and EO=H_P. Again in the case of WLM the simulations performed with enhanced envelope overshooting models better agree with the observations. The relative excess of stars in the red side of the main sequence decreases significantly with EO=$2H_P$ and almost disappears with

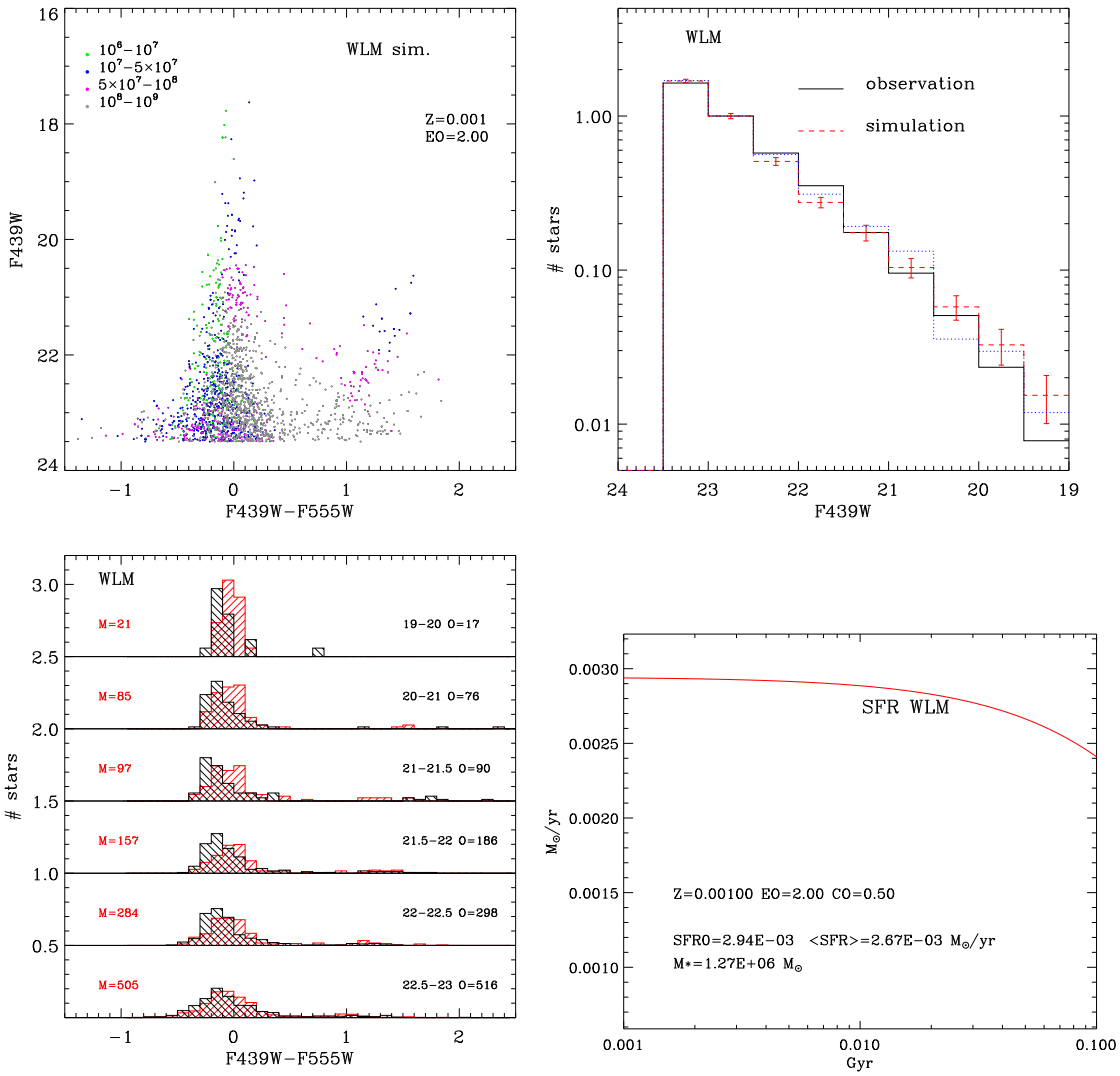

Figure 4.24: The best simulated CMD (upper left), the luminosity function (upper right), the color distribution (lower left), and the star formation history (lower right) of WLM, obtained with *PARSEC* increasing the envelope overshooting to EO=2 $H_{\rm P}$.

EO=4$H_{\rm P}$. Compared with the standard case of EO=0.7$H_{\rm P}$, the average star formation rate in the new best-match models is about 30% lower. This is due to the different IMF slope adopted in the first case, x=2.65, with respect to the one adopted in the latter cases x=2.35. For NGC6822, the best simulations obtained with models with enhanced envelope overshooting are shown in Figure 4.26 and Figure 4.27, for the case EO=2$H_{\rm P}$ and EO=4$H_{\rm P}$, respectively. Even in this case the morphology of the blue sequence is better reproduced.

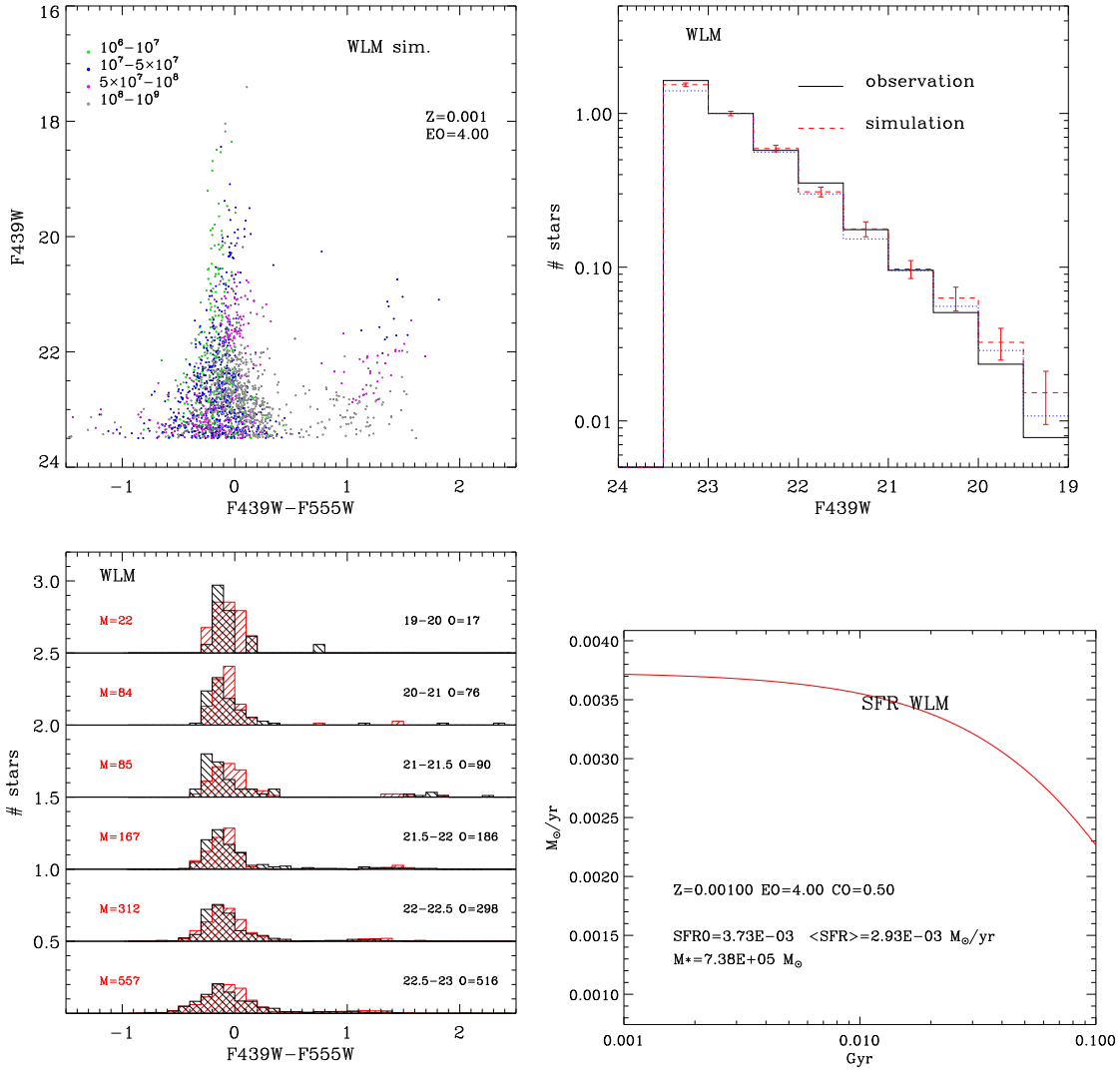

Figure 4.25: The best simulated CMD (upper left), the luminosity function (upper right), the color distribution (lower left), and the star formation history (lower right) of WLM, obtained with *PARSEC* for a larger envelope overshoot EO=4 $H_{\rm P}$.

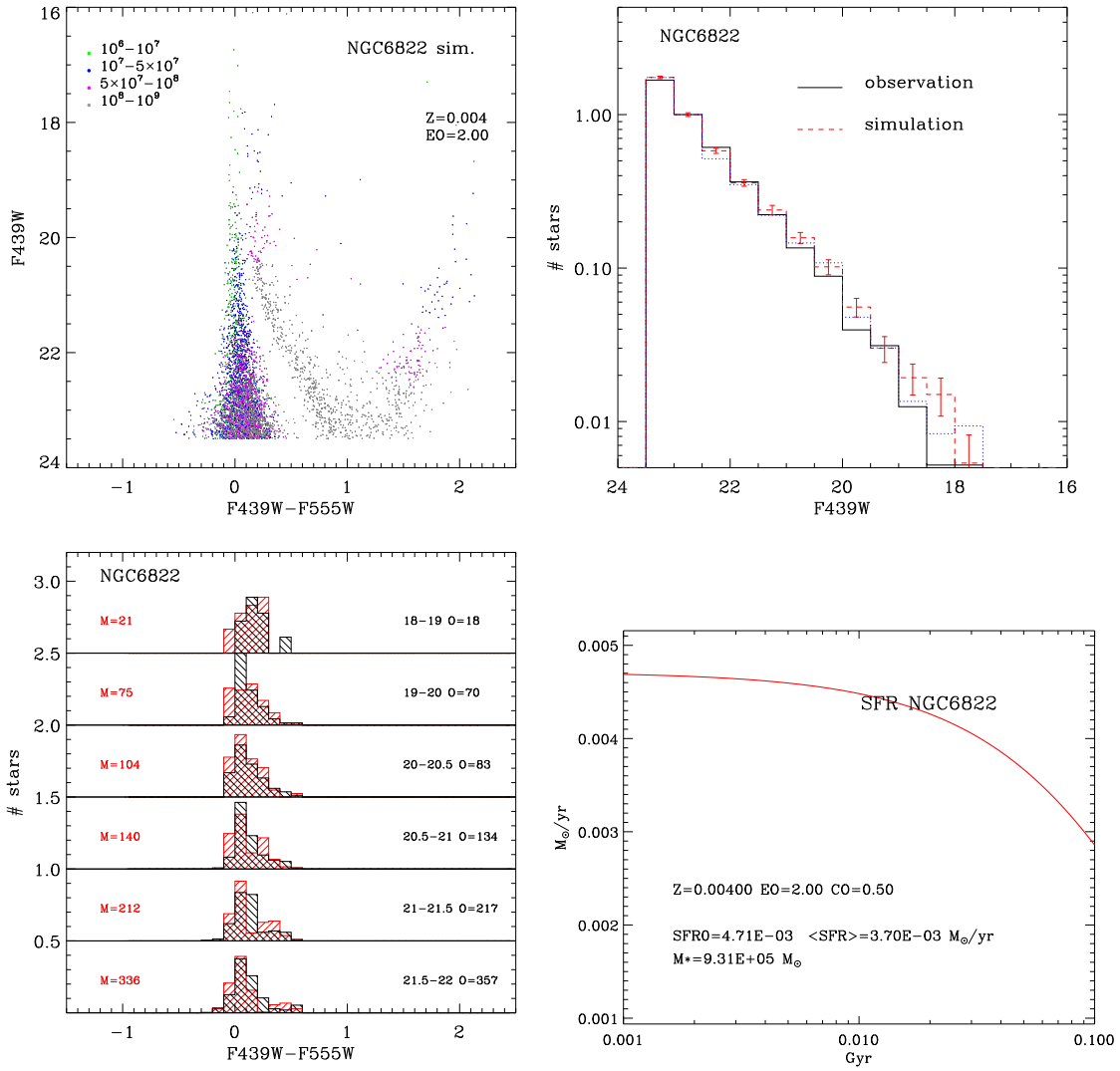

Figure 4.26: The best simulated CMD (upper left), the luminosity function (upper right), the color distribution (lower left), and the star formation history (lower right) of NGC 6822, obtained with *PARSEC* increasing the envelope overshooting to EO=2 $H_{\rm P}$.

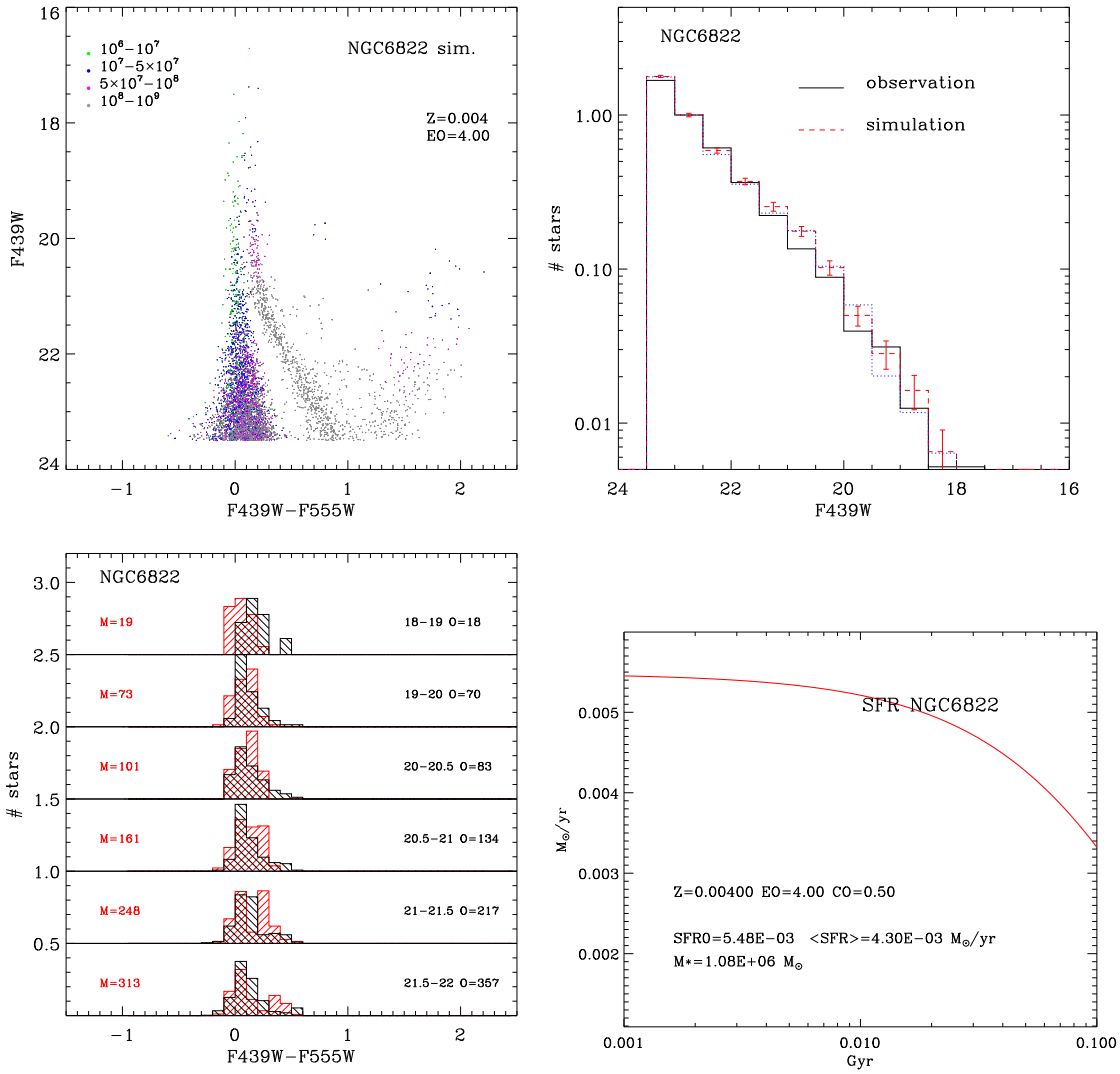

Figure 4.27: The best simulated CMD (upper left), the luminosity function (upper right), the color distribution (lower left), and the star formation history (lower right) of NGC 6822, obtained with *PARSEC* for a larger envelope overshoot EO=4 H_P .

Chapter 5

PARSEC evolutionary tracks of intermediate- and high-mass stars at metallicity Z=0.0005

In Section 4 we have analysed three well studied dwarf irregular galaxies (DIGs), Sextans A, WLM and NGC 6822, which are used to constrain the models at metallicities $0.001 \leq Z \leq 0.004$. The result of this analysis indicated that, if one keeps the extent of the core overshooting parameter fixed on the value resulting from comparison of low- and intermediate-mass stars (i.e. an overshooting length of about $0.25 H_{\rm P}$ above the unstable core), then the blue loops of intermediate- and high-mass stars are significantly reduced with respect to the models computed without core overshooting. To restore the extent of the blue loops, significant overshooting at the base of the convective envelope is required, with a typical extent of a few $H_{\rm P}$. It is worth noting that any mechanism that increases the size of the fully He exhausted region tend to shorten or even suppress the blue loops. This is also the case of models with rotational enhanced central mixing. In some cases even models computed with the usual instability criterion and without any extended mixing face the problem of lacking extended blue loops, especially at high metallicities. The goal of this study is to test if the conclusion obtained in Section 4 remains valid at very low metallicities.

5.1 Data

The Sagittarius dwarf irregular galaxy (SagDIG) is an ideal candidate to test our models at extremely low metallicity, because it is a very metal-poor star forming galaxy in the Local Group, and also it is nearby (≈1.1 Mpc) which enables the *Hubble Space Telescope* to well resolve its star content.

5.1.1 Color-magnitude diagrams

To test our models, we use deep observations of SagDIG with the Advanced Camera for Surveys (ACS) on board the Hubble Space Telescope (HST). The observations contain two-epoch data-sets (GO-9820 and GO-10472) that are separated by $\sim$ 2 years. The main body of the galaxy ($l = 21.06°$, $b = -16.28°$) was imaged in three filters: F475W, F606W and F814W. More details on the observations and data reduction can be found in Momany et al. (2014).

Due to its low latitude, SagDIG suffers a heavy Galactic contamination but Momany et al. (2014) used two epochs data to analyse the relative proper motions of all detected stars and correct for foreground contamination. The CMDs cleaned for such a contamination of SagDIG are shown in Figure 5.1, for filters F475W and F606W and for filters F606W and F814W, in the left and right panels, respectively.

The high resolution HST/ACS observations enable us to distinguish various stellar populations in SagDIG, as marked also by selected *PARSEC* evolutionary tracks overplotted in the figures. For the superposition of the evolutionary tracks we adopt a distance modulus $(m\text{-}M)_0$=25.06 and an extinction of A(F475W)=0.657 mag, A(F606W)=0.520 mag and A(F814W)=0.286 mag, respectively. These values will be discussed more extensively in a subsequent section. SagDIG is characterized by the presence of very old populations. Red giant branch (RGB) stars are indicatively marked by *PARSEC* evolutionary tracks of masses M=0.9$M_\odot$, 1.0$M_\odot$and 1.1$M_\odot$(cyan) while, for horizontal branch (HB) stars we show two helium burning tracks of M=0.85$M_\odot$and 0.95$M_\odot$(pink). Since these are meant to be the most metal poor stars in SagDIG, we have adopted a very low metallicity Z=0.0002. The turnoff stars of these old populations are not visible in the CMDs of Figure 5.1. Indeed, the deeper region of the observed main sequence, around a magnitude of $m_{F606W} \sim 27$, corresponds to the end of the H-burning phase of the track with $M \sim 1.5M_\odot$, which is the faintest track plotted in red. This track is just near the separation mass between low- and intermediate-mass stars, i.e. between those that undergo or escape the helium flash. The track of $M \sim 1.7M_\odot$already belongs to the intermediate-mass progeny and shows a well developed red clump. For all the tracks with mass $M \geq 1.5M_\odot$, we use a larger metallicity, Z=0.0005, as will be discussed below. We also note the presence of AGB stars in the continuation of the RGB tracks above the corresponding RGB tips, and few of them likely corresponding to intermediate-mass stars. The AGB population is not modelled in our simulations because the majority of it comes from older stellar populations.

Starting from the red clump we may see the locus of the bluest He-burning (BHeB) intermediate- and high-mass stars, which is clearly separated from the H-burning main sequence (MS). This locus is marked by the blue loops of the other tracks plotted in the figure, which have initial masses of M=2.3$M_\odot$, 3.0$M_\odot$, 4.0$M_\odot$, 5.0$M_\odot$, 8.0$M_\odot$and 12.0$M_\odot$. We note that the upper main sequences in the SagDIG CMDs seem to extend beyond that of the model of M=12$M_\odot$and, for this reason, we also plot the tracks with M=16.0$M_\odot$and 20.0$M_\odot$. However these tracks ignite He in the blue side of the CMDs and do not perform blue loops as the less massive ones.

The clear separation of MS and BHeB stars makes the CMD of this galaxy, especially the m_{F606W} vs $(m_{F606W} - m_{F814W})$ CMD where the separation is striking, a powerful workbench for stellar evolution

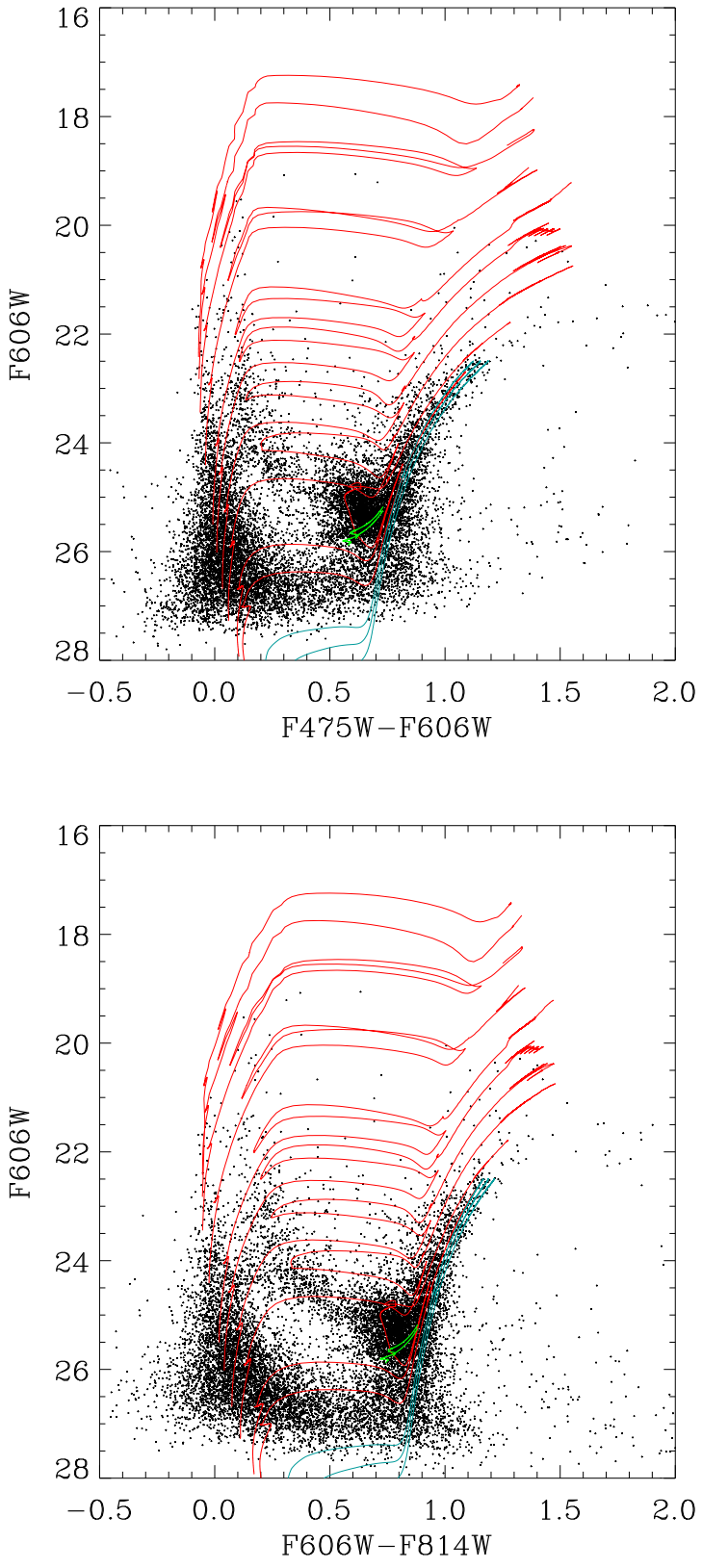

Figure 5.1: Observed color-magnitude diagrams of SagDIG and evolutionary tracks computed by *PARSEC* V1.2S with EO=0.7H_P . Cyan lines are tracks of M=0.9$M_\odot$, 1.0$M_\odot$and 1.1$M_\odot$with Z=0.0002, marking the RGB stars. Green lines mark HB evolutionary phases of stars with M=0.85$M_\odot$and 0.95$M_\odot$and with Z=0.0002. Red lines are tracks of M=1.5$M_\odot$, 1.7$M_\odot$, 2.3$M_\odot$, 3.0$M_\odot$, 4.0$M_\odot$, 5.0$M_\odot$, 8.0$M_\odot$, 12.0$M_\odot$, 16.0$M_\odot$and 20.0$M_\odot$with Z=0.0005.

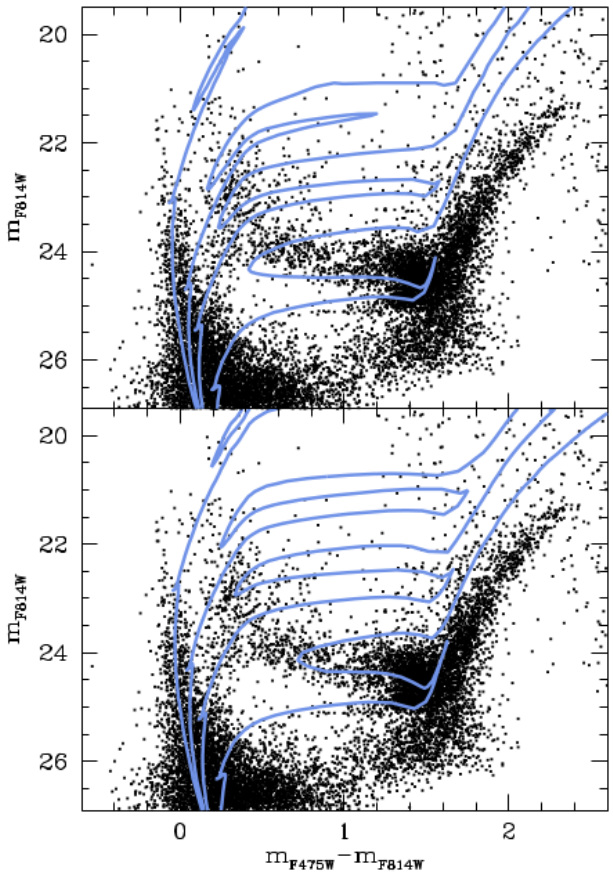

Figure 5.2: The m_{F814W} vs $(m_{F475W} - m_{F814W})$ diagram of SagDIG with theoretical isochrones from Girardi et al. (2002). Upper panel: Z=0.0001 isochrones with ages of 31.5, 100, 200, 630 Myr. Lower panel: Z=0.0004 isochrones with ages of 31.5, 89, 200, 630 Myr. This figure is from Momany et al. (2005).

models at low metallicity.

5.1.2 Metallicity of SagDIG

From the color of the RGB, Karachentsev et al. (1999) estimated the metallicity of SagDIG [Fe/H]=-2.45 ± 0.25, while Lee & Kim (2000) derived [Fe/H] in the range from -2.8 to -2.4. By comparing the color differences between the RGB stars in the SagDIG and Galactic globular clusters (GGC) fiducial lines, Momany et al. (2002) yielded a mean metallicity [Fe/H]=-2.1 ± 0.2 for the red giants, and Momany et al. (2005) gave the range [Fe/H]=-2.2 to -1.9 depending on different assumed reddening.

On the other hand, by analysing optical spectrophotometry of H_{II} regions in SagDIG, Skillman et al. (1989a) derived an oxygen abundance of 12+log(O/H)=7.42, which is in accordance with the measurement of Saviane et al. (2002) who estimated the O abundance in the range 12+log(O/H)=7.26 to 7.50. From the latter values we obtain, using for the Sun 12+log10(O/H)=8.83 and Z=0.017 (Grevesse & Sauval 1998), Z between 4.5E-4 and 7.9E-4. If instead we use the solar values 12+log10(O/H)=8.69 and Z=0.0134 (Asplund et al. 2009), we obtain Z between 5.0E-4 and 8.7E-4. We thus adopt for the young population of SagDIG a metallixity Z=5E-4 which is the lower value compatible with spectroscopic observations. We note that for the most recent populations Momany et al. (2005) infer a metallicity between Z=0.0001

and Z=0.0004, by fitting the extension of the blue loops of intermediate- and high-mass stars using the previous Padova isochrones, as shown in Figure 5.2. We see that though models with Z=0.0001 can produce more extended blue loops, the morphology of these loops is not compatible with observations. Assuming that the metallicity is the main driver of the blue-loop morphology, Z=0.0004 is favoured for this galaxy. This explains why we prefer to enlarge the envelope overshooting in models with higher metallicity.

5.2 Models with extended envelope overshooting

Not only is there a clear separation between the H-burning main sequence (MS) and the blue He-burning stars (BHeB) in the CMDs of Figure 5.1, but also red He-burning giants/supergiants (RSG) can be fairly well separated from the older red giant stars. This allows us to test different prescriptions used in building models of intermediate- and high-mass stars, in particular those that are known to affect the extension and duration of the blue loops. We model the brightest area of the CMD, which can be reasonably well represented by the last episode of star formation in SagDIG, and thus focus on stars brighter than m_{F606W}=24, where the completeness is 100%, 99.7% and 98.8% in F475W, F606W and F814W, respectively. This corresponds to a mass limit of $\sim$5.0$M_{\odot}$and $\sim$3.0$M_{\odot}$on the MS and on the He-burning phase respectively, as indicated in Figures 5.1 and 5.3.

To compare models with different envelope overshooting, we add to the CMDs of SagDIG in Figure 5.3 the evolutionary tracks computed by assuming a large value of envelope overshooting, EO=4$H_{\rm P}$, which is the largest value adopted in Section 4. These computations have been performed only for initial masses M $\geq$2.1$M_{\odot}$and the evolutionary tracks are shown in blue color. The models run superimposed to the standard *PARSEC* models computed with EO=0.7$H_{\rm P}$ up to central He ignition. Then, models with larger envelope overshooting ignite He at slightly lower luminosities (the red giant tips are fainter) and they burn central He at a significantly lower luminosity, both in the early red giant stage and in the blue loop phase. An interesting effect of a large envelope overshooting is that, in the low mass range, the new models cross the Cepheid instability strip, being 0.5 magnitude fainter than the standard ones. We also note that the blue loop is significantly more extended than that in standard models. These differences become smaller at increasing mass and practically disappear at masses M $\geq$8$M_{\odot}$. As expected, the new models reproduce fairly well the region of the observed blue He-burning stars of SagDIG. We have also computed models with EO=2$H_{\rm P}$, which lie between the two extreme cases already discussed. In the next sections we compare the simulated CMDs obtained by these models with the observed one.

5.3 Synthetic color-magnitude diagrams

To construct a synthetic CMD of SagDIG, we follow the procedure described in Section 3.2. For each of the three values of the envelope overshooting parameter, EO=0.7$H_{\rm P}$, 2.0$H_{\rm P}$ and 4.0$H_{\rm P}$, we generate a large mock catalogue.

After accounting for the distance, we add the effect of extinction and photometric errors. We may also

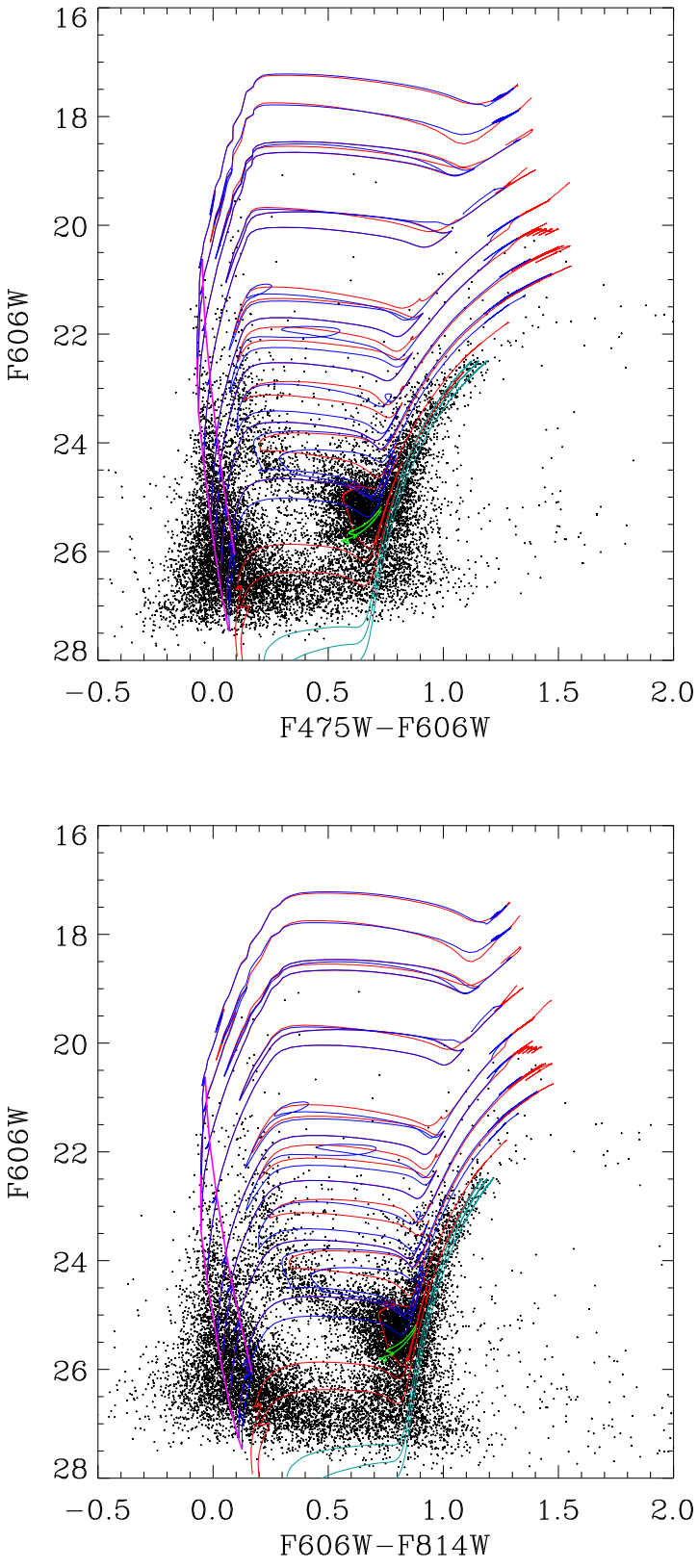

Figure 5.3: Observed color-magnitude diagrams of SagDIG and evolutionary tracks computed by *PARSEC* with EO=0.7$H_{\rm P}$ (red) and 4$H_{\rm P}$ (blue). Blue lines are tracks of M=2.1$M_{\odot}$, 2.3$M_{\odot}$, 3.0$M_{\odot}$, 4.0$M_{\odot}$, 5.0$M_{\odot}$, 8.0$M_{\odot}$, 12.0$M_{\odot}$, 16.0$M_{\odot}$and 20.0$M_{\odot}$with Z=0.0005. Pink lines mark the beginning and end of central H burning of stars with different initial masses, respectively.

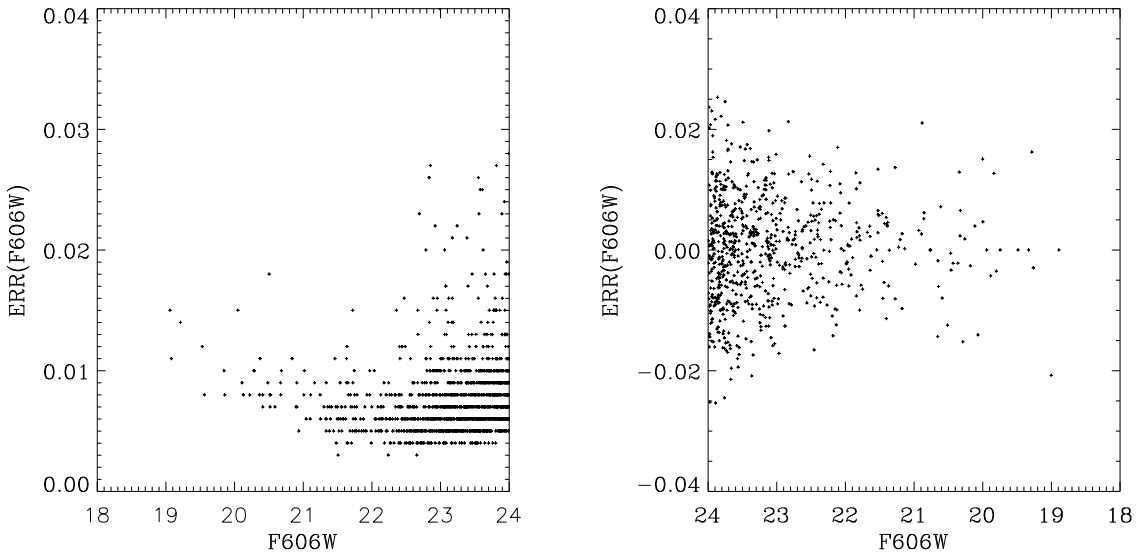

Figure 5.4: Left panel: error-magnitude plot for SagDIG in the F606W filter. Right panel: simulated photometric errors as a function of the apparent magnitude in the F606W filter.

include the effect of binarity as discussed later. We do not try more sophisticated statistical methods to reproduce the observed CMD, because our aim here is to obtain the best value of the envelope overshooting parameter to be used with the fixed metallicity Z=0.0005. Since we care about the extension of the blue loops in intermediate- and high-mass stars, we just select stars with mass $M \geq 1.9 M_{\odot}$, and also set the apparent magnitude limit to m_{F606W}=24 in the simulation.

5.3.1 Simulated photometric errors

Momany et al. (2014) have estimated the photometric errors for observed stars in SagDIG from artificial star experiments. To account for photometric errors, we first bin their results in 0.1 mag steps as a function of the apparent magnitude in each filter, and calculate the median error for each bin. Then we assign to each star in the mock catalogue an error that is randomly drawn from a Gaussian distribution with the standard deviation derived from the median corresponding to its magnitude (Section 4.2.1). We note that since the observations are very deep, the simulated errors for stars brighter than 24 mag are small ($\leq$0.03 mag), as can be seen in Figure 5.4.

5.3.2 Foreground and internal extinction

Lee & Kim (2000) estimated a low foreground reddening E(B-V)=0.06 based on the (B-V) vs (V-I) diagram, consistent with the value E(B-V)=0.07 derived by Momany et al. (2002) from the (V-I) color distribution of foreground stars toward SagDIG, as the blue cut-off of the (V-I) location is a function of reddening along the line of sight. Demers & Battinelli (2002) inferred E(B-V)$\approx$0.05 in the same way, but using (R-I) color distribution. The infrared dust maps of Schlegel et al. (1998) indicate a slightly higher reddening E(B-V)=0.12. On the other hand, spectroscopic studies of H_{II} regions in SagDIG suggest a higher reddening. Skillman et al. (1989a) calculated $c(H_{\beta})$=0.33 and E(B-V)=0.22 is derived

according to the relation $c(H_\beta) = 1.47E(B-V)$ (Seaton 1979). Saviane et al. (2002) obtained a similar value E(B-V)=0.19 from the measurement of the Balmer decrement. As this method is based on the H line ratio, the estimated value include both the foreground and the internal reddening. As young stars are physically associated with the warm interstellar medium (ISM), it is reasonable to believe they suffer higher reddening compared to old stars. This trend was also found in other dwarf irregular galaxies (Bianchi et al. 2012b; Tang et al. 2014). Bianchi et al. (2012b) derived individual star by star extinction from their multi-band data of Sextans A, WLM and NGC 6822 dwarf irregular galaxies and this information was implemented in the synthetic CMD analysis (Section 4.2.2). Since for SagDIG we lack multi-band data and cannot repeat the same procedure with the same accuracy, we deal with the extinction in the following ways. The simplest way is to use a single value of the attenuation in each photometric band, as derived from the simultaneous alignment of the observed and modelled MS stars in both the m_{F606W} vs $(m_{F475W} - m_{F606W})$ and m_{F606W} vs $(m_{F606W} - m_{F814W})$ CMDs.

For the superposition of the evolutionary tracks, we adopt a distance modulus $(m\text{-}M)_0$=25.06 and an extinction of A(F475W)=0.657 mag, A(F606W)=0.520 mag and A(F814W)=0.286 mag, respectively. These values will be discussed more extensively in a subsequent section.

5.4 Results

The observed CMD of SagDIG used to be compared is shown in Figure 5.5. The models with EO=0.7$H_{\rm P}$, 2$H_{\rm P}$ and 4$H_{\rm P}$ shown in Figures 5.6-5.8 correspond to the best fit selected from one hundred stochastic realizations made with the same parameters, based on the merit function that measures the agreement between the observed and modelled luminosity function of stars both in the main sequence and in the blue-loops evolutionary phase. The parameters of the star formation rate and initial mass function adopted in the models are listed in Table 5.1.

To compare more illustratively, we over-plot the synthetic m_{F606W} vs $(m_{F606W} - m_{F814W})$ CMDs of SagDIG obtained with the three different values of envelope overshooting on the observed one, as shown in Figures 5.9-5.11. The observed CMD is represented by black points, while the best simulation is shown in green color. The simulation refers to the stars brighter than m_{F606W}=24. For ease of comparison, we draw the observed fiducial main sequence, which is indicated by the almost vertical black line at $(m_{F606W} - m_{F814W}) \sim 0$. It has been obtained by considering the median of the colors of main sequence stars, defined as the stars bluer than (m_{F606W}-m_{F814W})=(m_{F606W}-18)/65, in magnitude bins of Δm_{F606W}=0.5 in the range $21 \leq m_{F606W} \leq 24$. The horizontal bar represents the standard deviation for the corresponding magnitude bin. It is calculated as the median absolute deviation, which is defined as the median of an array of differences between the colors of stars and the median color. The fiducial main sequence locus derived from the best fit CMD is shown in red color. Since the evolution up to central H exhaustion is not affected by envelope overshooting, the main sequence loci are the same in the three simulated CMDs. The superposition of the observed and simulated main sequence loci has been obtained by assuming a single value of the extinction for all stars in each of the three different photometric bands, A(F475W)=0.657 mag, A(F606W)=0.520 mag and A(F814W)=0.286 mag respectively. The adopted

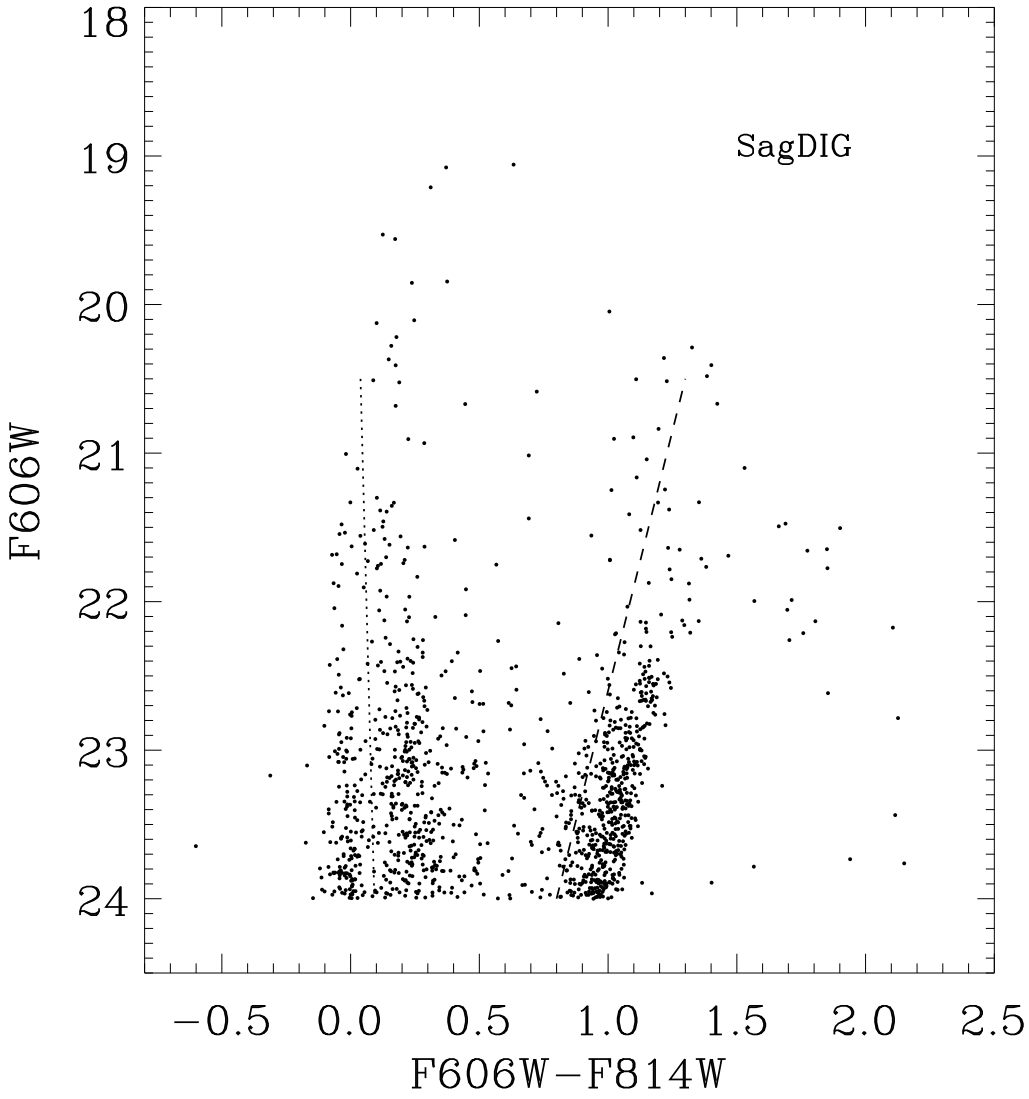

Figure 5.5: Observed color-magnitude diagram of SagDIG. The dotted line marks the separation of MS and BHeB stars. The dashed line illustrates the sequence of RSG.

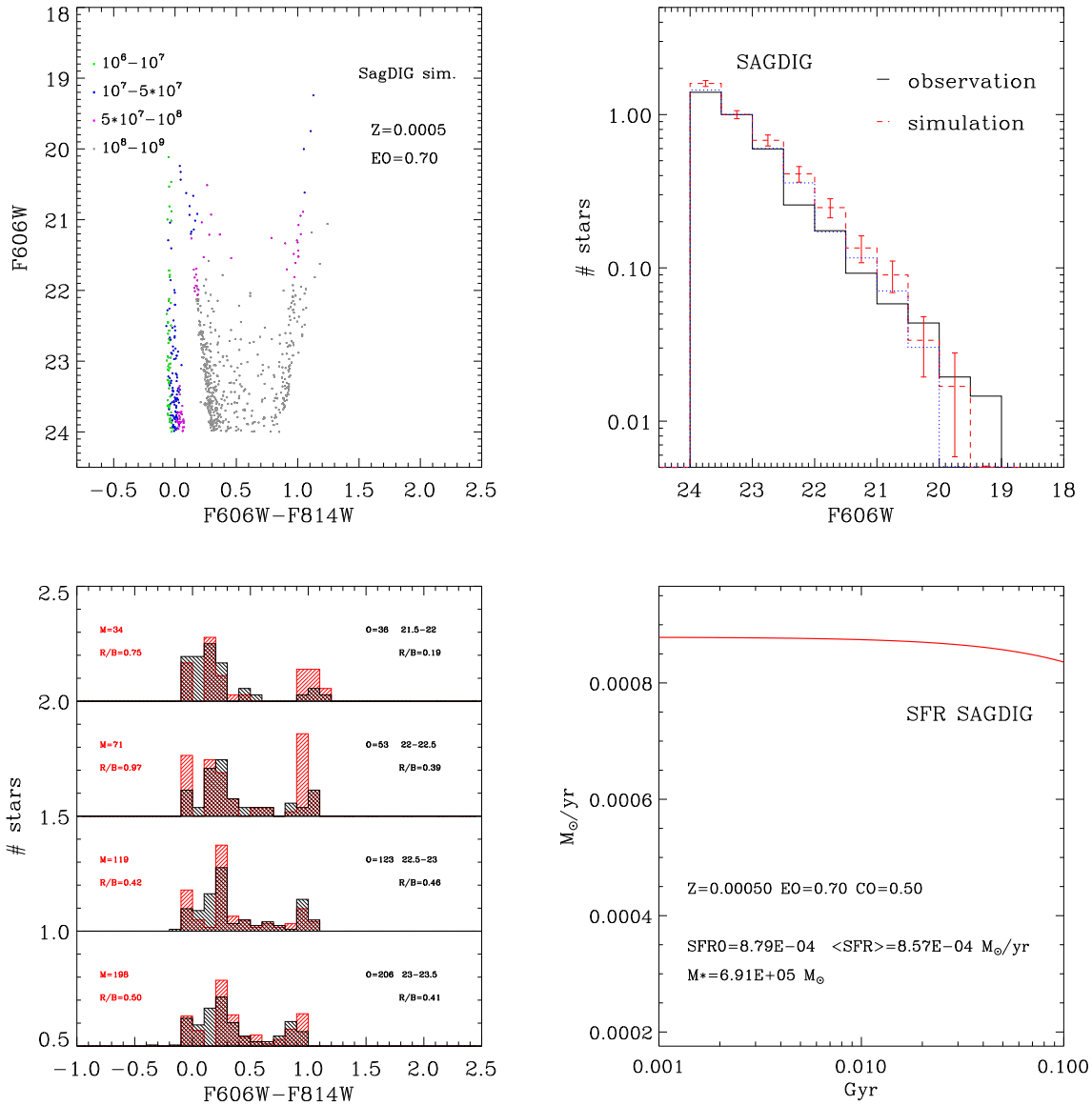

Figure 5.6: The best simulated CMD (upper left), the luminosity function (upper right), the color distribution (lower left), and the star formation history (lower right) of SagDIG, obtained by *PARSEC* V1.2S with EO=0.7H_P .

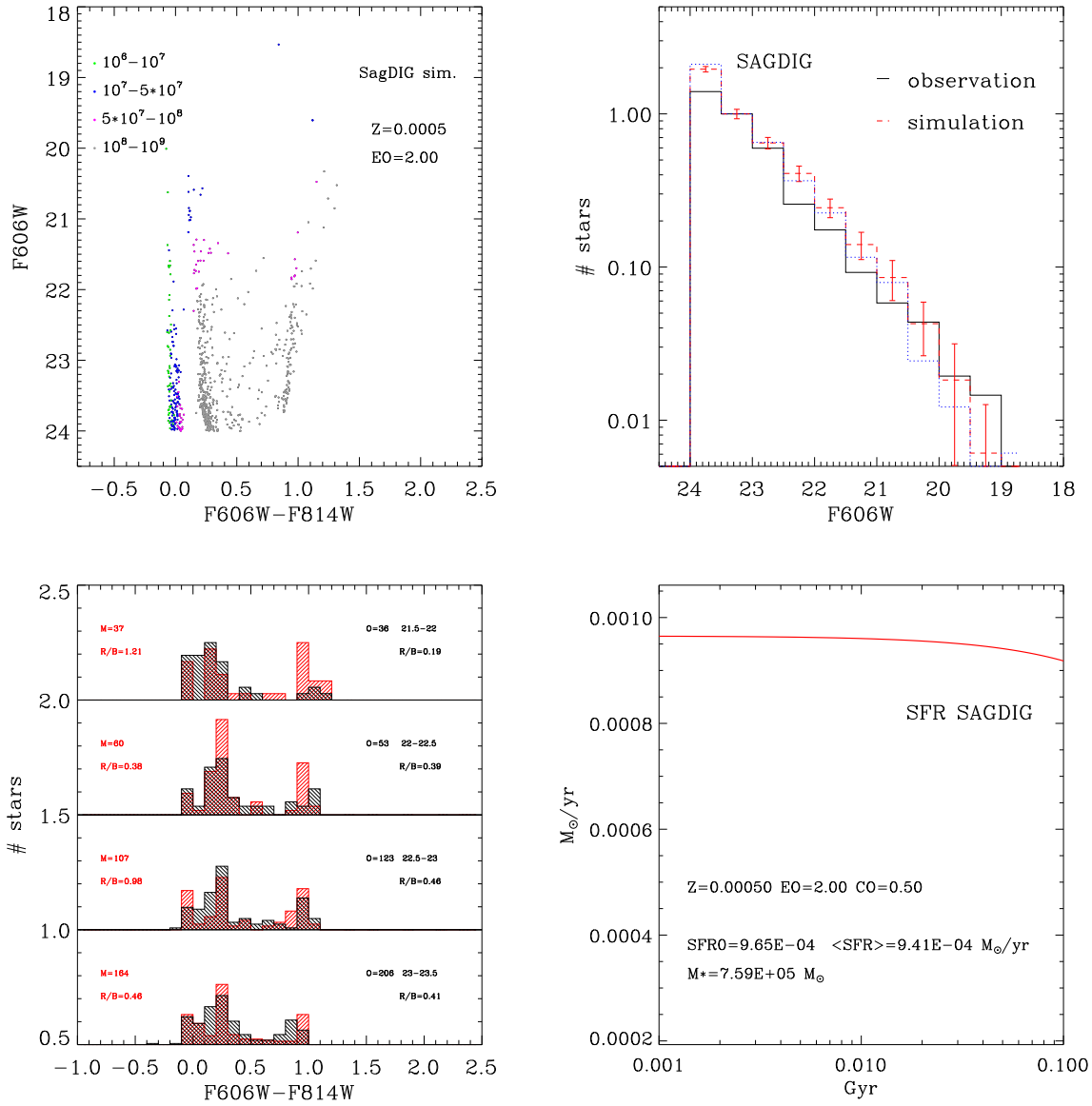

Figure 5.7: The best simulated CMD (upper left), the luminosity function (upper right), the color distribution (lower left), and the star formation history (lower right) of SagDIG, obtained with *PARSEC* increasing the envelope overshooting to EO=$2H_{\rm P}$.

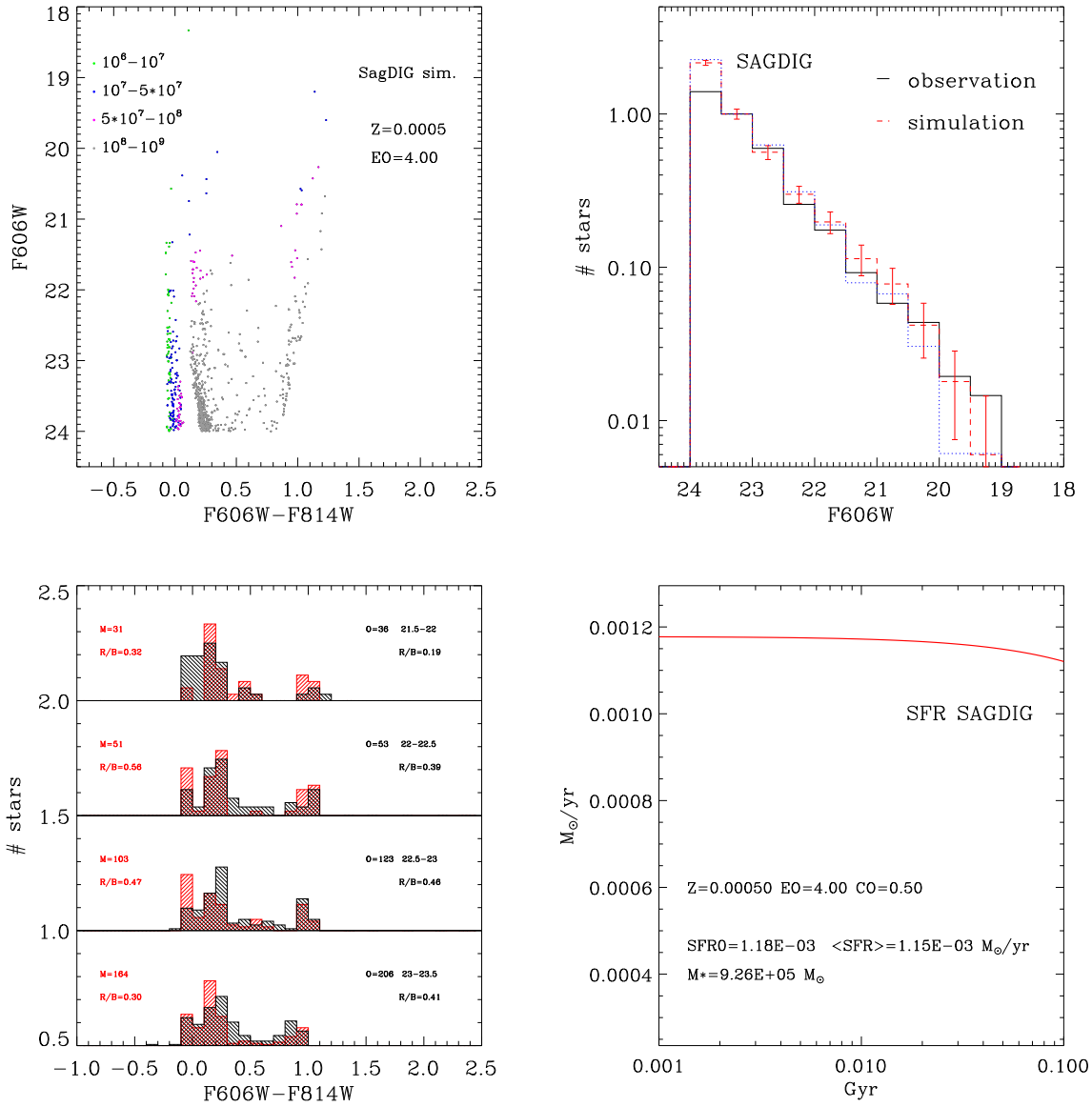

Figure 5.8: The best simulated CMD (upper left), the luminosity function (upper right), the color distribution (lower left), and the star formation history (lower right) of SagDIG, obtained with *PARSEC* increasing the envelope overshooting to EO=4$H_{\rm P}$.

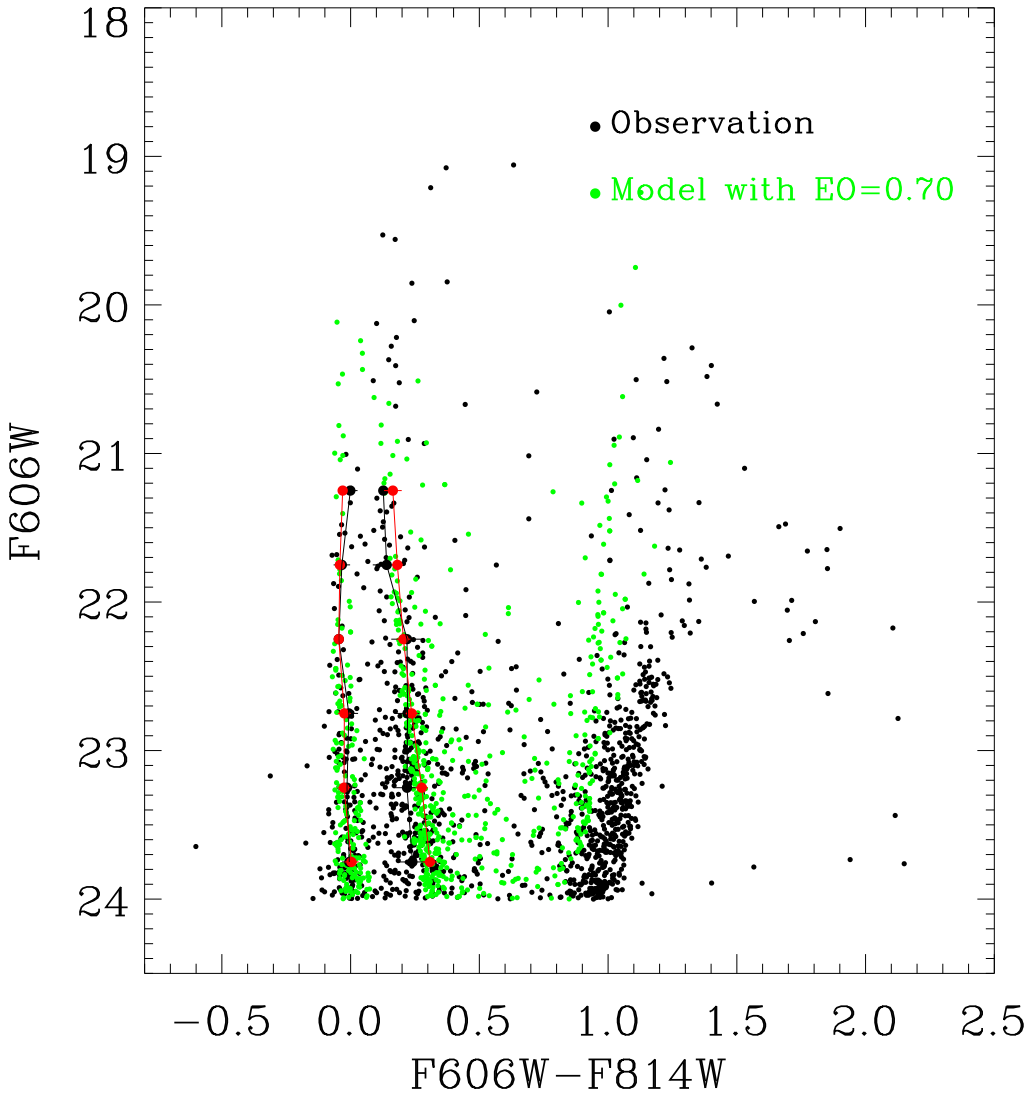

Figure 5.9: Comparison of observed and modelled CMDs, EO=0.7H_P . The observation and simulation are represented by black and green points, and the corresponding medians and fiducial lines are marked in black and red, respectively. The error bars are calculated as the median absolute deviation.

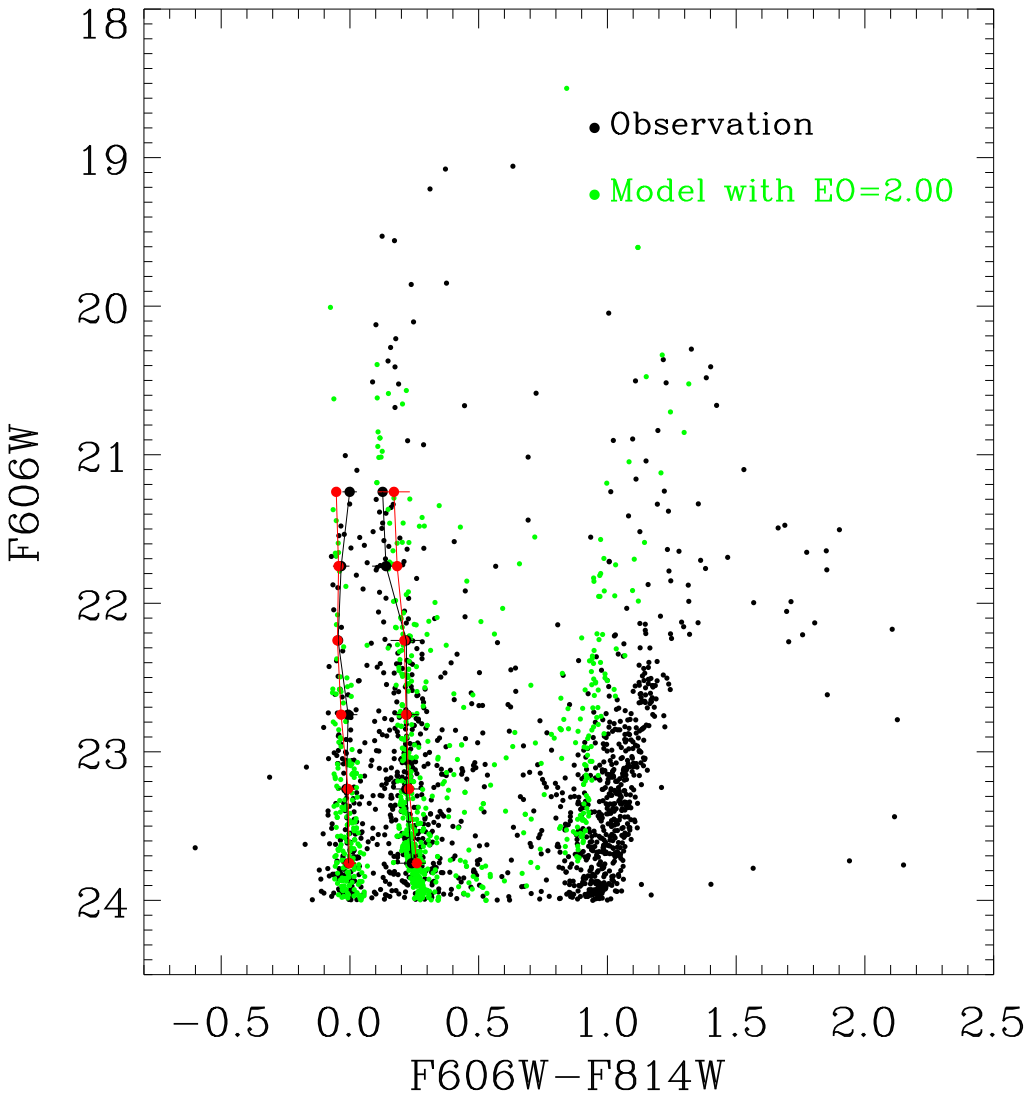

Figure 5.10: Comparison of observed and modelled CMDs, EO=2$H_{\rm P}$.

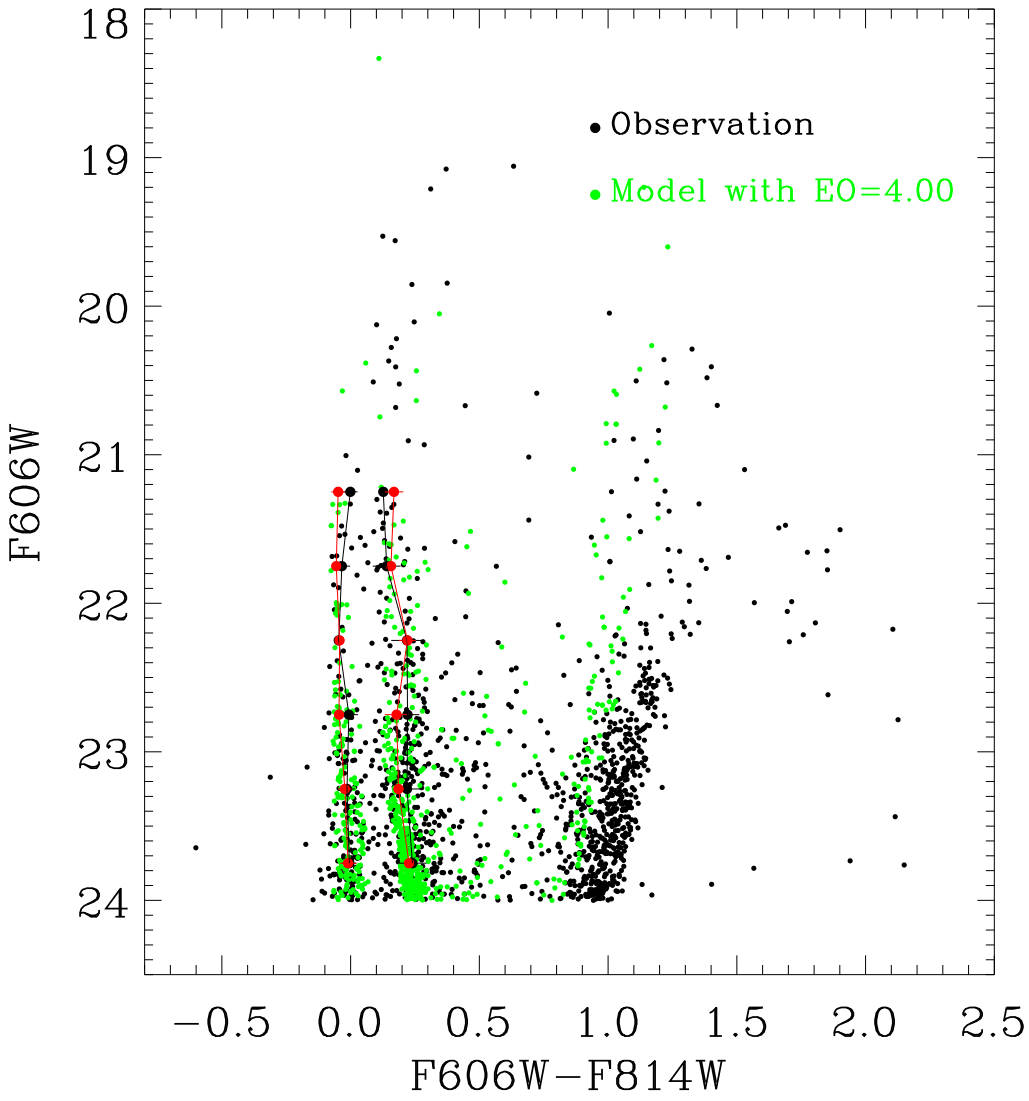

Figure 5.11: Comparison of observed and modelled CMDs, EO=4$H_{\rm P}$.

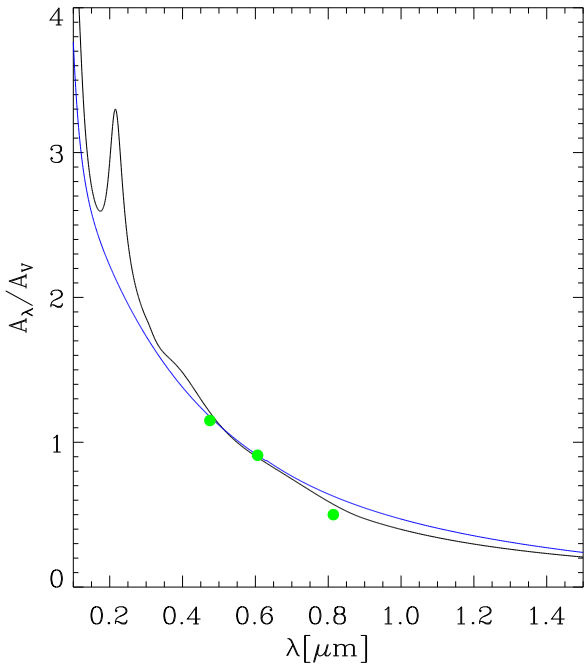

Figure 5.12: The reddening curve A_λ/A_V is shown as a function of λ. Our values A_λ/A_V for different photometric bands are shown by green solid dots. The black and blue line represent the Galactic extinction law (Cardelli et al. 1989b) and the Calzetti Law (Calzetti et al. 1994), respectively.

distance modulus is $(m\text{-}M)_0$=25.06. These values of extinction and distance modulus have also been used to draw the evolutionary tracks on the CMDs in Figures 5.1 and 5.3. Adopting A_{F606W}/A_V=0.91 (as in the Galactic extinction law with R_v=3.1), we get A_V=0.57. We compare the quantities A_{F475W}/A_V and A_{F814W}/A_V with those corresponding to other typical extinction laws in Figure 5.12. We see that the value of A_{F475W}/A_V lies on the Calzetti extinction curve (Calzetti et al. 1994), while the one of A_{F814W}/A_V falls slightly below the Galactic one (Cardelli et al. 1989b).

The synthetic CMDs reproduce fairly well the main features of the observed one, except for the RGB. This is because we focus on newly-formed stars, and exclude stars redder than the line (m_{F606W}-m_{F814W})=(29.95-m_{F606W})/7 which, as shown in Figures 5.1 and 5.3, correspond to the RGB of the old populations. We note however that the simulated green-dot sequence in the case with EO=0.7H_P, representing red giant stars of the intermediate age populations, seems to be more populous than the corresponding data, while the discrepancy gets smaller at increasing value of *EO*.

As discussed in Section 4.4, models with enhanced envelope overshooting produce more extended blue loops, which is also shown in Figure 5.3. But the simulations show two other interesting properties. One is that, at increasing envelope overshooting, the relative fraction of blue He-burning stars increases while that of red He-burning stars decreases, explaining the better agreement between the simulated and observed red giants obtained with EO=4H_P. The other is that the population of yellow He-burning stars, say those with $0.4 \leq (m_{F606W} - m_{F814W}) \leq 0.7$, decreases at increasing envelope overshooting. This is particularly evident in the magnitude range $23 \leq m_{F606W} \leq 24$.

The effect of envelope overshooting on the extension of the blue loops can be appreciated already

by eye from Figures 5.6-5.8, but in order to render it more clear, we derive the BHeB stars main locus by using the same method adopted for the main sequence locus. The bins are the same used for the main sequence stars, though we recall that, at fixed initial mass, He-burning stars are brighter than H-burning ones. In order to derive the median color we have considered all stars redder than (m_{F606W}-m_{F814W})=(m_{F606W}-18)/65 and bluer than (m_{F606W}-m_{F814W})=($m_{F606W} - m_{F814W}$)=0.4. The meaning of the error bar is the same as the one obtained for MS stars. The median locus of the observed BHeB stars is drawn in black and it runs almost parallel to the main sequence locus, but about 0.25 mag redder. The locus of the synthetic BHeB stars is drawn in red. For EO=0.7$H_{\rm P}$, it is 0.1 mag redder than the observed one at magnitudes $23 \leq m_{F606W} \leq 24$. At brighter magnitudes the difference disappears. The locus of the models with envelope overshoot EO=2$H_{\rm P}$ runs superimposed to that of the observed data, in the magnitude range $23 \leq m_{F606W} \leq 24$, while using the models with envelope overshoot EO=4$H_{\rm P}$, it is slightly bluer than the observed one, in the same magnitude range $23 \leq m_{F606W} \leq 24$. We note that the difference between the observed and modelled BHeB loci is not large, even in the case of EO=0.7$H_{\rm P}$. Actually in the latter case the largest difference is comparable to the standard deviations of the loci themselves. However if we base our judgment more on the systematics of the effect than on its entity, it is clear that only models with larger envelope overshooting are able to reproduce the extension of the blue loops in the magnitude range $23 \leq m_{F606W} \leq 24$.

5.4.1 The star formation rate

As indicated in Section 3.2, the star formation rate is represented by an exponential parametrization

$$SFR(t) = SFR_0 \times exp(\frac{t}{\tau}) \tag{5.1}$$

where t represents the stellar age, $\rm SFR_0$ the current value of the SFR and τ the characteristic e-folding time. The results are shown in Table 5.1. We find that the SFR in SagDIG increases toward recent times ($\tau < 0$). Considering the case of EO=2$H_{\rm P}$, the average SFR in the last 100 Myr (∼9E-4$M_{\odot}$/yr) is significantly lower than that we obtained for Sextans A (<SFR>=2.9E-3$M_{\odot}$/yr), WLM ((<SFR>=2.7E-3$M_{\odot}$/yr)) and NGC 6822 ((<SFR>=3.7E-3$M_{\odot}$/yr)). It is worth noting that this average SFR is for the whole galaxy, while in those three galaxies the derived SFR refer to selected star-forming regions. We also notice that the SFR does not change much for models with different envelope overshooting, but in the case with high envelope overshooting, EO=4$H_{\rm P}$, the SFR turns out to be ∼ 30% larger than that in the case of EO=0.7$H_{\rm P}$. Correspondingly, the mass formed in the recent burst amount to M*=9.22E5$M_{\odot}$with EO=4$H_{\rm P}$, while it is relatively smaller in the other two cases, M*∼7E5$M_{\odot}$. Our value is close to that of Karachentsev et al. (1999) who found <SFR>=6.6±0.8E-4$M_{\odot}$/yr in the age range 0.05-0.2 Gyr. Indeed, in the same period, we find <SFR>=8.2E-4$M_{\odot}$/yr using models with EO=0.7$H_{\rm P}$. In Table 5.1 we also show the masses of the most massive and of the brightest stars found in the simulations.

Table 5.1: Parameters of the CMD simulations of SagDIG

EO	τ	α	SFR_0	<SFR>*	M_{max}	M_{bright}
	yr		$M_\odot$/yr	$M_\odot$/yr	$M_\odot$	$M_\odot$
0.7	-2E9	2.05	8.79E-4	8.57E-4	39	11
2	-2E9	2.25	9.65E-4	9.41E-4	62	13
4	-2E9	2.15	1.18E-3	1.15E-3	30	30

*the average SFR in the last 100 Myr

5.4.2 Effects of differential extinction and binary stars

A remarkable property of the CMDs shown in Figure 5.6-5.8 is that the standard deviation of the observed fiducial sequences are larger than the modelled ones. This indicates that both the observed main sequence and the observed BHeB sequence are more dispersed than that predicted by the models, at least for stars brighter than m_{F606W}=24. This cannot be ascribed to photometric errors because, besides being explicitly included in the simulation, they are by far too small to explain the effect. Thus other explanations have to be found.

In the case of the main sequence, the discrepancy could be due to the well known *main sequence widening* effect, i.e. that the termination point of the observed main sequence is cooler than that predicted by the models. This could be appreciated in the comparison between the observed CMD and the evolutionary tracks in Figure 5.3 where the width of the main sequence is marked by the pink lines. This discrepancy is one of the motivations that inspire the presence of extended mixing effects during the central H-burning phase of intermediate- and high-mass stars (Massevitch et al. 1979; Bressan et al. 1981). In the case of the BHeB stars, the problem does not have a similar explanation. The star number counts in the evolved phases are proportional to the evolutionary lifetimes of the corresponding phases, and to explain a large dispersion one should invoke a mechanism that is able to slow down the transition from the RSG to the BSG phases which is at present not known.

There are two other effects that could explain the widening of the sequences.

One is differential extinction. We have already mentioned that in previous analysis of DIGs, Bianchi et al. (2012b) and Tang et al. (2014) have directly measured and then modelled differential extinction of individual stars. This effect certainly contributes to the widening of both the main sequence and the blue He-burning sequence and thus helps filling the gap between them. But unfortunately, at variance with the quoted DIGs, in the case of SagDIG we lack the broad multiband photometry which allows Bianchi et al. (2012b) to obtain estimates of attenuation for individual stars. Nevertheless we may try to estimate the size of this effect, by assuming that the models are correct. Applying the same method used in Section 4.2.2, we derive a more realistic estimate of the extinction of individual stars, according to the trend of increasing attenuation at increasing luminosity, as shown in the diagram A(F606W) vs F606W of Figure 5.13. Adopting the differential extinction we obtain the synthetic CMDs shown in Figures 5.14-5.16. The comparison of simulated and observed CMDs are shown in Figures 5.17-5.19. While the gap can be partly filled by introducing the differential reddening, it remains evident in the case of EO=0.7H_P . The gap decreases in the case of EO=2H_P and almost disappears when a high envelope overshooting is adopted, EO=4H_P . The fiducial lines of the main sequence and of the BHeB stars, drawn in the same way as

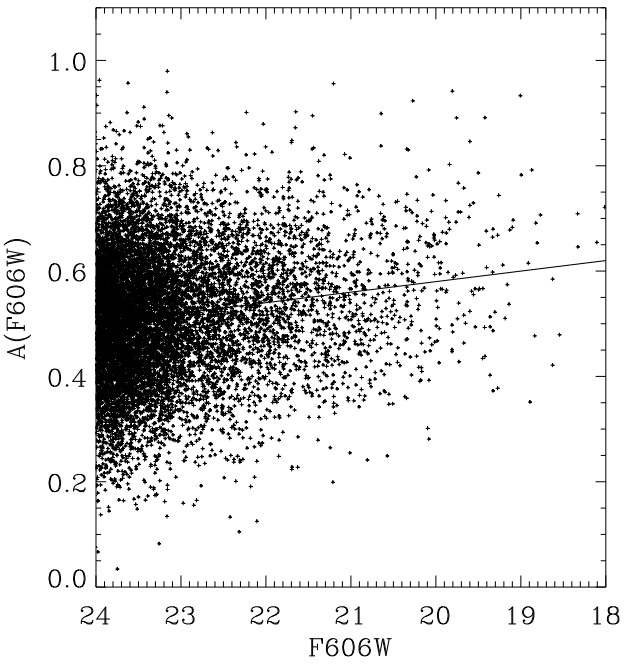

Figure 5.13: Differential extinction is assumed as a certain dispersion around a mean value A(F606W)=-0.02 × m_{F606W}+0.98 (black line).

in Figure 5.6-5.8, show that the fact that the models with the standard value of envelope overshooting, EO=0.7$H_{\rm P}$, are not able to reproduce the observed extended loops during central He-burning phase, is not due to neglecting differential extinction. Even with differential extinction a large value of envelope overshooting (EO∼2.0$H_{\rm P}$) is favoured.

Another effect that may contribute to widen the theoretical nominal sequences of single stars is the presence of binary stars. As is well known, the incidence of binaries is high, of the order of 50% (Duquennoy & Mayor 1991). The binary fraction appears higher for more massive stars, reaching 70% (Abt et al. 1990) and decreasing to 40% for M dwarfs (Kroupa et al. 1993).

In order to estimate the effect of binaries on synthetic CMDs, we run a model with a percentage of binaries of 50%. To reproduce the assumed 50% contamination, we randomly combine the sample stars in the mock catalogue without assuming a particular value of the mass ratio, until we reach the total number of observed objects with the required binary fraction. Since for binaries consisting of equal-mass components the apparent magnitude may increase by up to 0.75 mag, to obtain a complete estimate of their effect above m_{F606W}=24, we first work on stars brighter than m_{F606W}=25. After taking into account the luminosity increase due to binarity, we select objects brighter than m_{F606W}=24 and bluer than the line (m_{F606W}-m_{F814W})=(29.95-m_{F606W})/7, for stars redder than this line are considered as RGB stars. We further randomly choose stars as many as the observed data from this subset catalogue. This procedure is repeated one hundred times to obtain the best-fit model, the average luminosity function and its standard deviation at the selected magnitude bins. In this case we adopt a fixed extinction, as discussed in the previous section. Figure 5.21 shows the simulated CMD obtained by the models with EO=2$H_{\rm P}$ and a binary fraction of 50%. The inset shows the distribution of the mass ratios $q = M_2/M_1$

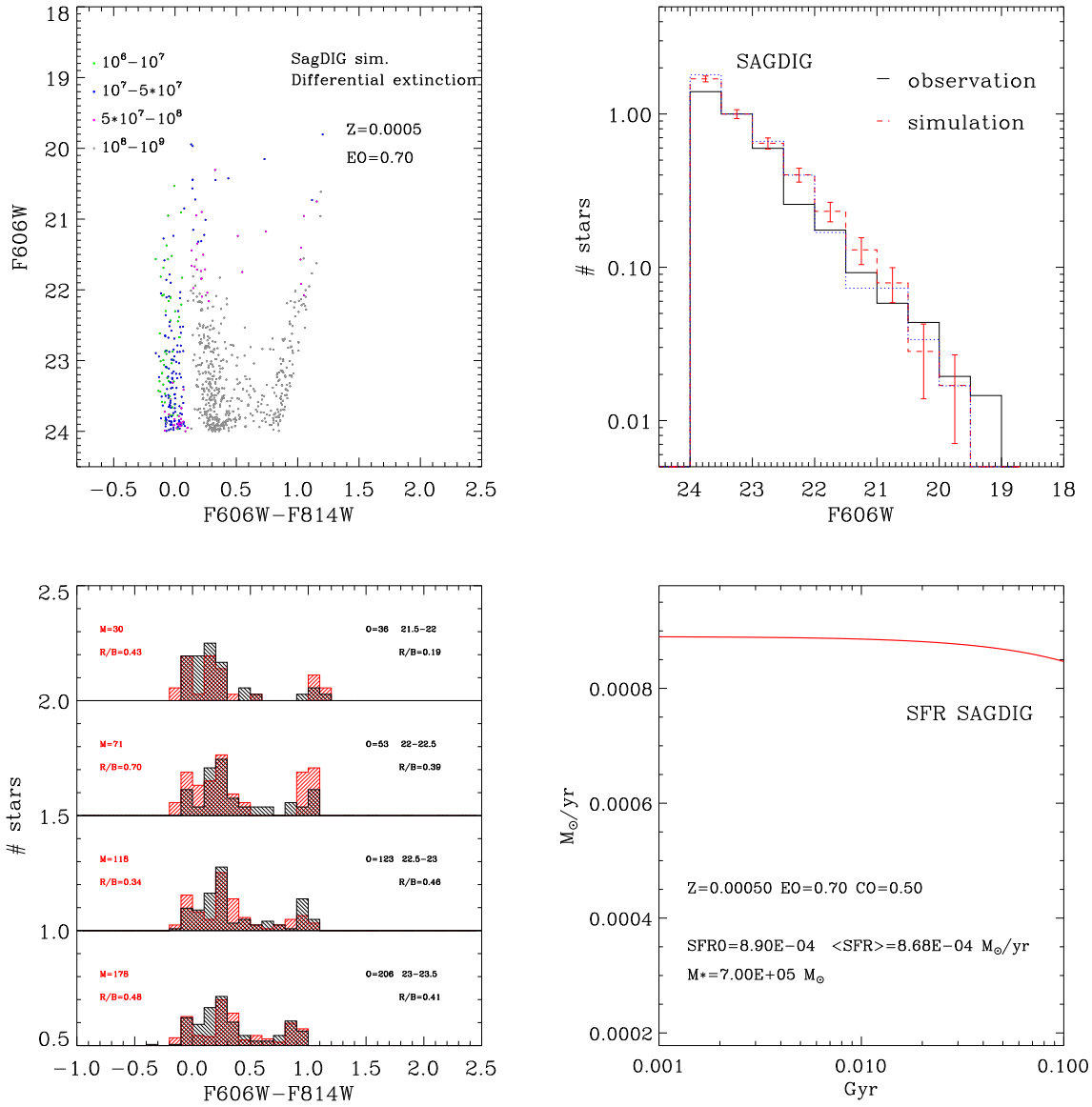

Figure 5.14: The best simulated CMD (upper left), the luminosity function (upper right), the color distribution (lower left), and the star formation history (lower right) of SagDIG, obtained by *PARSEC* V1.2S with EO=0.7H_P and differential extinction.

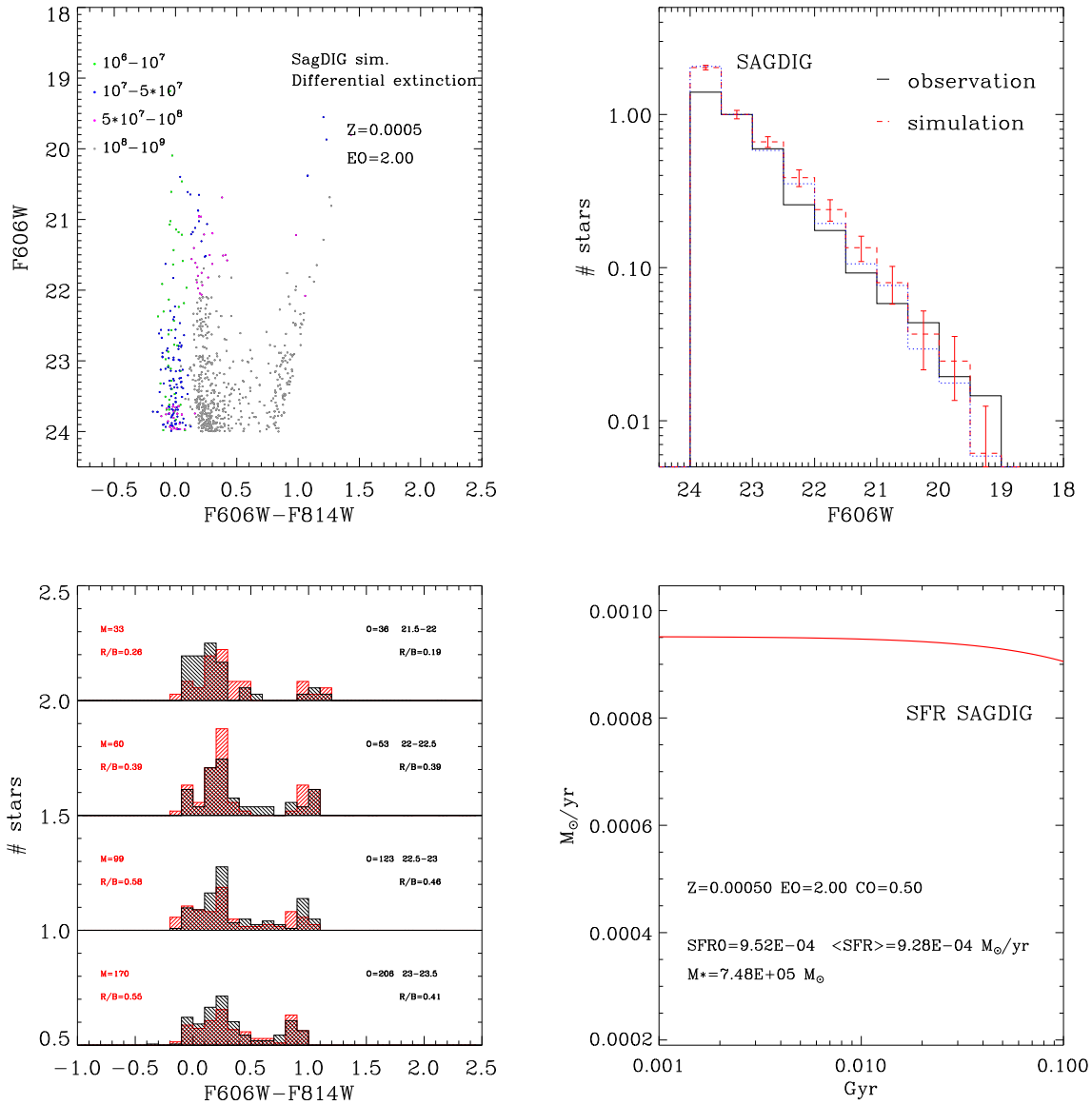

Figure 5.15: The best simulated CMD (upper left), the luminosity function (upper right), the color distribution (lower left), and the star formation history (lower right) of SagDIG, obtained by *PARSEC* with EO=2$H_{\rm P}$ and differential extinction.

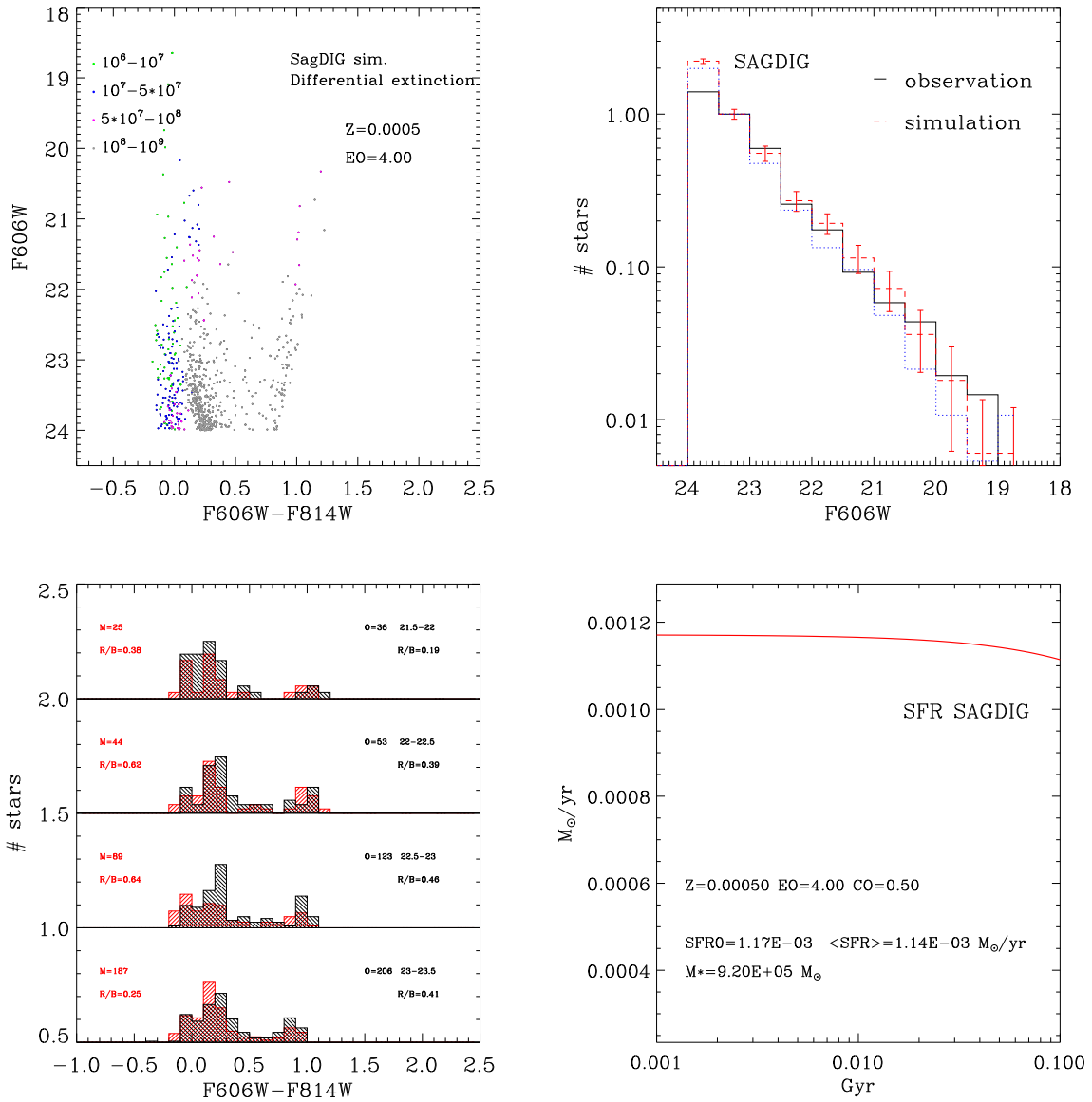

Figure 5.16: The best simulated CMD (upper left), the luminosity function (upper right), the color distribution (lower left), and the star formation history (lower right) of SagDIG, obtained by *PARSEC* with EO=4H_P and differential extinction.

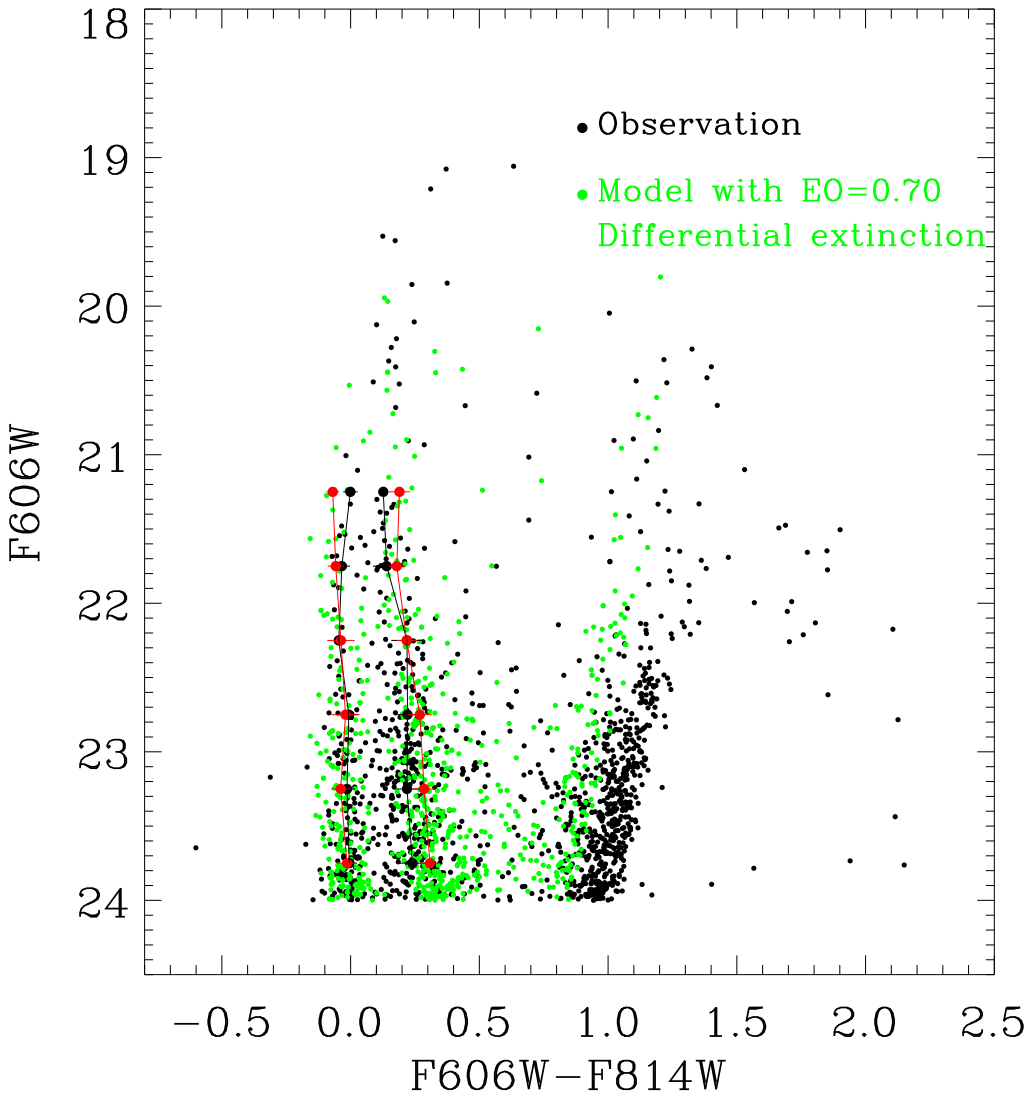

Figure 5.17: The best model obtained by *PARSEC* V1.2S with EO=0.7$H_{\rm P}$ and differential extinction.

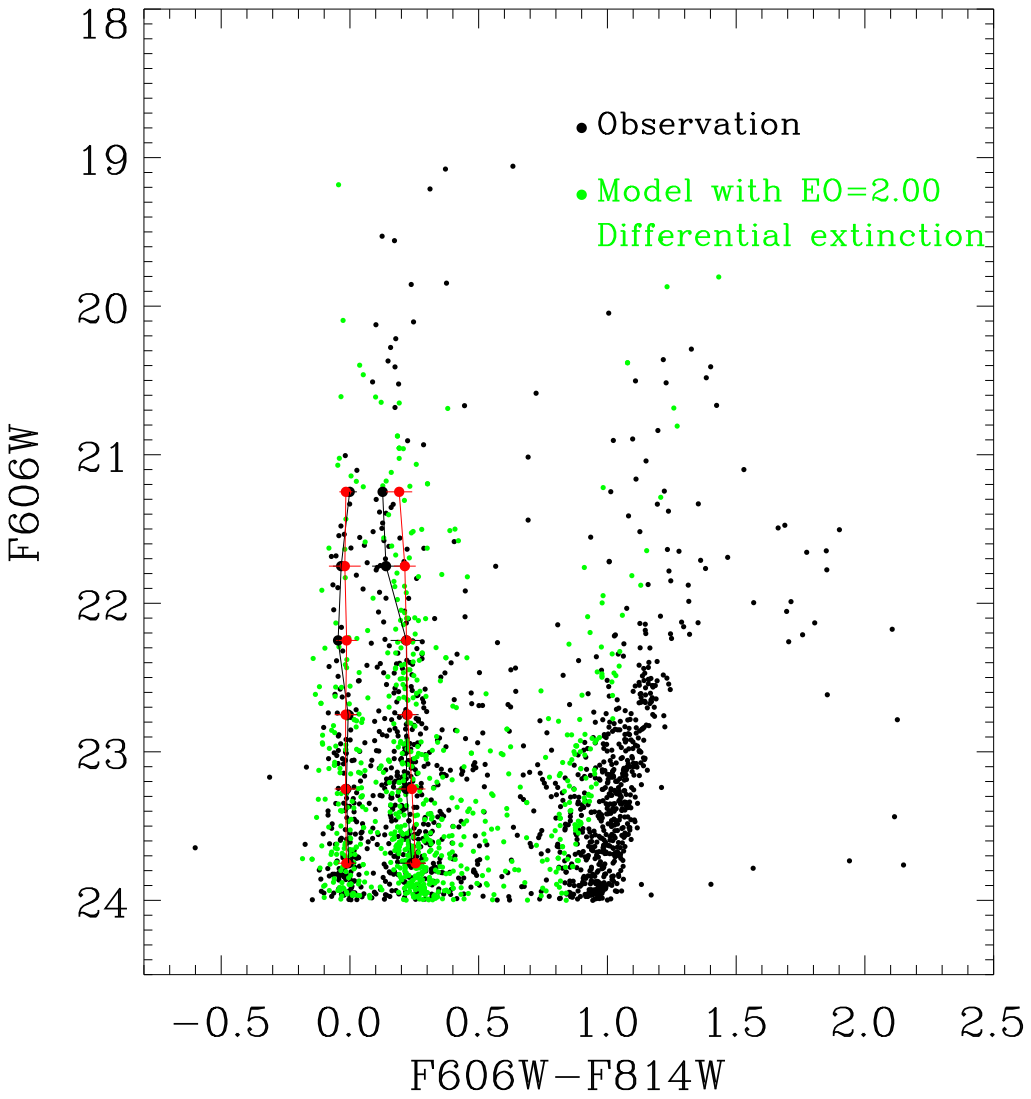

Figure 5.18: The best model obtained by *PARSEC* with EO=2$H_{\rm P}$ and differential extinction.

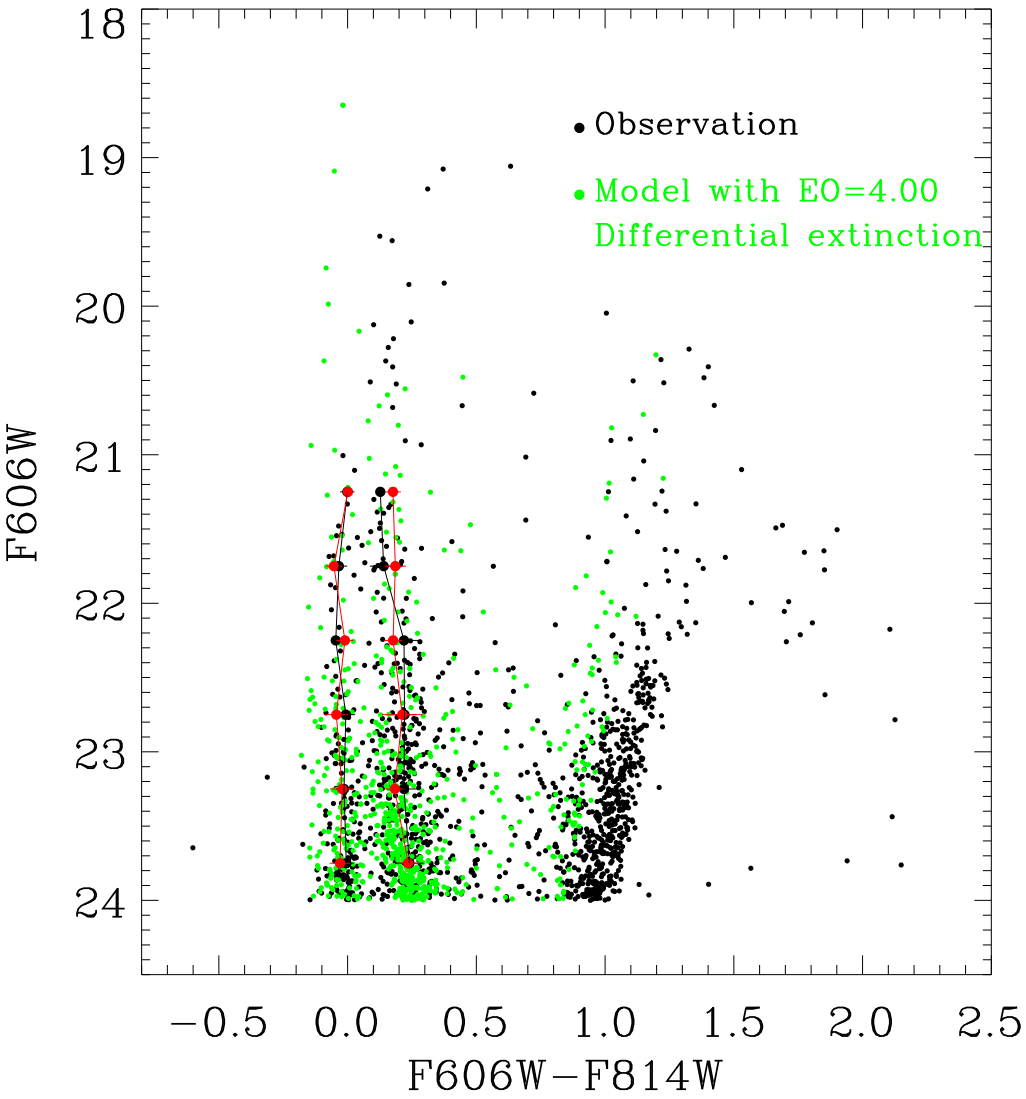

Figure 5.19: The best model obtained by *PARSEC* with $4H_{\rm P}$ and differential extinction.

between the primary and secondary components, which is consistent with a flat distribution (Mermilliod et al. 1992).

Compared to Figure 5.7, we see the effect of binaries is to broaden the main sequence and also the BHeB sequence. The number of stars falling between these two sequences is larger than that in the case computed without considering binaries. However the BHeB sequence is clearly split into two parallel sequences between $23 \leq m_{F606W} \leq 24$, and the red He-burning sequence seems also too broad, as part of these stars move to the location of yellow giant/supergiant. In particular the splitting of the BHeB seqence is not seen in the observed diagram, perhaps indicating that either the assumed binary fraction or the resulting mass ratio are too high for this galaxy of low metallicity. Furthermore, because of the asymmetric behaviour of the superposition of star pairs in the CMD, the fiducial lines shift toward the red side and, in order to reconcile the model with the observations, one should make use of a lower attenuation, by a factor $\delta(m_{F606W} - m_{F814W})$ ~0.02.

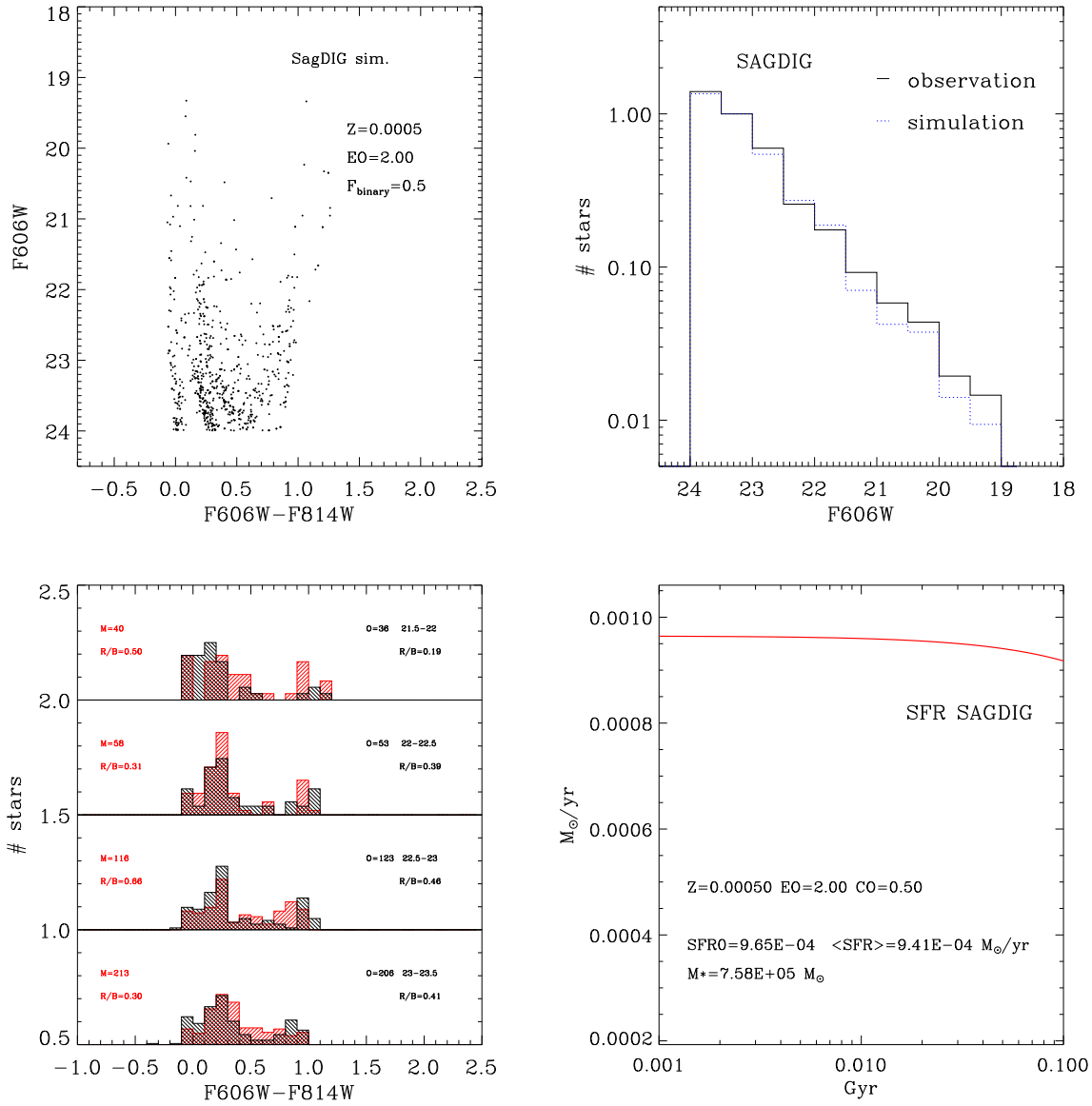

Figure 5.20: The best simulated CMD (upper left), the luminosity function (upper right), the color distribution (lower left), and the star formation history (lower right) of SagDIG, obtained by *PARSEC* with EO=$2H_{\rm P}$ and binary fraction F=0.5.

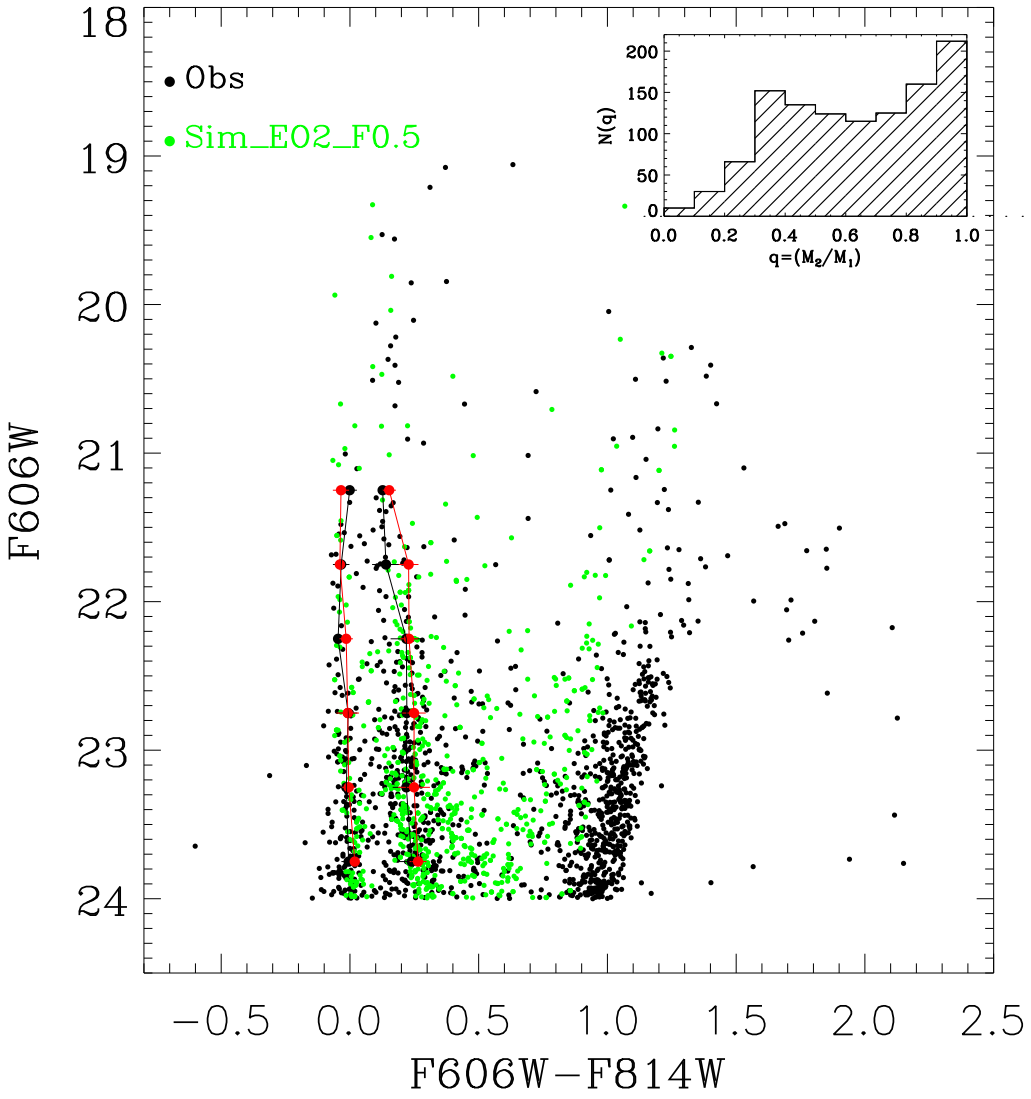

Figure 5.21: The best model obtained by *PARSEC* with EO=2H_P and binary fraction F=0.5. The insert shows the mass ratio distribution of binaries.

Chapter 6

Conclusions

With the aim of extending the new library of stellar evolutionary tracks and isochrones computed with *PARSEC*, we begin the calculation of new evolutionary tracks of massive stars. We adopt the same input physics used in the *PARSEC* V1.1 published version of low- and intermediate-mass stars, the only difference being that for masses $M \geq 14M_{\odot}$we include mass-loss. The new calculations supersede the old stellar evolution tracks of massive stars (Bertelli et al. 1994), so that we now provide updated and homogeneous sets of evolutionary tracks from very low (M=0.1$M_{\odot}$) to very massive (M=350$M_{\odot}$) stars, from the pre-main sequence to the beginning of central carbon burning.

In this thesis, we first introduced the basic physics in the theory of stellar evolution, especially the concept of the convective overshooting. Meanwhile we presented new evolutionary tracks of low metallicity, Z=0.001 (Figures 2.3-2.5), Z=0.004 (Figures 2.6-2.8) and Z=0.0005 (Figures 5.1, 5.3).

We notice that at fixed metallicity models with larger envelope overshooting can produce more extended blue loops. We then discussed if the adoption of different convective criteria for the determination of the unstable region could affect the extension of the blue loops. On one hand, it has already been shown in the past that adopting the Ledoux criterion may favour the development of extended blue loops (Chiosi & Summa 1970). On the other hand, the fact that the problem of short blue loops is found even in the tracks of intermediate-mass stars, for which the results should be independent of the adopted instability criterion because they do not possess intermediate unstable region (within the profile of chemical composition), suggests that the reason should be different. By analyzing a model of M=12$M_{\odot}$and Z=0.004 under standard *PARSEC* assumptions, which evolves without performing a blue loop, we find that the Ledoux criterion tend to *suppress* the blue loop, in the sense that the star favours the red-ward evolution after central H burning. This is apparently in contrast to the results reported by Chiosi & Summa (1970), who indicated that the Ledoux criterion favours the blue loop. However, a thorough inspection of that seminal paper shows that their model with the Schwarzschild criterion does not perform a blue loop only because it begins central He burning already in the blue loop region, i.e. as a BHeB star. With a series of new models not reported here for seek of conciseness, we show that at He ignition, the mass pocket between the H-exhausted core and the H/He discontinuity is already negligible, fully confirming the finding of Walmswell et al. (2015). The Schwarzschild criterion allows the formation of

a larger intermediate convective shell than in the case of the Ledoux criterion, and this convective shell pushes the H/He discontinuity deeper in the star, reducing the above mass pocket. Thus the case A model in Chiosi & Summa (1970) begins He burning already in the BHeB equilibrium configuration and not in the RSG stage, without the need of performing a blue loop. On the contrary, their case B model, with the Ledoux criterion, encounters the condition of a thin mass pocket between the H-exhausted core and the H/He discontinuity, slightly later during the evolution, after He ignition in the RSG phase, and thus performs a blue loop. When significant core overshooting is allowed during the H-burning phase, the situation changes critically. Being the H-exhausted core larger than that in the case without core overshooting, its contraction after central H-burning is stronger, pushing the star into the RSG stage, independently of the adopted instability criterion. These are the two cases shown in Figure 2.13 for M=12$M_{\odot}$and Z=0.004. However, though the differences between the models computed with the two different criteria are minimal, the track computed with the Schwarzschild criterion develops a larger intermediate convective region that deepens slightly the H-He discontinuity than in the one computed with the Ledoux criterion. The former develops the blue loop while in the latter case the condition of a thin intermediate layer is encountered only toward the end of central He burning, when the BHeB structure is no more a possible configuration for the star so that it burns the entire central He in the RSG stage.

In order to test these tracks against observations of nearby dwarf galaxies, Sextans A, WLM, NGC 6822 and SagDIG, we need to construct synthetic CMDs. Since the new massive star tracks have not yet been implemented in the popular CMD simulators (e.g. TRILEGAL) we built our own CMD simulator, where we specify the IMF and SFR laws, the metallicity, the photometric errors, attenuation and binary effects. In the simulations, we fix the metallicity to the value which is the nearest to that found in literature for the youngest populations of the galaxy, either stars or gas. This is important because our aim is to check the model results by using the morphology of the CMD, in particular of the BHeBS, which is known to depend significantly on the metallicity. The photometric errors are taken from the published photometry catalogues and are reproduced statistically as a function of the apparent magnitude. Concerning the attenuation by IS dust, for Sextans A, WLM and NGC 6822, we exploit the advantage that it has been individually derived for a large sub-sample of stars, by means of a star by star multiband spectro-photometric analysis (Bianchi et al. 2012b). In these three galaxies, the attenuation is characterized by an average value that rises with the intrinsic luminosity for the hot stars and by a significant dispersion, which is consistent with an age selective extinction together with local variations of the dust content. Only by including such a dispersion and trend with luminosity we may reproduce the morphology of the different sequences seen in the CMD, without a real need to use a dispersion in metallicity. This is especially true for Sextans A where the photometric errors are very small while, in the case of NGC 6822, there is still room for a dispersion in metallicity, which indeed has been observed in this galaxy, and is not surprising given its patchy star-formation episodes. For SagDIG we lack multi-band data and cannot estimate the attenuation in this way. We therefore use a single value of the reddening in each photometric band derived from the superposition of the observed and modelled MS fiducial lines.

First of all, we performed comparison of the new tracks with observed CMDs of star forming regions in three selected nearby metal-poor dwarf irregular galaxies, Sextans A, WLM and NCG 6822. These

galaxies are dominated by the last ongoing star-burst and the existing HST CMDs are a useful workbench for testing the overall performance of stellar evolution tracks in the domain of intermediate-mass and massive stars. The contamination by Milky Way dwarf stars, estimated with TRILEGAL simulations, is negligible in Sextans A and WLM, while for NGC 6822 it is significant at colours $m_{F439W} - m_{F555W} \geq 0.6$: for this galaxy we used only bluer stars, which include the main sequence and the blue helium-burning sequence.

For Sextans A and WLM we adopted a metallicity Z=0.001, which is an upper limit for the former and a lower limit for the latter. In both galaxies the location of the main sequence is well reproduced by the new tracks. Sextans A shows a well populated red sequence which is also fairly well reproduced by the new models. In Sextans A the main sequence and BHeBS form two parallel vertical sequences while in WLM they from a broad blue sequence. All models generally reproduce these sequences but, a quantitative comparison of the colour distribution in different magnitude bins shows that, for models with canonical overshooting, the simulated distributions are broader than the observed ones and generally skewed toward redder colours, in both galaxies. A lower metallicity, which would render the blue loops more extended, would be discrepant with measured values, therefore we interpret this mismatch as evidence that the BHeBS predicted by the models are not hot enough.

For NGC 6822 we adopt a metallicity of Z=0.004. As for the previous galaxies, the fit of the main sequence is fairly good, but at this metallicity the problem of the blue loops is even more exacerbated. The models computed with *PARSEC* V1.1 (canonical overshooting) show a shortening of the loops above $\log(L/L_{\odot})\sim3.5$ (Figure 2.6) and the corresponding simulation shows a blue sequence with bimodal colour distribution which is not evident in the observed CMD. This corroborates the notion that even at Z=0.004 the BHeBS predicted by the models are not hot enough and that, in order to reproduce the observed morphology of the CMD with the *PARSEC* V1.1 prescriptions, a metallicity much lower than the measured values would be required.

We show that this discrepancy is overcome by extending the overshooting at the base of the convective envelope. The simulations made with the enhanced EO models, better reproduce the observed CMDs for all the three galaxies. For Sextans A the comparison can be extended to the number ratios between stars in the red side of the loop and blue stars (including also main sequence stars). The comparison with the observed ratios strongly support the largest value, EO=$4H_{\rm P}$. Thus there is evidence that an EO larger than that adopted in *PARSEC* V1.1 should be preferred. Apart from the morphology (and corresponding luminosity function) of the loops, there are no other significant differences between models computed with different EO scales. The SFR, estimated from the best-match model in each case, increases by less than $\sim$15% at increasing EO mixing, and so it is not significantly affected by the choice of this parameter. We also find that a Salpeter slope for intermediate-mass and massive stars is, in general, the preferred choice to reproduce the observed luminosity function.

It is worth noticing that the mixing scales required to reproduce the observed loops, EO=$2H_{\rm P}$ or EO=$4H_{\rm P}$, are definitely larger than the maximum values compatible with e.g. the location of the RGB bump in evolved low mass stars, which can be well reproduced by an envelope overshooting not exceeding EO=$0.7H_{\rm P}$, the value adopted in *PARSEC* V1.1 for intermediate-mass stars. Thus the results suggest

a strong dependence of the mixing scale below the formal Schwarzschild border of the outer envelope, with the mass or luminosity of the star. A possible mechanism at the origin of such enhanced mixing could be the large discontinuity in angular momentum that develops between the outer envelope and the inner core during the first dredge-UP, when stellar rotation is included. The shear generated by this discontinuity could give rise to the required enhancement. However it is interesting to note that current models that consistently include rotational mixing in the whole star interiors, do not show larger loops (Heger & Langer 2000; Georgy et al. 2013), and thus would face the same difficulty.

In order to test if this conclusion is also valid at very low metallicity, we continued the investigation by considering the case of SagDIG, a nearby star forming dwarf irregular whose metallicity is estimated to be even lower than that of the aforementioned galaxies, Z=0.0005. This galaxy is an ideal workbench to test the performance of models of intermediate- and high-mass stars because it harbours a recent burst of star formation, and it is sufficiently nearby that intermediate-mass stars with masses as low as M=2$M_{\odot}$can be detected. The foreground contamination has been eliminated using proper motions of individual stars (Momany et al. 2014).

From a preliminary superposition of the standard *PARSEC* evolutionary tracks with EO=0.7$H_{\rm P}$ and the observed CMD of SagDIG, we already see that the models are not able to reproduce the observed loops. This has already been noticed by Momany et al. (2005) who, in an attempt to determine the metallicity of the galaxy from the blue loop superposition, were forced to try also the lowest value of metallicity of the old Padova models, Z=0.0001.

We further performed new calculations with enhanced envelope overshooting, EO=2$H_{\rm P}$ and EO=4$H_{\rm P}$. Combining the results with other specified parameters, the IMF and SFR law, the photometric errors and the extinction in our own CMD simulator, we construct the synthetic CMDs that are compared with the observed one of SagDIG. In all models the location of the observed fiducial main sequence is well reproduced with a reasonable value of the attenuation. This is expected since the main sequence phase is not affected by envelope overshooting and the match is actually used to determine the extinction to be adopted in the simulated CMDs. As expected, models with larger envelope overshooting perform more extended blue loops, and their BHeBS get closer to the MS. In order to decide which value of envelope overshooting reproduces better the observed extension of the blue loops, we also draw and compare the fiducial lines corresponding to the BHeBS of the synthetic and of the observed CMDs. We find that the model with EO=2$H_{\rm P}$ matches the observations best, while the blue loops predicted by the case EO=0.7$H_{\rm P}$ are not hot enough and those predicted in the case of EO=4$H_{\rm P}$ are likely hotter than the data indicate. It is worth stressing that, since the value of the envelope overshooting is not an adjustable parameter in the CMD comparison, we have no better and more statistically sound method to decide which is the best case, than that of comparing the fiducial main sequences. We have also tested how the results depend on other additional assumptions concerning the attenuation and the possible effect of binarity. If we assume a differential attenuation with a reasonable model (Figure 5.13) where the attenuation has a certain dispersion around a mean value that increases with the intrinsic luminosity of the stars (Tang et al. 2014), the overall CMD fit looks better but the preferred value of the envelope overshooting remains unchanged. However, due to the dispersion introduced in the synthetic CMD, the

uncertainty of the fiducial points (the horizontal bars in the CMD figures), corresponding to the color median absolute deviation in each magnitude bin, becomes slightly larger. To single out the effect of binarity, we consider the case with constant attenuation and a binary fraction of 50%. The effect of binaries is to broaden both the main sequence and the BHeB sequence, with the consequence that the number of stars falling between the two sequences is larger than that in the case computed without considering binaries. However the BHeB sequence is clearly split into two parallel sequences between $23 \leq m_{F606W} \leq 24$, and the red He-burning sequence becomes less populated, as part of these stars move into the region populated by yellow giants/supergiants. The splitting of the BHeB sequence is not seen in the observed diagram, perhaps indicating that either the assumed binary fraction or the resulting mass ratio are too high for this galaxy of low metallicity. Furthermore, because of the asymmetric behaviour of the superposition of star pairs in the CMD, the fiducial lines shift toward the red side and, in order to reconcile the model with the observations, one should adopt a slightly lower attenuation, $\delta(m_{F606W} - m_{F814W})$ ~0.02. Even in this case the models that perform better are those computed with an envelope overshooting EO=$2H_{\rm P}$.

The results are consistent with those found in the other three galaxies with slightly higher metallicities than the one considered here. Thus the current investigation corroborates the finding that the mixing scale below the formal Schwarzschild border in the envelopes of intermediate- and high-mass stars must be significantly higher than currently assumed in *PARSEC* models. It is worth noting that there are other conditions where strong mixing below the conventional instability region is invoked such as, for example, to enhance the efficiency of the carbon dredge up during the thermally pulsing Asymptotic Giant Branch phase (Kamath et al. 2012). On the other hand, such a high value is likely incompatible with the location of the Red Giant Branch (RGB) bumps observed in Globular Clusters, which can be well reproduced by the models using an envelope overshooting not larger than EO=$0.5H_{\rm P}$. Thus it seems that the mixing scale below the formal Schwarzschild border depends on the stellar mass or luminosity or surface gravity. Furthermore the homogenization of the overshooting region happens in a relatively short timescale. The inward penetration of envelope convection in the tracks in Figure 2.13 is completed in about 10000 yr, corresponding to about 0.007 of the He-burning lifetime (t_{He} ~1.3 Myr). Then, convection remains at its maximum penetration for about 1000yr before beginning to retreat. For a pressure scale height of about $H_{\rm P}$ =3E9cm and assuming that mixing in the overshooting region propagates as diffusive process during the latter time, we get for the diffusion coefficient D~2E8cm$^2/s - \tau = l^2/(6D)-$. The corresponding velocity of propagation of the mixed region within the overshooting distance is $u_e \sim$ 0.1cm/s. This velocity is less than the estimated velocity of turbulent entrainment, representing the *slow diffusion* of turbulence into the stably stratified layers at their interface (Meakin & Arnett 2007). Thus, though the timescale of the process is relatively short, the penetration scales are fully compatible with the predictions of the turbulent entrainment theory.

Bibliography

Abt, H. A., Gomez, A. E., & Levy, S. G. 1990, ApJS, 74, 551

Alongi, M., Bertelli, G., Bressan, A., & Chiosi, C. 1991, A&A, 244, 95

Asplund, M., Grevesse, N., Sauval, A. J., Allende Prieto, C., & Kiselman, D. 2004, A&A, 417, 751

Asplund, M., Grevesse, N., Sauval, A. J., & Scott, P. 2009, ARA&A, 47, 481

Bahcall, J. N., Pinsonneault, M. H., & Wasserburg, G. J. 1995, Reviews of Modern Physics, 67, 781

Bertelli, G., Betto, R., Chiosi, C., Bressan, A., & Nasi, E. 1990, A&AS, 85, 845

Bertelli, G., Bressan, A., Chiosi, C., Fagotto, F., & Nasi, E. 1994, A&AS, 106, 275

Bertelli, G., Bressan, A. G., & Chiosi, C. 1985, A&A, 150, 33

Bertelli, G., Nasi, E., Girardi, L., & Marigo, P. 2009, A&A, 508, 355

Bessell, M. S. 2005, ARA&A, 43, 293

Bianchi, L., Efremova, B., Hodge, P., & Kang, Y. 2012a, AJ, 144, 142

Bianchi, L., Efremova, B., Hodge, P., Massey, P., & Olsen, K. A. G. 2012b, AJ, 143, 74

Bianchi, L., & Efremova, B. V. 2006, AJ, 132, 378

Bianchi, L., Scuderi, S., Massey, P., & Romaniello, M. 2001, AJ, 121, 2020

Böhm-Vitense, E. 1958, ZAp, 46, 108

Bouret, J.-C., Lanz, T., Martins, F., et al. 2013, A&A, 555, A1

Bresolin, F., Pietrzyński, G., Urbaneja, M. A., et al. 2006, ApJ, 648, 1007

Bressan, A., Fagotto, F., Bertelli, G., & Chiosi, C. 1993, A&AS, 100, 647

Bressan, A. G., Chiosi, C., & Bertelli, G. 1981, A&A, 102, 25

Bressan, A., Marigo, P., Girardi, L., Nanni, A., & Rubele, S. 2013, in European Physical Journal Web of Conferences, Vol. 43, European Physical Journal Web of Conferences, 3001

Bressan, A., Marigo, P., Girardi, L., et al. 2012, MNRAS, 427, 127

Brunish, W. M., & Becker, S. A. 1990, ApJ, 351, 258

Caffau, E., Ludwig, H.-G., Steffen, M., Freytag, B., & Bonifacio, P. 2011, Sol. Phys., 268, 255

Calzetti, D., Kinney, A. L., & Storchi-Bergmann, T. 1994, ApJ, 429, 582

Cardelli, J. A., Clayton, G. C., & Mathis, J. S. 1989a, ApJ, 345, 245

Cardelli, J. A., Clayton, G. C., & Mathis, J. S. 1989b, ApJ, 345, 245

Cassisi, S., Marín-Franch, A., Salaris, M., et al. 2011, A&A, 527, A59

Castelli, F., & Kurucz, R. L. 2003, in IAU Symposium, Vol. 210, Modelling of Stellar Atmospheres, ed. N. Piskunov, W. W. Weiss, & D. F. Gray, 20P

Chabrier, G. 2001, ApJ, 554, 1274

Chen, Y., Bressan, A., Girardi, L., et al. 2015, MNRAS, 452, 1068

Chen, Y., Girardi, L., Bressan, A., et al. 2014, MNRAS, 444, 2525

Chiosi, C., & Summa, C. 1970, Ap&SS, 8, 478

Christensen-Dalsgaard, J., Monteiro, M. J. P. F. G., Rempel, M., & Thompson, M. J. 2011, MNRAS, 414, 1158

Cioni, M.-R. L., & Habing, H. J. 2005, A&A, 429, 837

Cyburt, R. H., Amthor, A. M., Ferguson, R., et al. 2010, ApJS, 189, 240

Dalcanton, J. J., Williams, B. F., Seth, A. C., et al. 2009, ApJS, 183, 67

Davidge, T. J. 2003, PASP, 115, 635

de Jager, C., Nieuwenhuijzen, H., & van der Hucht, K. A. 1988, A&AS, 72, 259

de Vaucouleurs, G. 1959, Handbuch der Physik, 53, 311

Deheuvels, S., Michel, E., Goupil, M. J., et al. 2010, A&A, 514, A31

Demers, S., & Battinelli, P. 2002, AJ, 123, 238

Dewitt, H. E., Graboske, H. C., & Cooper, M. S. 1973, ApJ, 181, 439

Di Cecco, A., Bono, G., Stetson, P. B., et al. 2010, ApJ, 712, 527

Dohm-Palmer, R. C., & Skillman, E. D. 2002, AJ, 123, 1433
Dolphin, A. E., Saha, A., Skillman, E. D., et al. 2003a, AJ, 125, 1261
Dolphin, A. E., Saha, A., Skillman, E. D., et al. 2003b, AJ, 126, 187
Duquennoy, A., & Mayor, M. 1991, A&A, 248, 485
Fagotto, F., Bressan, A., Bertelli, G., & Chiosi, C. 1994a, A&AS, 104, 365
Fagotto, F., Bressan, A., Bertelli, G., & Chiosi, C. 1994b, A&AS, 105, 29
Fagotto, F., Bressan, A., Bertelli, G., & Chiosi, C. 1994c, A&AS, 105, 39
Georgy, C., Saio, H., & Meynet, G. 2014, MNRAS, 439, L6
Georgy, C., Ekström, S., Eggenberger, P., et al. 2013, A&A, 558, A103
Gieren, W., Pietrzyński, G., Nalewajko, K., et al. 2006, ApJ, 647, 1056
Gieren, W., Pietrzyński, G., Szewczyk, O., et al. 2008, ApJ, 683, 611
Gilmore, G. 1984, MNRAS, 207, 223
Girardi, L., Bertelli, G., Bressan, A., et al. 2002, A&A, 391, 195
Girardi, L., Bressan, A., Bertelli, G., & Chiosi, C. 2000, A&AS, 141, 371
Girardi, L., Groenewegen, M. A. T., Hatziminaoglou, E., & da Costa, L. 2005, A&A, 436, 895
Girardi, L., Rubele, S., & Kerber, L. 2009, MNRAS, 394, L74
Godart, M., Noels, A., & Scuflaire, R. 2013, in European Physical Journal Web of Conferences, Vol. 43, European Physical Journal Web of Conferences, 1008
Gordon, K. D., & Clayton, G. C. 1998, ApJ, 500, 816
Graboske, H. C., Dewitt, H. E., Grossman, A. S., & Cooper, M. S. 1973, ApJ, 181, 457
Gräfener, G., & Hamann, W.-R. 2008, A&A, 482, 945
Grevesse, N., & Sauval, A. J. 1998, Space Sci. Rev., 85, 161
Groh, J. H., Meynet, G., Ekström, S., et al. 2013, in EAS Publications Series, Vol. 60, EAS Publications Series, ed. P. Kervella, T. Le Bertre, & G. Perrin, 51
Haft, M., Raffelt, G., & Weiss, A. 1994, ApJ, 425, 222
Halabi, G. M., El Eid, M. F., & Champagne, A. 2012, ApJ, 761, 10
Heger, A., & Langer, N. 2000, ApJ, 544, 1016
Hodge, P., & Miller, B. W. 1995, ApJ, 451, 176
Humphreys, R. M., & Davidson, K. 1979, ApJ, 232, 409
Iben, Jr., I. 1966, ApJ, 143, 483
Iglesias, C. A., & Rogers, F. J. 1996, ApJ, 464, 943
Itoh, N., & Kohyama, Y. 1983, ApJ, 275, 858
Itoh, N., Uchida, S., Sakamoto, Y., Kohyama, Y., & Nozawa, S. 2008, ApJ, 677, 495
Kamath, D., Karakas, A. I., & Wood, P. R. 2012, ApJ, 746, 20
Kamath, D., Wood, P. R., Soszyński, I., & Lebzelter, T. 2010, MNRAS, 408, 522
Kang, A., Sohn, Y.-J., Kim, H.-I., et al. 2006, A&A, 454, 717
Karachentsev, I., Aparicio, A., & Makarova, L. 1999, A&A, 352, 363
Kato, S. 1966, PASJ, 18, 374
Kaufer, A., Venn, K. A., Tolstoy, E., Pinte, C., & Kudritzki, R.-P. 2004, AJ, 127, 2723
Kennicutt, Jr., R. C. 1998, in Astronomical Society of the Pacific Conference Series, Vol. 142, The Stellar Initial Mass Function (38th Herstmonceux Conference), ed. G. Gilmore & D. Howell, 1
Kniazev, A. Y., Grebel, E. K., Pustilnik, S. A., Pramskij, A. G., & Zucker, D. B. 2005, AJ, 130, 1558
Kroupa, P. 2001, MNRAS, 322, 231
Kroupa, P., Tout, C. A., & Gilmore, G. 1993, MNRAS, 262, 545
Lauterborn, D., Refsdal, S., & Weigert, A. 1971, A&A, 10, 97
Lee, H., Skillman, E. D., & Venn, K. A. 2005, ApJ, 620, 223
Lee, M. G., & Kim, S. C. 2000, AJ, 119, 777
Lodders, K., Palme, H., & Gail, H.-P. 2009, in Landolt-Börnstein - Group VI Astronomy and Astrophysics Numerical Data and Functional Relationships in Science and Technology Volume 4B: Solar System. Edited by J.E. Trümper, 2009, 4.4., ed. J. E. Trümper, 44
Maeder, A., Przybilla, N., Nieva, M.-F., et al. 2014, A&A, 565, A39
Marigo, P., & Aringer, B. 2009, A&A, 508, 1539
Marigo, P., Girardi, L., Bressan, A., et al. 2008, A&A, 482, 883
Martins, F., & Palacios, A. 2013, A&A, 560, A16
Massevitch, A. G., Popova, E. I., Tutukov, A. V., & Iungelson, L. R. 1979, Ap&SS, 62, 451
Meakin, C. A., & Arnett, D. 2007, ApJ, 667, 448
Mermilliod, J.-C., Rosvick, J. M., Duquennoy, A., & Mayor, M. 1992, A&A, 265, 513
Miller, G. E., & Scalo, J. M. 1979, ApJS, 41, 513

Misselt, K. A., Clayton, G. C., & Gordon, K. D. 1999, ApJ, 515, 128
Momany, Y., Held, E. V., Saviane, I., & Rizzi, L. 2002, A&A, 384, 393
Momany, Y., Held, E. V., Saviane, I., et al. 2005, A&A, 439, 111
Momany, Y., Clemens, M., Bedin, L. R., et al. 2014, A&A, 572, A42
Muijres, L., Vink, J. S., de Koter, A., et al. 2012, A&A, 546, A42
Munakata, H., Kohyama, Y., & Itoh, N. 1985, ApJ, 296, 197
Nugis, T., & Lamers, H. J. G. L. M. 2000, A&A, 360, 227
Pagel, B. E. J., Edmunds, M. G., & Smith, G. 1980, MNRAS, 193, 219
Rana, N. C., & Basu, S. 1992, A&A, 265, 499
Richer, M. G., & McCall, M. L. 1995, ApJ, 445, 642
Robertson, J. W. 1972, ApJ, 173, 631
Rocha-Pinto, H. J., Maciel, W. J., Scalo, J., & Flynn, C. 2000, A&A, 358, 850
Ryan, S. G., & Norris, J. E. 1991, AJ, 101, 1865
Salpeter, E. E. 1955, ApJ, 121, 161
Saviane, I., Rizzi, L., Held, E. V., Bresolin, F., & Momany, Y. 2002, A&A, 390, 59
Scalo, J. M. 1986, Fund. Cosmic Phys., 11, 1
Schlegel, D. J., Finkbeiner, D. P., & Davis, M. 1998, ApJ, 500, 525
Schmidt, M. 1959, ApJ, 129, 243
Seaton, M. J. 1979, MNRAS, 187, 73P
Sibbons, L. F., Ryan, S. G., Cioni, M.-R. L., Irwin, M., & Napiwotzki, R. 2012, A&A, 540, A135
Silva, L., Granato, G. L., Bressan, A., & Danese, L. 1998, ApJ, 509, 103
Skillman, E. D., Kennicutt, R. C., & Hodge, P. W. 1989a, ApJ, 347, 875
Skillman, E. D., Terlevich, R., & Melnick, J. 1989b, MNRAS, 240, 563
Stothers, R. B., & Chin, C.-W. 1991, ApJ, 374, 288
Tang, J., Bressan, A., Rosenfield, P., et al. 2014, MNRAS, 445, 4287
Tolstoy, E., Irwin, M. J., Cole, A. A., et al. 2001, MNRAS, 327, 918
Torres, G., Vaz, L. P. R., Sandberg Lacy, C. H., & Claret, A. 2014, AJ, 147, 36
Twarog, B. A. 1980, ApJS, 44, 1
Urbaneja, M. A., Kudritzki, R.-P., Bresolin, F., et al. 2008, ApJ, 684, 118
Vanhollebeke, E., Groenewegen, M. A. T., & Girardi, L. 2009, A&A, 498, 95
Venn, K. A., Tolstoy, E., Kaufer, A., et al. 2003, AJ, 126, 1326
Venn, K. A., Lennon, D. J., Kaufer, A., et al. 2001, ApJ, 547, 765
Vink, J. S., de Koter, A., & Lamers, H. J. G. L. M. 2000, A&A, 362, 295
Vink, J. S., de Koter, A., & Lamers, H. J. G. L. M. 2001, A&A, 369, 574
Vink, J. S., Muijres, L. E., Anthonisse, B., et al. 2011, A&A, 531, A132
Walmswell, J. J., Tout, C. A., & Eldridge, J. J. 2015, MNRAS, 447, 2951
Weiss, A., Serenelli, A., Kitsikis, A., Schlattl, H., & Christensen-Dalsgaard, J. 2005, A&A, 441, 1129
Woosley, S. E., & Heger, A. 2012, ApJ, 752, 32
Xu, H. Y., & Li, Y. 2004, A&A, 418, 225
Young, P. J. 1976, AJ, 81, 807
Zoccali, M., Renzini, A., Ortolani, S., et al. 2003, A&A, 399, 931